Atmospheric chemistry at the ocean surface: investigating ozonolysis in the sea surface microlayer

Adam Saint

PhD

University of York

Chemistry

September 2019

Abstract

Reactive dry deposition in the marine environment is a significant sink of surface level ozone in the troposphere. Previous measurements are sparse but indicate that the uncertainties in quantifying this loss are high. This thesis presents additional measurements of ozone deposition to both synthetic and real seawater samples to attempt to reduce these uncertainties.

A new flow reactor was used to measure the second order rate constant for the reaction of ozone and dissolved iodide, matching the number of measurements of this value at room temperature in the literature. A value of $1.94 \pm 0.20 \times 10^9$ M^{-1} s^{-1} was obtained, reducing the error in this measurement from 28% to 10%.

Ozone deposition was measured onto synthetic seawater samples containing unsaturated fatty acids. The reaction proceeded according to the Langmuir-Hinshelwood surface reaction mechanism, as expected for the reaction of ozone and organics. It was shown that reactivity increased with increasing number of double bonds and in the presence of dissolved iodide. It was also shown that organic molecules partially inhibit the reaction of ozone with dissolved iodide.

Surface and underlying water samples were collected from the North Sea in 2017 and 2018 and the ozone depositions measured. A deposition of ozone was estimated based on measured iodide concentration measurements and the rate constant mentioned previously. These were compared to actual measured ozone deposition; iodide was found to contribute between 8% and 43% of the measured reactive ozone loss, considerably less than estimated previously.

Contents

List of Figures

List of Tables

Acknowledgements

My thanks first of all go to my primary supervisor, Prof. Lucy Carpenter for her support and guidance throughout this project. My thanks also go to Prof. Ally Lewis for all of his input and advice.

I would like to thank the other members of the Carpenter group and the wider team at WACL for the good times shared during this project and for all the discussion and collaboration that has made this project so much more fruitful. I especially thank Rosie and Liselotte, and everyone else we managed to coerce into sieving the ocean with us!

I would like to thank all the organisers and collaborators of 2017's MILAN campaign for all their hard work and for hosting me in Wilhelmshaven. It was a fantastic experience made all the better thanks to the people I got to share it with.

Finally, I would like to thank my family for all their encouragement and faith, and my partner, Sophie, to whom I will be forever grateful and whose continued support over the years has made this accomplishment possible.

Declaration

I declare that this thesis is a presentation of original work and I am the sole author. This work has not previously been presented for an award at this, or any other, University. All sources are acknowledged as References.

Chapter 1

Introduction

1.1 The composition and structure of the atmosphere

The Earth's atmosphere consists of a mixture of nitrogen (N_2, 78%), oxygen (O_2, 21%), argon (Ar, $< 1\%$), water vapour (H_2O, $< 1\%$) and many other trace species. Most of the mass of the atmosphere is concentrated at the surface due to gravity and there is an exponential decrease in pressure with increasing altitude. The relationship of temperature with altitude is more complicated and as such a wide range of temperatures and temperature gradients can be observed throughout the atmosphere.

The atmosphere can be divided into approximate regions based upon changes in the temperature gradient, as shown in figure 1.1. In the lowest of these regions, the troposphere, infrared radiation emitted by the Earth's surface is absorbed by the atmosphere. Warm surface air expands and becomes less dense than higher, colder air. These differences in density cause the warmer air to become buoyant and rises. As a particular packet of air rises into a less dense section of the atmosphere, it expands and displaces the air at that altitude. This work requires energy causing the air packet to cool. The mixing of material and energy throughout the troposphere occurs in this way by convection, and a steady decrease in temperature with altitude can be observed.

In the next region of the atmosphere, the stratosphere, the concentration of atmospheric ozone reaches a maximum as in figure 1.1 [66]. Here, UV radiation from the Sun is directly absorbed by ozone and the temperature rises. The point of temperature gradient inversion between the troposphere and stratosphere (at an altitude of approximately 12 km) is referred to as the tropopause.

As the temperature gradient in the stratosphere is positive, higher air is warmer and less dense than the cold air below it. This causes stability and stratification of the air packets in the stratosphere with far less mixing than in the troposphere below. The altitude boundaries of the troposphere and

stratosphere are not fixed, and the exact height of the tropopause can vary depending on latitude, topography and weather.

As the inversion in the temperature gradient stops convection between the troposphere and stratosphere, the movement of air over the tropopause is much slower than the turbulent mixing of air within the troposphere. High energy tropospheric storms are able to puncture this barrier and move energy, water vapour and other material up into the stratosphere and air near the jet streams can be exchanged between the two regions.

Almost all natural (biogenic) and human (anthropogenic) emissions into the atmosphere occur within the troposphere, at the surface. The reactions of these compounds in the troposphere are controlled by photochemistry and the available wavelengths of light. As previously mentioned, UV solar radiation is absorbed by stratospheric ozone, effectively filtering out these wavelengths of light ($200 - 315$ nm) and preventing them from penetrating into the troposphere. Most reactive chemical species in the atmosphere experience increasing oxidation with time until they are removed from the atmosphere by wet deposition (dissolution in precipitation), dry deposition (reactions with, adsorption onto or settling upon a surface) or biological uptake.

1.2 Ozone as an atmospheric pollutant

Ozone is an extremely important atmospheric gas due to its effects on human [129], animal [115] and plant [140] health as well as the global climate [18]. Exposure to ozone has been shown in some clinical trials to cause immediate respiratory distress in both humans and animals, with particular adverse pulmonary effects observed in children and asthmatic patients [27, 75]. In addition, chronic exposure to ozone has been shown to negatively affect baseline respiratory function and damage lung structure [74].

Ozone has been recognised as one of the most damaging air pollutants to plant life globally [25]. It has been shown that ozone exposure by cotton

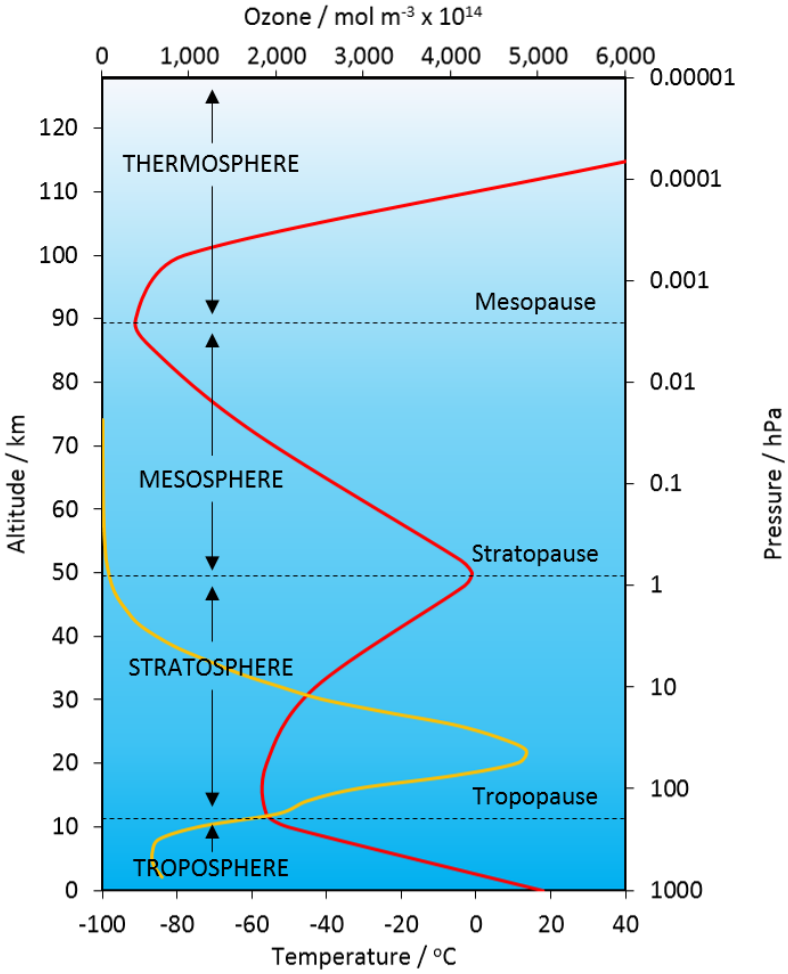

Figure 1.1: Temperature profile (red line) of the first 100 km of the Earth's atmosphere with labelled regions and boundaries with approximate ozone concentrations (yellow line) from Krueger and Minzner, 1976 [66]

plants reduced the observed growth and final yield over multiple seasons [89], single exposures of oilseed rape plants to ozone reduced the oil yield from the seeds [8] and ambient ozone exposure was responsible for a reduction in seed number (-16%), fruit number (-9%) and fruit weight (-22%) in a number of crop species [69]. In addition, increased ozone exposure has been cited as a potential contributor for forest decline in the US and Europe [83].

It is well established that human activity has caused the Earth's climate to change through alterations to surface conditions and the chemical composition of the atmosphere [99]. A common metric used to compare the effects of various climate altering processes is radiative forcing (RF). RF is defined as the energy change per unit area (in W m^{-2}) due to a particular process and is usually averaged over a period of time. Figure 1.2 shows the radiative forcing from several atmospheric gases plus some other effects. Many climate active chemical pollutants are released directly as primary emissions, others are formed in the atmosphere as the secondary products of chemical reactions of primary sources. Tropospheric ozone is an example of a secondary climate active pollutant and is formed through the reactions of the hydroxyl radical ($^{\bullet}$OH), hydrocarbons and nitrogen oxides (NO_x) which are common anthropogenic emissions.

The impact of ozone on the climate varies according to geographical location and is coupled very strongly to other effects such as temperature and water vapour concentration [68]. In addition, ozone is a highly reactive compound with a low atmospheric lifetime (average global mean lifetime = 22.3 $\pm$ 2 days [126]) and variable surface abundances. It is therefore necessary for estimates of the effects of ozone on the climate or air quality to be computed in climate models. The effects of ozone on the historic climate must also be modelled in this way as direct measurements of atmospheric ozone before the 1970s are very sparse and ozone is too reactive to persist in ice cores [127].

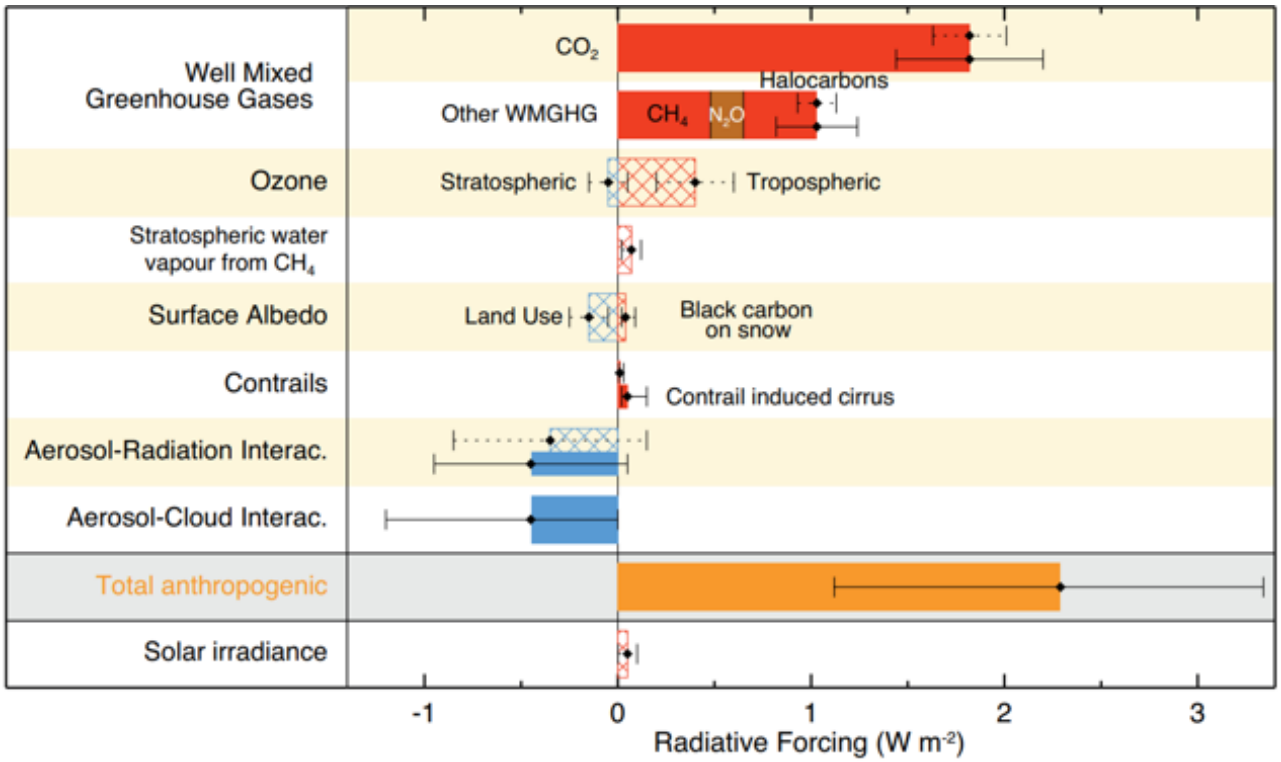

Figure 1.2: Bar chart showing the radiative forcing of several climate relevant gases and other changes for the period 1750-2011. Reproduced from the IPCC 5^{th} Assessment Report, 2013 [99]

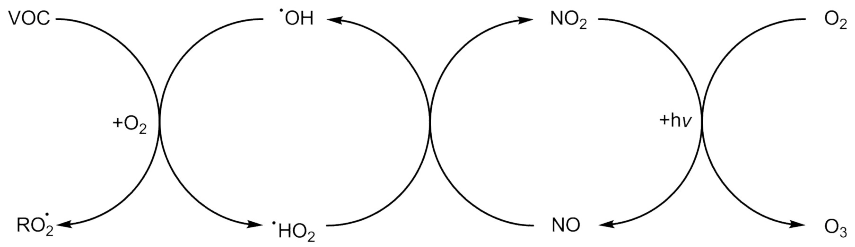

Figure 1.3: Ozone generation through the NO_x cycle

In general, tropospheric ozone absorbs infrared radiation emitted by the Earth in a wavelength range where few other atmospheric gases absorb (λ_{max} $\approx$ 9.5 μm) causing a warming effect (see figure 1.2). The negative radiative forcing for stratospheric ozone in figure 1.2 is caused by anthropogenic degradation of the ozone layer at these higher altitudes leading to less absorbed longwave radiation.

1.3 Sources and sinks of tropospheric ozone

There are two main sources of tropospheric ozone: direct generation from the photochemical reactions of the oxides of nitrogen, see the NO_x cycle in figure 1.3, and to a lesser extent, migration of stratospheric ozone into the lower atmosphere [32].

As shown in figure 1.3 and mentioned previously, the chemistry of ozone in the atmosphere is directly coupled to that of NO_x and $^{\bullet}OH$. $^{\bullet}OH$ is formed through the reaction of water (H_2O) with the excited singlet oxygen radical (O^1D), formed by the photolysis of ozone (at λ = 230 - 308 nm [130]) as in reactions 1.1 and 1.2.

$$O_3 \xrightarrow{h\nu} O^1D + O_2 \tag{1.1}$$

$$O^1D + H_2O \longrightarrow 2^{\bullet}OH \tag{1.2}$$

Further reactions can continue leading to the catalytic destruction of O_3 by $^{\bullet}OH$ via production and destruction of the hydroperoxy radical, $HO_2^{\bullet}$, as

in reactions 1.3 and 1.4.

$$^{\bullet}OH + O_3 \longrightarrow HO_2^{\bullet} + O_2 \tag{1.3}$$

$$HO_2^{\bullet} + O_3 \longrightarrow {}^{\bullet}OH + 2O_2 \tag{1.4}$$

Organic compounds can react with $^{\bullet}OH$ to form organic peroxy radicals which then react to form organic acids, an example reaction pathway with methane (CH_4) is shown in reactions 1.5, 1.6 and 1.7. Together, $HO_2^{\bullet}$ and organic peroxy radicals (such as $CH_3O_2^{\bullet}$) are referred to as $RO_2^{\bullet}$.

$$CH_4 + {}^{\bullet}OH \longrightarrow {}^{\bullet}CH_3 + H_2O \tag{1.5}$$

$$^{\bullet}CH_3 + O_2 + M \longrightarrow CH_3O_2^{\bullet} + M \tag{1.6}$$

$$CH_3O_2 + HO_2^{\bullet} + M \longrightarrow CH_3OOH + O_2 + M \tag{1.7}$$

In isolation, O_3 catalytically converts NO into NO_2 which photolytically decays into NO as in reactions 1.8, 1.9 and 1.10. This cycle does not lead to any change in O_3 or NO_x overall.

$$NO + O_3 \longrightarrow NO_2 + O_2 \tag{1.8}$$

$$NO_2 \xrightarrow{h\nu} NO + {}^{\bullet}O \tag{1.9}$$

$$^{\bullet}O + O_2 + M \longrightarrow O_3 + M \tag{1.10}$$

Combining the chemistry of HO_x and NO_x, ozone is generated catalytically through reactions 1.11, 1.12 and 1.13. These two pathways occur in tandem, with each particular set of local emissions and concentrations altering the balance between them.

$$NO + HO_2 \longrightarrow NO_2 + {}^{\bullet}OH \tag{1.11}$$

$$NO_2 \xrightarrow{h\nu} NO + {}^{\bullet}O \tag{1.12}$$

$$^{\bullet}O + O_2 \longrightarrow O_3 \tag{1.13}$$

A summary of the global tropospheric ozone budget (from a standard GEOS-Chem v10-01 simulation) is given in table 1.1 [53]. From the values shown it can be seen that the primary source (94%) of ozone in the troposphere are the chemical reactions of peroxy radicals with NO with the remainder coming from stratosphere-troposphere exchange (STE, 6%) though this could be an underestimation in this version of the model. The largest fraction of reactive ozone formation is attributed to the hydroperoxy radical (62% of the total ozone formation), followed by the methylperoxy radical (23%) then all other organic peroxy radicals make up the smallest share (8%). It should be noted that the values shown here represent global averages and it is expected that local variations in conditions could cause large shifts in the relative contributions of these reactive pathways.

It can be seen from table 1.1 that the primary sink of tropospheric ozone is homogeneous gas phase reactions, the largest of which is photolysis to $^{\bullet}O$ followed by the reaction with water vapour (reactions 1.1 and 1.2, 42% of the total ozone loss). As the photolysis reaction is driven by absorption of UV light, the extent to which this occurs in the troposphere is directly correlated to amount of ozone filtering out these wavelengths in the stratosphere. The next most significant reactive sink of ozone is the catalytic reaction cycle with $^{\bullet}OH$ and $HO_2^{\bullet}$ (reactions 1.3 and 1.4) which together make up around a third (35%) of the total ozone loss. Dry deposition makes up the third largest sink (21% of total ozone loss) and comprises all chemical and physical deposition onto the Earth's surface. By comparison, the sink of tropospheric ozone via wet deposition is relatively small (ozone loss due to dissolution in precipitation, 0.3%) due to ozone's low solubility in water [7].

Table 1.1: Global budget of tropospheric ozone in GEOS-Chem [53]

Sources / Tg yr^{-1}	
Chemical Production	4960
$HO_2^\bullet + NO$	66%
$CH_3O_2^\bullet + NO$	25%
$RO_2^\bullet + NO$	9%
STE	325
Total	5290

Sinks / Tg yr^{-1}	
Chemical Loss	4360
$O^\bullet + H_2O$	51%
$HO_2^\bullet + O_3$	27%
$^\bullet OH + O_3$	15%
$HOBr + h\nu$	4%
Others	3%
Dry Deposition	908
Wet Deposition	17
Total	5290

1.4 Ozone dry deposition

The dry deposition of ozone is estimated to account for 20-25% of tropospheric ozone loss and as is comprised of many different physical and chemical processes occurring on many different types of surface. These depositions can vary widely in magnitude as shown in table 1.2 where three types of vegetative land surface show different responses to different seasonal coverages [144]. Due to the complex relationships that occur between ozone and different surface types, O_3 dry deposition is often poorly represented in atmospheric models [44].

Li *et al.* measured the dry deposition of ozone onto several Mediterranean forests under semiarid and humid conditions [73]. Ozone deposition velocities were recorded in the range of -0.8 - 1.5 cm s^{-1} across the sampling sites, seasons and time of day. Large variations were recorded in the average diurnals, with increases in daytime compared to nighttime deposition velocity of up to 74% in the spring and summer and approximately 8% in autumn winter. On several occasions during extreme dry surface events, negative values of deposition velocity were recorded. These events were attributed to the dry conditions limiting the water retention of the forest canopy, significantly reducing ozone uptake whereas the aerosol in air above was more able to act as a sink of ozone leading to a positive flux. Increased relative humidity was said to stimulate leaf-surface wetness leading to higher non-stomatal ozone deposition due to the waxy nature of leaf surfaces.

Ozone deposition onto various bare soils was measured by the eddy correlation method by Stella *et al.* [125]. Nighttime deposition velocity averaged around 0.15 - 0.25 cm s^{-1}, maximum deposition velocities were recorded in the early morning of 0.30 - 0.60 cm s^{-1}. It was found that soil resistance to ozone uptake increased exponentially with increasing relative humidity for all soil types though to differing degrees. This was due to ozone being generally insoluble in water and the presence of extra moisture restricted the number of available dry sites in the soil for deposition to occur. In addition, soils with higher clay contents were found to have lower resistances due to larger pore

Table 1.2: Typical values for bulk surface deposition velocity (in cm s^{-1}) for a number of different vegetation types, surface coverages and seasons at a height of 10 m and a solar irradience of 800 W m^{-2} under dry conditions and moderate wind speeds. Adapted from Wesely and Hicks, 2000 [144]

Season and coverage	Agricultural land	Rangeland	Deciduous forest
Midsummer with lush vegetation	1.3	0.9	1.0
Autumn with unharvested cropland	0.5	0.4	0.2
Late autumn after frost, no snow	0.7	0.5	0.3
Winter, snow on ground near freezing	0.1	0.1	0.2
Transitional spring with partially green short annuals	1.0	0.7	0.6

sizes in the clay soils providing greater surface area for deposition. Variations observed in minimum soil resistance were from 12 ± 1.20 s m^{-1} to 800 s m^{-1} for clay contents of 54 % and 0%, respectively.

The dry depositions of ozone onto several different water-based surface types including fresh water, sea water, snow and sea ice, have been reported in the literature. Values for deposition velocities onto water based surfaces are given in table 1.3 along with the method used to determine deposition velocity and whether the method was deployed in the field (*in situ*) or samples were returned to the lab for analysis. Large ranges were observed for all surface types and sampling methods, with no clear bias towards any particular method. Deposition velocities onto these water based surfaces were generally lower than those reported onto vegetation or soil, with snow covered land showing the greatest ozone deposition velocity due to the presence of soil underneath.

Some rough calculations can be made to estimate the deposition velocity of ozone to water due only to dissolution. In a closed system, the amount of a gas that dissolves in a solvent is controlled by Henry's law. For the dissolution of ozone in pure water under standard conditions, the Henry's law constant is approximately equal to 4, indicating the saturated aqueous concentration of ozone is approximately equal to a quarter of the gas phase ozone concentration [7]. Ozone loss to natural water sources does not exist in a closed system, however, as turbulent mixing of both the liquid surface and lower atmosphere constantly refresh the initial conditions. In this case, a better estimate for ozone loss can be obtained from the Noyes - Whitney equation for the rate of dissolution (equation 1.14), where dm is the amount of solute transferred into the solvent, dt is the time over which the mass transfer occurs, D is the diffusivity constant, A is the interfacial surface area, C_s is the solubility, here defined as the saturated aqueous concentration, C is the concentration of solute at time t and h is the thickness of the boundary layer of solvent at the solvent/solute interface.

$$\frac{dm}{dt} = DA\frac{C_s - C_t}{h} \tag{1.14}$$

Table 1.3: Literature values for ozone deposition velocity onto snow, sea ice, fresh water and sea water surfaces in order of ascending minimum measured deposition velocity

Surface type	Method	Deposition velocity / cm s^{-1}	Ref.
Snow	*In situ* box enclosure	0.004 - 1.250	[30]
Snow	Tower eddy correlation	0.01	[50]
Snow	Tower eddy correlation	0.03	[143]
Snow	Tower eddy correlation	0.03	[136]
Sea ice	Tower eddy correlation	-0.12 - 0.05	[97]
Sea ice	Tower eddy correlation	0.006 - 0.3	[40]
Sea ice	Aircraft eddy correlation	0.07	[128]
Fresh water	*In situ* box enclosure	0.012 - 0.083	[30]
Fresh water	Lab box enclosure	0.015 - 0.100	[30]
Fresh water	Tower eddy correlation	0.01	[143]
Fresh water	*In situ* box enclosure	0.1	[2]
Sea water	Lab box enclosure	0.002 - 0.015	[85]
Sea water	Sonde ozone profile	0.009 - 0.017	[133]
Sea water	Ship eddy correlation	0.009 - 0.24	[5]
Sea water	*In situ* box enclosure	0.023 - 0.083	[30]
Sea water	Aircraft eddy correlation	0.024	[60]
Sea water	Lab box enclosure	0.025 - 0.091	[30]
Sea water	Tower eddy correlation	0.025	[87]
Sea water	Tower eddy correlation	0.030	[145]
Sea water	*In situ* box enclosure	0.03 - 0.06	[2]
Sea water	Lab wind tunnel	0.04	[36]
Sea water	Aircraft eddy correlation	0.056	[70]
Sea water	Tower eddy correlation	0.11	[31]

If a spherical flask (V = 1 L) half filled with pure water was opened to a flow of ozone (1000 sccm, 100 ppbv) under standard conditions the loss of ozone due to dissolution can be calculated using equation 1.14. Using the ideal gas equation, the gas phase concentration of ozone can be estimated as 4.09 × $10^{-}9$ mol dm^{-3}. Assuming a Henry's law constant of 4, this gives an estimate of the saturated aqueous concentration (C_s) of 1.02 × $10^{-}9$ mol dm^{-3}. At time t = 0 s, the concentration of ozone in the water is equal to 0 mol dm^{-3}, thus the term C_t in equation 1.14 can be ignored. Under standard conditions, the diffusivity constant for ozone in water can be taken from Johnson and Davis, where D was measured at 298.2 K to be 1.89 × 10^{-9} m^2 s^{-1} [56]. The interfacial surface area between the solute and solvent can be estimated as the surface area of the water, equal to πr^2, giving A = 0.012 m^2. Assuming the solvent is well mixed, the boundary layer height can be estimated as the ratio of the liquid volume to surface area giving h = 0.041 m.

Inputting these values into equation 1.14 gives an estimate for the dissolution rate at time t = 0 s of 5.65 × 10^{-16} mol s^{-1}. At a gas flow rate of 1000 scccm, the residence time of ozone in the flask is 30 s. Thus, the amount of ozone dissolved into the water before the gas in the flask is replenished is approximately 1.69 × 10^{-14} mol. The dissolution only deposition velocity can be estimated using equation 1.15 to be 1.14 × 10^{-6} cm s^{-1} [113].

$$v_D = \frac{ln\frac{[O_3]_i}{[O_3]_f}}{\frac{A}{V_{gas}}t} \tag{1.15}$$

From table 1.3 it can be seen that ozone depositions onto fresh and sea water samples are higher than might be expected from dissolution alone by upwards of three orders of magnitude. This would indicate that deposition onto natural water surfaces is dominated by reactive chemical rather than purely physical processes. Deposition onto fresh water is generally lower in magnitude than onto sea water which can in part be attributed to the presence of reactive salts in sea water that are not present in fresh water, such as iodide, providing an extra reactive sink of ozone [116]. Overall, it appears

likely that the particular conditions, sampling locations and specific local water composition of each study have a greater influence on measured deposition velocity than the type of water surface being considered.

1.5 Modelling marine ozone deposition

Atmospheric models are used to create estimates of the composition of the Earth's atmosphere using knowledge of the chemical and physical processes occurring within it. Such models can vary in complexity in terms of the processes considered (e.g. atmosphere, hydrosphere, lithosphere), their scale (i.e. global or regional) and resolution (both time and spatial), each depending on the specific research questions being considered and computational resources available.

When modelling the behaviour and fate of an atmospheric constituent species such as ozone, a number of processes must be considered including emission (both biogenic and anthropogenic), chemical reactions (as combinations of differential rate equations), transport (simulating spatial movement over time) and deposition (both wet and dry).

The most computationally costly process in most chemical models is the reactive gas phase chemistry, as each individual chemical transformation requires its own rate equation, all which are then combined for each iterative time step to calculate new concentrations. It is therefore not uncommon for a atmospheric chemical model to only consider the reactions of a few key species in each run to minimise the computational time required for processing.

While each of the gas phase reactions of a particular species may be well known, the different physical and reactive dry deposition processes occurring at the planet's surface are often much less certain. Such uncertainties arise from the small scale changes in surface type (often smaller scale than the resolution of the models), heavy parameterisation and lack of direct measurements for comparison [28, 44, 144].

Dry deposition is often included in atmospheric models using the resistor approach where each individual step between a reactive species (e.g. ozone) and the surface is given a single resistance value [142]. The resistances are then compiled in series or parallel, as appropriate, then combined mathematically in an analogous fashion to resistors in an electrical circuit as can be seen from the example in figure 1.4.

It is not uncommon for climate models to treat ozone dry deposition across the entire ocean as a uniform value (approximately 0.05 cm s^{-1}) [33]. While this is within the range of measured values (see table 1.3) it does not capture the variation observed across these measurements. Efforts have been made to parameterise ozone v_D at the ocean surface, though limitations in the number and distribution of measurements lead to high uncertainties [33, 44, 116, 150].

In a review of ozone dry deposition in global climate models, Hardacre *et al.* found that dry deposition to the oceans may account for up to 60 % of the total ozone deposition [44]. Here, the ozone deposition to multiple land surface types were compared using 15 different global models. The average total annual dry deposition across all models was 978 $\pm$ 127 Tg yr^{-1} (within error of the value shown in table 1.1); the annual ozone deposition to the 'water' surface type was 250 $-$ 591 Tg yr^{-1} (25.6 - 60.4 % of the average total deposition).

This large range could not be attributed to a similar range in the deposition velocities in each model, in fact the variation in deposition velocity across the different models for the 'water' surface type was very small, $<$ 0.1 cm s^{-1}. Instead, the range was attributed to these small differences in deposition velocity being integrated over such a large area (71.2 % global coverage). It was suggested that by improving the constraints on deposition velocity to the oceans in global models, the differences in total ozone deposition could be greatly reduced.

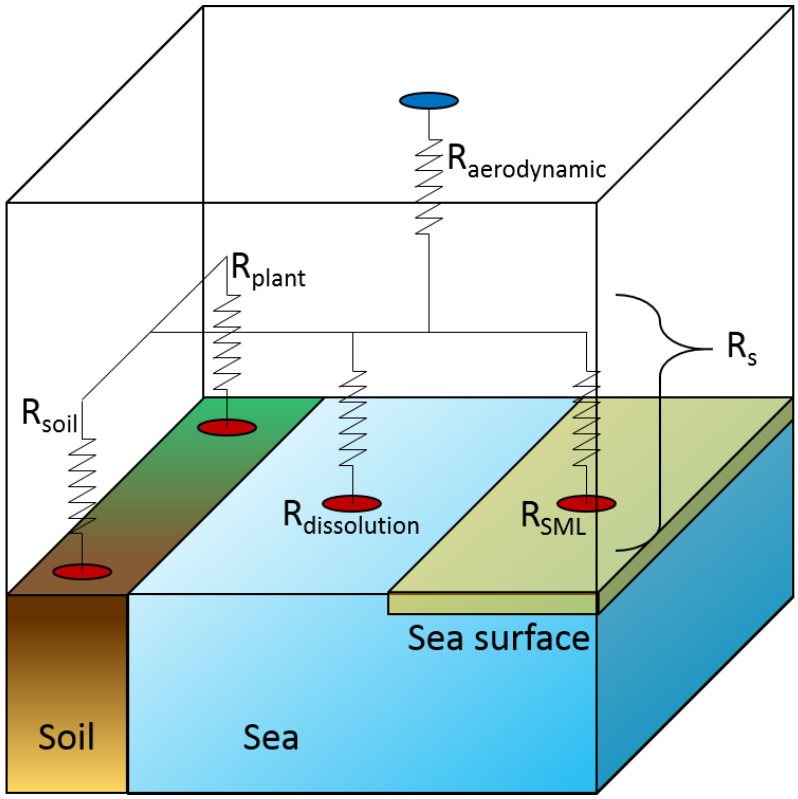

Figure 1.4: A simplified coastal dry deposition resistance scheme for transforming gas concentrations from the bulk atmosphere (blue circle) to various locations at the surface (red circles). Surface resistance, R_s, is here comprised of the resistances to the soil (R_{soil}), plant life (R_{plant}), dissolution into seawater ($R_{dissolution}$) and reactions in the sea surface microlayer (R_{SML})

1.6 The sea surface microlayer; a boundary for ocean atmosphere interactions

The transport of compounds between the atmosphere and oceans is important as the oceans can act as a source or sink for many climate active species. These exchange processes can occur on a massive scale as the ocean covers approximately 70% of the Earth's surface, but are controlled by the composition and properties of the complex and distinct uppermost few microns of the ocean surface [13].

This interfacial region is known as the sea surface microlayer (SML). SML composition varies widely with location and season but is generally concentrated in organic surfactant compounds due to hydrophobic effects, see figure 1.5 [55, 103].

As previously mentioned, a significant sink of surface level ozone is the dry deposition onto seawater. Ozone is not very soluble in seawater [7]; thus the deposition is controlled by surface reactions. There are two main surface reactions for ozone in the SML, the reactions with dissolved iodide (I^-) and with dissolved organic material (DOM) [116].

1.7 Iodide at the ocean surface

The majority of marine iodine exists as one of two inorganic ions, either iodide (I^-) or iodate ($IO_3{}^-$) with additional smaller contributions from organic iodine containing compounds [76, 146]. The ratio of marine inorganic iodine present as iodide and iodate is not constant, with particularly high ratios of iodide observed in coastal waters compared to the open ocean [134].

A recent review from Chance *et al.* (2014) collated many of the studies that have investigated the distribution of surface ocean iodide [14]. It was found that while many studies had measured marine iodide concentrations, the global

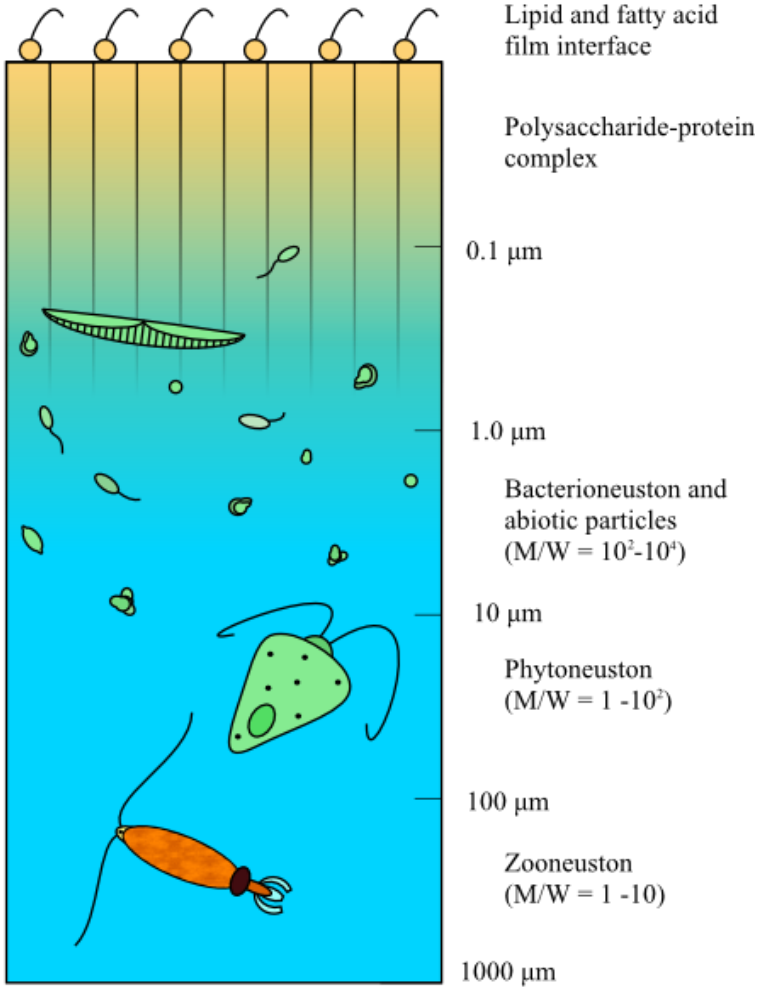

Figure 1.5: The first millimeter of the ocean; organic matter is concentrated close to the surface, in the first micrometer

distribution of these studies was quite sparse. In addition, the definitions of "surface waters" differ between studies but generally occur at depth ranges of 6-15 m, far below the depth of the SML. The surface waters in these studies can be better compared to the subsurface or bulk samples collected in studies that do make the distinction between SML and subsurface water, which are typically collected at depths of around 1 m [105, 137].

Depth profiles show relatively stable concentrations for the first 100 m then decreased concentrations in the water below which suggests that comparisons between subsurface waters from different studies can be made without matching exact depths. Measured iodide concentrations ranged from below the limit of detection to 700 nM with an average of 77 nM.

Measured iodide concentration correlated strongly with latitude, and it was noted that the profiles of iodide concentration match the profiles of water temperature, such that the square of water temperature can be used to calculate an estimate for iodide concentration. A similar parameterisation conducted by MacDonald *et al.* found a better fit though with fewer data points that gave much lower values for iodide concentration (by a factor of approximately 2) [78].

It is not currently known whether iodide is depleted or enriched in the SML. It was noted that organic iodine containing compounds that could act as a source for iodide were enriched in surface foams in Lake Mir, Croatia compared to the underlying water [135]. Since such foams are similar to those encountered on the oceans, it seems likely that sea foams would exhibit the same behaviour. However, an older study from Chapman and Liss (1981) investigating the potential enrichment of iodide and other nutrients in the SML demonstrated that iodide was neither depleted nor enriched in the SML [16]. The enrichment factor of iodide, defined as the ratio of concentrations of a species in the SML compared to the underlying water was found to be 1.13 ± 0.70; within error of unity therefore suggesting no overall difference between the SML and underlying water.

The dry deposition of ozone at the ocean surface due to the reactions with dissolved iodide will depend on the heterogeneous rate of reaction between them, $k_{O_3+I^-}$. $k_{O_3+I^-}$ has been measured in the literature several times, most recently by Shaw and Carpenter who reported a value of $2.2 \pm 0.9 \times 10^9$ M^{-1} s^{-1} [120]. This was in rough agreement with previous measurements, though the spread of values across the literature is over an order of magnitude (3.2×10^8 - 4.0×10^9 M^{-1} s^{-1}) [52, 79]. This will be discussed further in chapter 2, section 2.3.

1.8 DOM at the ocean surface

The measurement of marine dissolved organic carbon (DOC) and, more broadly, dissolved organic matter (DOM) have rapidly developed in the past few decades. Marine DOM represents one of the Earth's largest reservoirs of bioactive carbon and is roughly equal in size to the stock of carbon in the atmosphere as CO_2 (approximately 700 Pg C) [43].

DOM is not truly *dissolved*, rather it is best described as a very fine suspension of organic particles. Indeed, the distinction between DOM and particulate organic matter (POM) is defined practically by whether material passes through a 0.45 μm filter (based on the smallest pore size of filters available when the definition was first adopted) [132]. This definition, while arbitrary, is useful as it separates most living organisms from individual molecules as in figure 1.6. [101].

Measurements of DOM generally fall into one of two categories: holistic or reductionist. Holistic studies focus primarily on total concentration or bulk properties that can be used to compare the entire DOM pool quickly and easily such as spectral absorbance or total DOC concentrations. Reductionist studies target specific sections of the total DOM pool by in depth analyses to relate these select measurements back to the properties of the bulk such as DOM chromatographic fingerprinting.

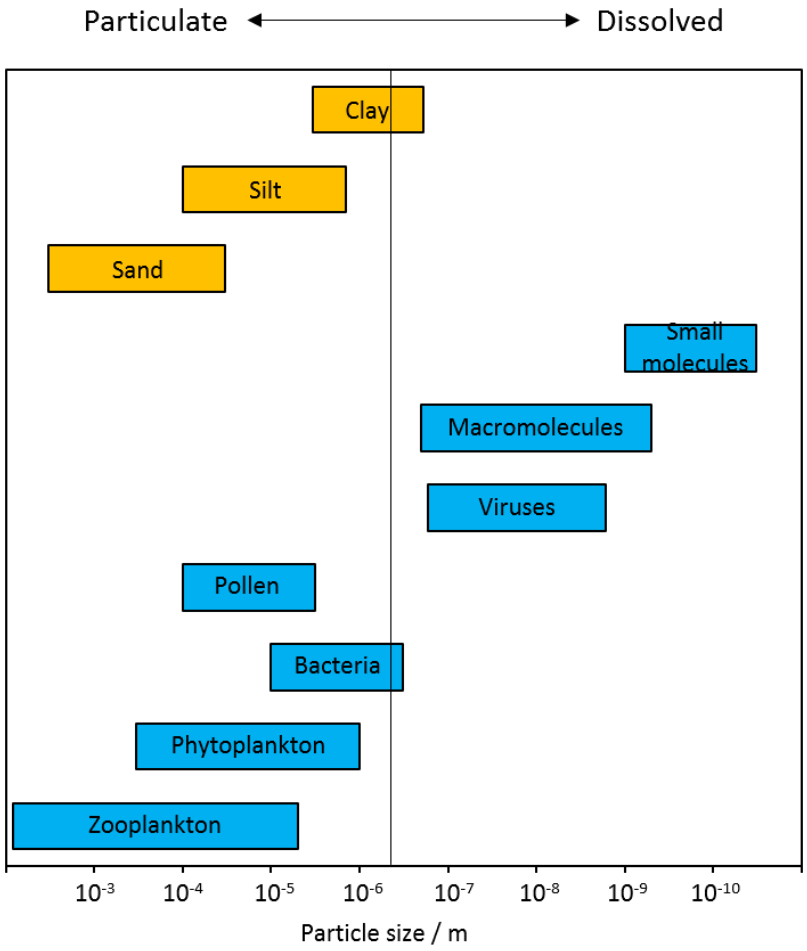

Figure 1.6: The continuation of sizes of organic matter (blue) and minerals (yellow) in seawater [43]

The largest source of marine DOM is the decay of phytoplankton comprising up to 40% carbohydrates and the rest made up of proteins and lipids [101]. Terrestrially sourced DOM comprises another large fraction of marine DOM from biomass degradation, soil organic matter, anthropogenic sources, etc. which may constitute up to 30% of the total marine DOM pool [42].

Several studies have been conducted investigating the extent to which DOM contributes to the reactive dry deposition of ozone at the SML including a series of model runs from Sarwar *et al.* [116] and lab studies from Martino *et al.* [81] and Shaw and Carpenter [120].

Martino *et al.* found that at concentrations of dissolved iodide and DOM representative of coastal marine systems ($[I^-]$ = 50-400 nM, [DOM] = 1-6 mg L^{-1}) the contributions to chemical enhancement of ozone deposition are similar, ranging between approximately 0.005 and 0.015 cm s^{-1} for both species [81]. Shaw and Carpenter measured the emission of I_2 from solutions of iodide and DOM that were exposed to ozone [120]. It was shown that the addition of DOM inhibited the formation of I_2 through the reaction of iodide and ozone though the ozone loss to DOC almost compensated for the decreased loss of ozone to iodide in these runs.

Sarwar *et al.* ran a series of sensitivity tests on the hemispheric Community Multiscale Air Quality model to determine the enhancement to reactive v_D by iodide, dimethyl sulfide (DMS), DOC and bromide (Br^-) [116]. It was found that the contributions of I^- and DOC to the total v_D were roughly the same (0.023 and 0.021 cm s^{-1}, respectively), the contribution of DMS was approximately 10 times less (0.002 cm s^{-1}) and the contribution of Br^- was approximately 35 times less ($\approx$0.0006 cm s^{-1}). The combined effect of these parameters was to increase the median ozone deposition velocity over the oceans by 0.040 cm s^{-1} compared to non-reactive deposition. It should be noted that the approach used to generate these values was very approximate and they are estimates only. The relative contributions of DOM and iodide to reactive dry deposition in the literature will be discussed further in chapter 4, section 4.1.

1.9 Aims of this project

The reactive dry deposition of ozone to the ocean surface is clearly a significant sink of tropospheric ozone, with the potential to influence the chemical processes occurring in both the marine and atmospheric environments.

It is evident from the literature that both dissolved iodide and DOM contribute significantly to reactive ozone loss at the ocean surface, though the uncertainties surrounding these processes are large. It is therefore the overarching aim of this work to reduce the uncertainties in the measurement and prediction of the contributions of dissolved iodide and DOM to v_D through laboratory studies of the kinetics of ozone loss to iodide solutions and measurement of ozone deposition onto solutions of unsaturated DOM, DOM with iodide and finally real SML samples.

Measurements of the second order heterogeneous rate constant for the reaction of gas phase ozone and dissolved iodide in the literature are sparse and show poor agreement with one another. In this work, a movable inlet flow reactor was designed, tested and optimised to gather kinetic information on the reaction of ozone with iodide. Values for the second order heterogeneous rate constant were measured empirically under several sets of experimental conditions and compared to the values presented in the literature.

Ozone deposition was measured onto synthetic seawater solutions containing either saturated or unsaturated organic surfactant molecules. Through the shape of the ozone uptake profiles with varying ozone exposure levels the mechanism of uptake was determined. The deposition of ozone onto unsaturated molecules with 1, 2 or 3 double bonds were compared to determine the effect of the degree of unsaturation on ozone uptake. Ozone deposition onto a synthetic seawater sample containing both an unsaturated organic molecule (oleic acid) and dissolved iodide was compared to the depositions recorded onto solutions of both components alone to investigate how the two reactive processes couple together.

Samples of SML and underlying water (ULW) were collected from the North Sea during the Microlayer At Night (MILAN) campaign of 2017 and from three cruises near to Bridlington in 2018. Inorganic iodine concentrations were measured for each sample and enrichment factors determined. By combining these measurements with the values for the second order heterogeneous rate constant of ozone and iodide, estimations were made for the contribution to dry deposition of ozone due to the reaction with iodide. Total ozone deposition was recorded in a similar way to the synthetic seawater samples and the mechanism of uptake was determined again. The total measured deposition was compared to calculated estimates for the contribution of iodide to the deposition and the relative contribution of DOM inferred. The correlations between ozone deposition and the other physical, chemical and biological measurements made during the MILAN campaign were determined and compared.

Chapter 2

Determination of the second order rate constant between O_3 and I^-

2.1 Mechanism of the reaction between ozone and iodide

Ozone deposition to the ocean surface is a significant sink of tropospheric ozone [30]; one of the most significant factors to marine ozone loss is via the heterogeneous reaction with dissolved iodide [80]. This reaction is of particular environmental importance not only when considering the loss of ozone to the marine atmosphere but also for the products formed in this reaction which can contribute to changes in atmospheric composition and reactivity [120].

The reaction between ozone and iodide can proceed via one of two pathways, either as an aqueous or surface reaction [95]. The aqueous reaction in the bulk-phase requires the dissolution of an ozone molecule into the overall solution prior to reaction and follows traditional second order kinetics [35]. The surface reaction, as described by Langmuir-Hinshelwood kinetics, requires an ozone molecule to adsorb onto the liquid surface but not be completely dissolved [113]. A recent review from Moreno *et al.* concludes that the the two pathways probably occur simultaneously though the surface reaction dominates in cases when the aqueous iodide concentration is high ($> 10^{-4}$ M) and the mixing ratio of ozone in the gas phase above the liquid surface is low ($<$ 80 ppm), otherwise the aqueous pathway dominates [95]. This would suggest that under normal natural conditions the reaction between ozone and iodide in seawater occurs via the aqueous reaction pathway.

The Gibbs free energy change of the aqueous reaction between ozone and a halide show that the reaction with iodide is the most energetically favoured as shown in table 2.1 [138]. The process of the aqueous iodide reaction with ozone is two step. First, dissolved ozone (figure 2.1) and iodide combine and an adduct intermediate is formed [113], see equation 2.2, followed by the release of molecular oxygen, see equation 2.3 [98]. This step is pH dependant; HOI is only formed when the pH is lower than 10 which is true for natural seawater conditions. The hypoiodous acid formed can react further with another equivalent of iodide to form molecular iodine, see equation 2.4. Thus in the overall

reaction, see equation 2.5, two equivalents of iodide react with one equivalent of ozone to form one equivalent of molecular iodine.

$$O_{3(g)} \longrightarrow O_{3(aq)} \tag{2.1}$$

$$I^-_{(aq)} + O_{3(aq)} \longrightarrow IOOO^-_{(aq)} \tag{2.2}$$

$$IOOO^-_{(aq)} + H^+_{(aq)} \longrightarrow HOI_{(aq)} + O_{2(aq)} \tag{2.3}$$

$$HOI_{(aq)} + I^-_{(aq)} + H^+_{(aq)} \longrightarrow H_2O_{(l)} + I_{2(aq)} \tag{2.4}$$

$$2\,I^-_{(aq)} + O_{3(aq)} + 2\,H^+_{(aq)} \longrightarrow O_{2(aq)} + H_2O_{(l)} + I_{2(aq)} \tag{2.5}$$

Table 2.1: Gibbs free energy change of the reaction between halides and ozone [138]

Halide	ΔG adduct formation / kJ mol^{-1}	ΔG O_2 release / kJ mol^{-1}
Fluoride	+25	+45
Chloride	+21	+4
Bromide	-8	+8
Iodide	-20	-3

2.2 Measurement of the ozone iodide rate coefficient

The rate coefficient for the reaction between ozone and iodide, $k_{O_3+I^-}$, can be calculated from measurements of ozone deposition to solutions of iodide at various concentrations [79].

The resistance method can be applied to the deposition of ozone to a reactive surface, with the overall deposition being controlled by multiple component resistances that combine to give a total resistance, such as adsorption, dissolution, bulk transfer or reaction, see equation 2.6 where v_D is the deposition velocity of the reactive species [35, 142].

$$R_{total} = v_D^{-1} \tag{2.6}$$

In a manner analogous to electrical circuits, deposition resistances can be considered and combined either in series or in parallel. An example of two resistances that occur in series are the resistance due to gas phase diffusion (often termed aerodynamic resistance) and the resistance due to the limit of solubility (often termed saturation resistance); these resistances are essentially independent of one another as they occur in different physical spaces on the pathway to deposition.

An example of two resistances that occur in parallel are the above mentioned saturation resistance and the resistance due to reaction in the bulk liquid. Both these resistances refer to processes that occur within the bulk liquid and directly impact one another, hence they are considered to occur in parallel.

In the case of ozone deposition to a reactive surface, the most important resistances to take into account are the aerodynamic resistance and the surface reaction resistance [31]. As these resistances refer to processes occurring in different locations they can be combined in series as in equation 2.7.

$$R_{total} = R_{surface} + R_{aerodynamic} \tag{2.7}$$

At an ozone mixing ratio of 200 ppb, the aqueous concentration of ozone, $[O_3]_{aq}$, can be estimated using the ideal gas law in equation 2.8 and Henry's law as approximately 2×10^{-9} mol L^{-1}. The dimensionless Henry's law constant for ozone at 293 K was estimated to be 3.90 using data from Helz and Kosak-Channing [64]. With sufficiently high concentrations of iodide (typically > 0.02 M [120]), pseudo first order reaction kinetics can be observed as in equation 2.9 where k_{obs} is the observed reaction rate constant, equal to $k[I^-]$, t is time and $[O_3]$ and $[O_3]_0$ are the measured gas phase ozone mixing ratios at time t and $t = 0$, respectively.

$$[O_3]_{(g)} = \frac{n}{V} = \frac{P}{R \times T} \tag{2.8}$$

$$-ln[O_3] = k_{obs}t - ln[O_3]_0 \tag{2.9}$$

Under psuedo first order reaction conditions, the half life of ozone at the surface, $t_{\frac{1}{2}(surface)}$, can be calculated using equations 2.10 and 2.11 where $t_{\frac{1}{2}(measured)}$ and $\frac{5}{6}t_{\frac{1}{2}(control)}$ are the measured half lives of ozone over a reactive solution and control solution, respectively. The ratio of $\frac{5}{6}$ is an experimentally determined factor [120]. Deposition velocity can then be calculated using equation 2.12 where V and A are the head space volume and surface area of the sample, respectively.

$$t^{-1}_{\frac{1}{2}(measured)} = \frac{ln(2)}{k_{obs}} \tag{2.10}$$

$$t^{-1}_{\frac{1}{2}(surface)} = t^{-1}_{\frac{1}{2}(measured)} - \frac{5}{6}t^{-1}_{\frac{1}{2}(control)} \tag{2.11}$$

$$v_D = \frac{V}{A} \times t^{-1}_{\frac{1}{2}(surface)} \tag{2.12}$$

For the deposition of ozone onto aqueous solutions of iodide, equation 2.13 can be used to estimate the surface resistance of a particular concentration of iodide and hence the second order rate coefficient [35].

$$R_{surface} = \frac{H}{\sqrt{kD[I^-]}} \tag{2.13}$$

In equation 2.13, H refers to the dimensionless Henry's Law constant, k refers to the second order rate constant and D refers to the diffusivity of ozone. Temperature dependant values for H and D were calculated from data in the literature for the experimental conditions used here of 293.15 K; $H = 3.9$ [64] and $D = 1.70 \times 10^{-9}$ m^2 s^{-1} [56].

It has been observed that the presence of additional dissolved species can alter the dissolution equilibrium for a particular compound, this is known as salting out [6]. Helz and Kosak - Channing measured the Henry's Law constant for ozone in aqueous solution at various temperatures and ionic strengths [64]. This relationship was summarised in equation 2.14, where K_H is the equilibrium constant for ozone dissolution in L atm mol^{-1}, T is the temperature in K and I is the ionic strength in mol dm^{-3}. K_H relates to the dimensionless Henry's law constant H by equation2.15, where R is the gas constant (0.0821 L atm K^{-1} mol^{-1}) and T is the temperature in K. Ionic strength can be calcuated from equation 2.16, where C is the concentration of ion i in mol dm^{-3} and z is the charge on ion i. For a simple 1:1 ionic species such as potassium iodide, the ionic strength is equal to to the molar concentration.

$$lnK_H = -1277T^{-1} + 2.659I - 688.0IT^{-1} + 12.19 \tag{2.14}$$

$$K_H = RTH \tag{2.15}$$

$$I = \frac{1}{2}\sum_{i=1}^{n} C_i z_i^2 \tag{2.16}$$

The impact of ionic strength on the Henry's law and equilibrium constants can be determined by calculating the percentage error between the ionic strength dependant equilibrium constants for a solution at a particular temperature and the ionic strength independent equilibrium constant where the I terms in equation 2.14 are set to zero. At iodide concentrations of 1×10^{-7} M and 1×10^{-5} M (the range of concentrations used in this kinetic study), the percentage error is equal to 3.50×10^{-6} % and 3.50×10^{-4} %, respectively. As at such low concentrations and ionic strengths the impact of salting out is so small, it is not necessary to take into account the ionic strengths in the values for Henry's law constants in equation 2.13.

2.3 Rate of reaction of iodide and ozone from previous work

The number of studies measuring the rate of reaction between ozone and iodide are few and far between, and with poor agreement between them. Garland *et al.* attempted to directly measure the second order rate constants between ozone and a range of salt species present in natural seawater at 298 K, but found the iodide ozone reaction occurred too quickly for them to measure. Instead a rate coefficient of 2×10^{9} M^{-1} s^{-1} was inferred from measurements of surface resistance to solutions of iodide [35]. No estimate of the uncertainty was provided for this value. Five concentrations of iodide were examined, three relatively high concentration samples (0.85, 0.17 and 3.4×10^{-2} M) and two low concentration samples (6.7×10^{-6} and 6.7×10^{-7} M). At the highest concentration levels the measured surface resistances were very low (0.05, 0.06 and 0.06 s cm^{-1} respectively) especially when compared to the aerodynamic resistance of the method ($R_a = 1.08$ s cm^{-1}).In these cases ozone deposition was limited by the aerodynamic resistance and the values for surface resistance were not reliable. In addition, predicted surface resistance values were calculated (0.03, 0.06, 0.15 s cm^{-1} respectively) in the work and compared to the measured values. These predicted values showed more spread than the

measured values and suggest that there is a large degree of uncertainty in these measurements.

Hu *et al.* measured ozone deposition onto four different solutions of iodide (approx. $0.5 - 3$ M) at 277 K yielding values of resistance of approx. $0.017 - 0.007$ s cm^{-1} [52]. A rate constant was then calculated to be 4×10^9 M^{-1} s^{-1}. The authors claim that this value is within experimental error of the value obtained by Garland, though these experiments were carried out at different temperatures, with this work being carried out under cooler yet more reactive conditions. Again, the iodide concentrations used in this work were quite high, suggesting a system with a very large aerodynamic component to the total measured resistance compared to the reactive resistance, indicating the method was less sensitive to ozone deposition.

Magi *et al.* conducted the only temperature-dependant study of ozone deposition onto solutions of iodide ranging from $276 - 293$ K [79]. As in the previous study, four solutions of iodide were used for each temperature dependent measurement ranging from $0.5 - 3$ M. A clear temperature dependence was observed showing an increase in the rate constant as temperature increases. The highest temperature examined in this study was lower than that used by Garland *et al.*, so while the rate constant for the highest temperature (2.4×10^9 M^{-1} s^{-1} at 293 K) was similar to the value Garland *et al.* obtained, extrapolating from the Arrhenius plot gave an estimated rate constant at 298 K of 4.09×10^9 M^{-1} s^{-1}, much higher than the value reported by Garland *et al.* for this temperature. The value reported by Magi *et al.* at 276 K (3.2×10^9 M^{-1} s^{-1}) is lower than the similar value reported by Hu *et al.* by over an order of magnitude suggesting some difference in the methods used to obtain these values has interfered with some of the results.

Liu *et al.* studied the second order rate constants for the reactions of ozone and five ionic species, including iodide [77]. The reaction rate for iodide was directly at 298 K measured by pulsed-accelerated-flow spectrometry as $1.2 \pm 0.1 \times 10^9$ M^{-1} s^{-1}. This estimate comes out lower than the other measurement at this temperature by Garland *et al.*, and the measurements are not within the

error of Liu *et al.*. If the temperature-dependant values obtained by Magi *et al.* are assumed to be correct, this value falls much lower than the extrapolated estimate mentioned above.

Shaw and Carpenter measured ozone loss to buffered solutions of iodide (5 and 10 $\times$ 10^{-6} M) at pH 8 and 293 K under psuedo first order reaction conditions. An estimate of the second order rate constant was determined to be 2.2 $\pm$ 0.9 $\times$ 10^{9} M^{-1} s^{-1} using the relationship stated in equation 2.13. This value is in reasonably good agreement with the data presented by Magi *et al.*, falling just within the lower bound of the uncertainty at this temperature. As this method of estimating the second order rate constant relies on a linear regression of the square root of [iodide] and the inverse of surface resistance, a potential source of error in this work is that only two different concentrations of iodide were studied.

The second order reaction between gaseous ozone and aerosol phase solutions of iodide as might be present in the marine atmosphere was investigated by Rouvière *et al.* [112]. Iodide aerosol was generated by nebulizing a 0.03 M solution of potassium iodide giving an aqueous concentration of iodide in the particle phase of 7.3 M. Ozone (70 - 300 ppb) was exposed to the aerosol stream using a movable injector line which could vary the reaction time between 2 and 25 s. Even though the concentration of iodide in the particle phase was very high, depletion of iodide within each particle was observed over the timescale of the experiment meaning the system could not be treated as operating under the simple pseudo first order kinetic case. In addition, as the products of the reaction have very different solubilities, the phase state of a particle may not stay constant during the experiment, further complicating the analysis. Instead a solver was used to model the differential equations of iodide ozonolysis and keep track of the iodide concentration in the particles over time. From many different fits of the model results, an average value was found for the second order rate constant of 1.0 $\pm$ 0.3 $\times$ 10^{9} M^{-1} s^{-1} at 293 K. This value is quite low, and only just overlaps uncertainty limits with the results at a similar temperature from Magi *et al.* and Shaw and Carpenter. This

low estimation could be because of the uncertainty in the iodide concentration in the particle phase during an experiment.

2.4 Aims of the work presented in this chapter

The aim of this work was to obtain an estimate for the second order heterogeneous rate constant between ozone and iodide in order to reduce the substantial uncertainty in this parameter.

A movable injector flow reactor was designed and tested to minimise the contribution of aerodynamic resistance to overall measured resistance and hence to maximise the sensitivity and accuracy of the derived rate constant.

2.5 A movable inlet flow reactor for the measurement of ozone deposition

A flow reactor was designed to simulate the exposure of a surface to ozone as a function of time (schematic and photo shown in figure 2.1) by moving a gas inlet line over the aqueous sample. In such a reactor, exposure time, t, is directly related to the flow rate of gas, f_{gas}, and headspace volume, V_{HS}, which itself is a function of the tube length, l, radius, r, and fill volume, V_{fill}, as in equation 2.17. Another important metric for gas-surface interactions is the surface area, A_s, to headspace volume ratio, where the surface area is calculated from the surface width, w, and tube length as in equation 2.18.

$$t = \frac{V_{HS}}{f_{gas}} = \frac{(\pi r^2 l) - V_{fill}}{f_{gas}} \tag{2.17}$$

$$\frac{A_s}{V_{HS}} = \frac{wl}{(\pi r^2 l) - V_{fill}} \tag{2.18}$$

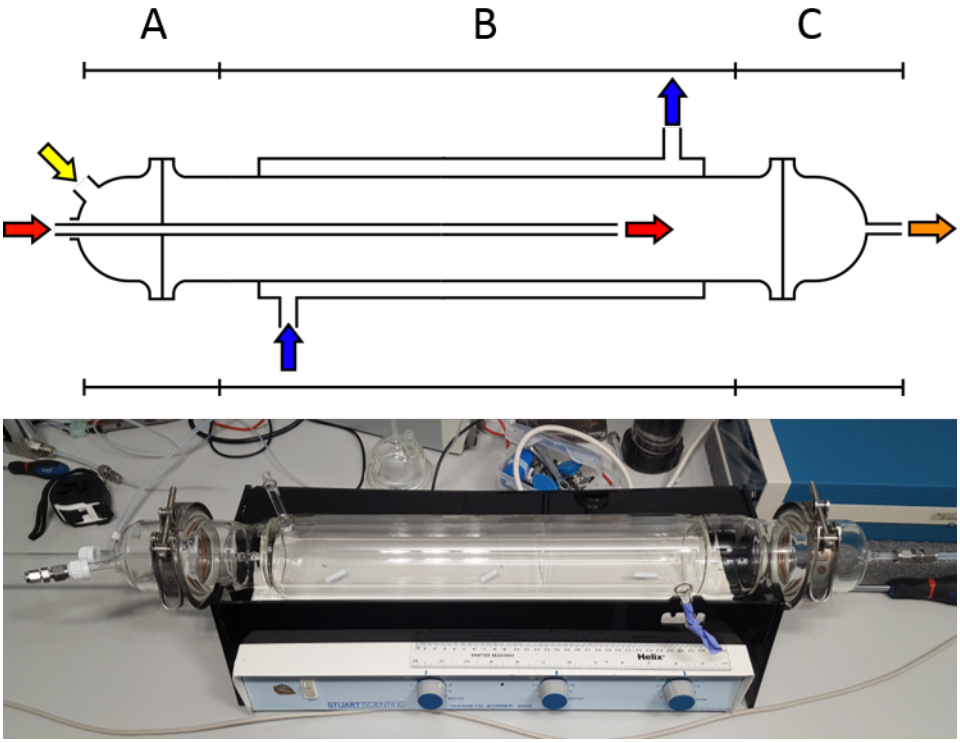

Figure 2.1: Movable injector flow reactor: top, a schematic showing the different sections of the reactor (A: inlet cap and flange, B: main temperature controlled tube body, C: outlet cap and flange) and the flow paths of ozone through the movable inlet line (red arrows), carrier gas into the reactor (yellow arrow), outlet gas from the reactor (orange arrow) and coolant solution through the temperature control jacket (blue arrows); bottom, a photo of the flow reactor

Table 2.2: Dimensions of the sections of the flow reactor

Section	Length / mm	Diameter / mm
A	100	62.0
B	507	62.2
C	100	62.0

The reactor featured a segmented design with the main body of the tube being open ended so end caps could be attached with any inlet/outlet ports as necessary. The main body of the tube also had a glass jacket that could be flushed with fluid to regulate the temperature inside the reactor. The inlet end cap had two gas tight ports, one positioned at an angle connected to the carrier gas and the other in the centre of the cap allowed the movable inlet line to enter the reactor. The inlet line was supported inside the tube by a small PTFE stand that braced the end of the inlet line against the walls of the flow reactor. To maintain the balance of the inlet line, a second stand was used outside the flow reactor body to prevent the line from sagging under its own weight and the weight of the gas fittings.

The primary outlet cap had only one port for the exit of gases from the reactor, though if needed other caps could be fitted for other purposes. Liquid samples (270 mL) were added to the tube using a syringe through the carrier gas port (seen on the left of figure 2.1). Samples were stirred gently using three magnetic stirrer bars so to mix the sample without distorting the surface shape. The inner diameters of the different sections of the tube were measured using calipers so the headspace volume could be calculated for any position inside the tube for use in equation 2.12. The average diameter of the reactor was 62.1 $\pm$ 0.1 mm.

The surface area of the aqueous sample was calculated from the length of the reactor, l, and the width of the surface layer, w. The surface width was obtained from the cross sectional area taken up by the sample as shown in figure 2.2, where d and r are the diameter and radius of the reactor respectively,

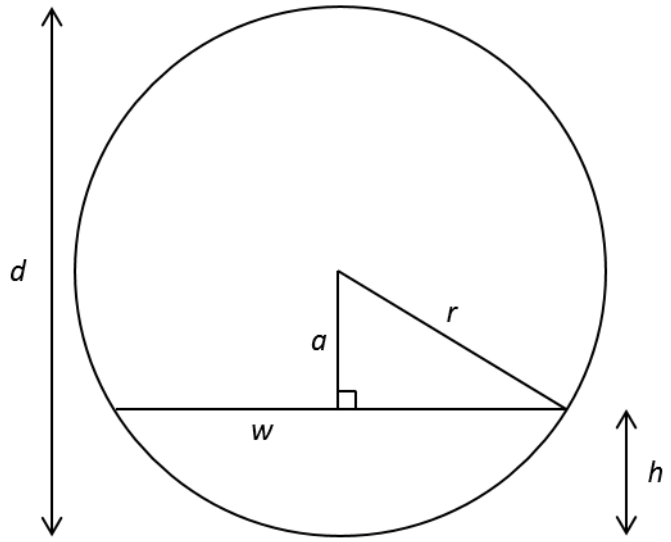

Figure 2.2: Schematic of a cross section of the flow reactor in profile

h is the height of the sample in the reactor and a is the distance between the centre of the reactor and the the height of the samples such that the radius is equal to the sum of the sample height and the distance a, equation 2.19.

$$r = h + a \tag{2.19}$$

The proportion of the cross sectional area taken up by the sample is equal to the ratio of the volume of the liquid sample to the total volume of the reactor, equation 2.20. The cross sectional area of the sample, A_l, is related to the height of the sample, h and the tube radius by equation 2.21. The width of the surface of the sample can be calculated using simple trigonometry as in equation 2.22.

$$\frac{V_l}{V_t} = \frac{A_l}{A_t} \tag{2.20}$$

$$A_l = r^2 cos^{-1}\left(\frac{r-h}{r}\right) - (r-h)\sqrt{2rh - h^2} \tag{2.21}$$

$$r^2 = x^2 + \left(\frac{w}{2}\right)^2 \tag{2.22}$$

In a tube of radius 3.105 ± 0.025 cm and length 70.7 ± 0.05 cm, at a fill level of 270 ± 2 mL and with a total tube volume of 2141 ± 35 mL, A_l was calculated to be 3.82 ± 0.09 cm^2. Rather than rearranging equation 2.21 to find an expression for h in terms of A_l, the Goal Seek function of Microsoft Excel was used to brute force a value for h via trial and error given the value for A_l and equation 2.21. This gave a value for h of 1.14 ± 0.03 cm with an error margin in the Goal Seek estimate of A_l of 0.0005%. Using equation 2.22, the surface width was found to be 4.81 ± 0.11 cm giving a total surface area in the tube of 340.1 ± 1.5 cm^2. From this, a total surface area to headspace volume ratio can be calculated as 0.182 ± 0.003 cm^{-1}.

All errors here were calculated using the propagation of errors method that assumes that if some quantity, y, can be expressed as a function of independent variables, $y = f(x_1, x_2 \ldots x_i)$, each with an associated error, σ_{x_i}, then the error in y, σ_y, can be calculated using equation 2.23.

$$\sigma_y^2 = \sum_{i=1}^{n} \left(\frac{dy}{dx_i} \sigma_{x_i} \right)^2 \tag{2.23}$$

2.6 Ozone generation and detection

Ozone was generated using a pen ray lamp (UVP ltd.). Compressed air was passed through a moisture trap and a hydrocarbon filter and then through a quartz tube next to the lamp. Shortwave UV light (185 nm) converted oxygen gas in the air flow into ozone. The ozone mixing ratio was controlled by covering or exposing part of the lamp with a metal sheath.

Ozone was detected using an ozone monitor (model 205B, 2B Technologies) connected to the outlet of the flow reactor (shown by the orange arrow in figure 2.1). The line was opened up to the lab air through a charcoal filter to maintain atmospheric pressure within the system. Ozone mixing ratios were recorded by the instrument every two seconds. For each position of the inlet line in the reactor data was collected for 5 minutes while the signal stabilised then an

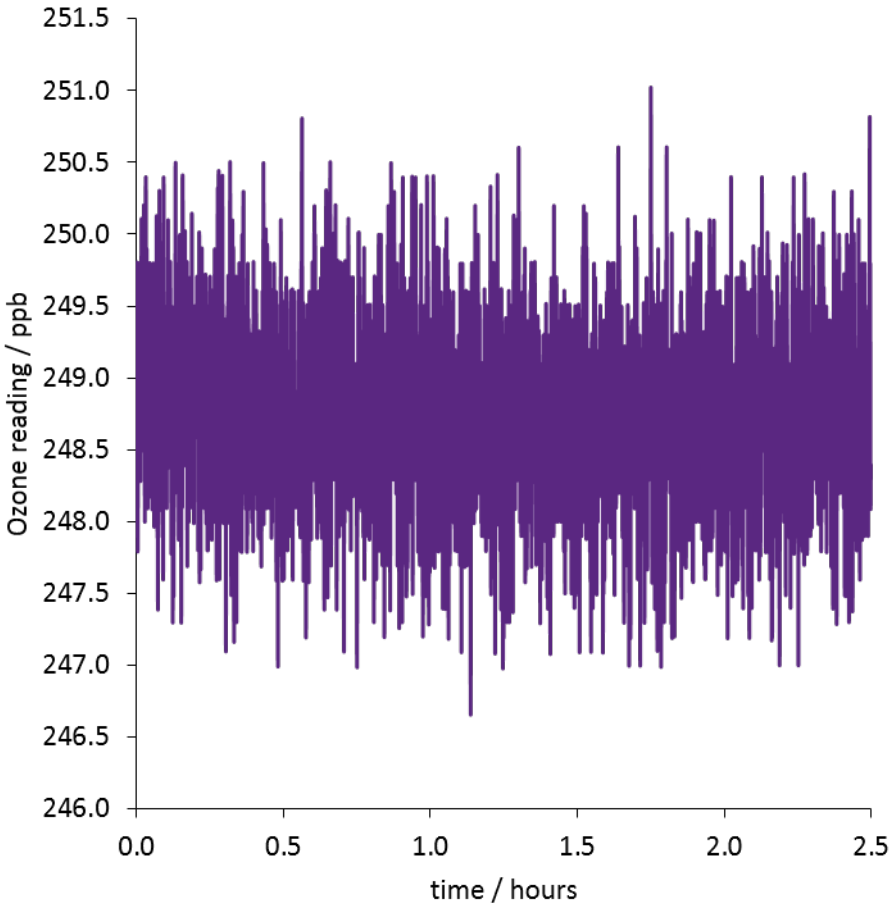

Figure 2.3: Measured ozone mixing ratios through an empty flow reactor over 2.5 hours, average ozone = 248.7 ± 0.6 ppb

average mixing ratio was calculated with data from at least 10 further minutes.

The drift of the ozone generator and monitor was measured. A position was chosen at random on the ozone generator and the reading measured on the ozone monitor over 2.5 hours, figure 2.3. In this experiment, 4498 individual measurements were made averaging at 248.7 ± 0.6 ppb, an error of only 0.24 %.

2.7 Control experiment in the flow reactor

Prior to the analysis of iodide solutions, a control experiment was run with LCMS grade water (270 mL) only in the flow reactor to determine whether

any ozone loss could be observed due to dissolution in the water or loss to the walls of the reactor. The control experiment was carried out with a flow rate of ozone through the tube of 1000 sccm, which will be referred to in the rest of this work as F2 flow conditions. Two repeats were carried out by making a forward and reverse pass over the sample with the inlet line. Figure 2.4 shows the ozone measured in the flow reactor at different exposure times during the control experiment.

It can be observed from figure 2.4 that there is no observable decrease in the ozone signals measured in the flow reactor over the exposure times examined. As it is unlikely that there is no wall losses or dissolution of ozone occurring at all, this could be explained by the system not being sensitive enough to ozone change to register these small losses or that the system reached equilibrium on a timescale far shorter than that of the experiment. Applying a linear regression to all this data together gives a line best fit of equation $y = 0.0452x + 213.3$ with an R^2 of 0.4568. The low value of R^2 suggests that a linear trendline is not an appropriate way to model this data, which is to be expected for a system where no trend is predicted. It is therefore assumed here that the control half life is equal to zero thus equation 2.11 becomes:

$$t^{-1}_{\frac{1}{2}(surface)} = t^{-1}_{\frac{1}{2}(measured)} \tag{2.24}$$

2.8 The optimisation of flow characteristics in the flow reactor

As shown in equation 2.7, the total resistance, which is the measured variable, is equal to the sum of the surface and aerodynamic resistances. Minimising the aerodynamic resistance by changing the flow conditions should lead to the surface reaction resistance being a larger component of the total measured resistance indicating that the method is more sensitive to the reaction.

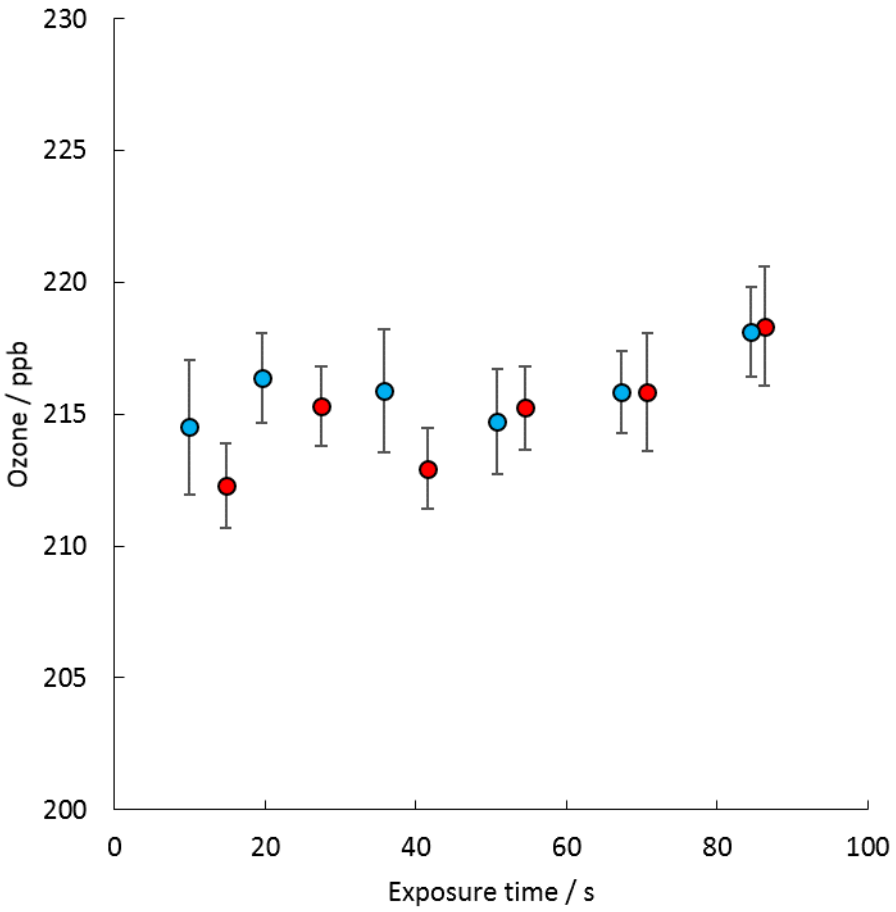

Figure 2.4: Control experiment showing ozone levels at different exposure times in the flow reactor with LCMS grade water only under F2 flow conditions. Different colours are separate repeats, error bars are one standard deviation of the mean of at least 5 minutes of data

In order to maximise the sensitivity of the flow reactor method to the surface reaction between ozone and iodide, a series of optimisation experiments were carried out under different flow conditions. All experiments were carried out at room temperature (293 K). The ideal flow conditions for the tube would be those that minimise the aerodynamic resistance to ozone deposition, that is the resistance caused by the ozone diffusing to the liquid surface, so that the largest possible contribution is made by the surface reaction resistance to the total measured resistance as shown in equation 2.7. Aerodynamic resistance values for each of these flow systems were obtained by measuring the ozone deposition over solutions of high concentration iodide (0.02 and 0.10 M) where the surface reaction resistance is assumed to be essentially equal to zero [120]. The different flow rates for each set of flow conditions are given in table 2.3.

In addition to exploring different flow rates in the system, four different movable injection inlet lines (as shown in figure 2.1) were used in the aerodynamic tests; a glass tube ending in a glass sinter similar to that found in a gas bubbler (figure 2.5A), an open tube with a Teflon cap sealed at the end with 20 holes perpendicular to the length of the tube (figure 2.5B), an open ended tube (figure 2.5C) and a sealed glass tube with several randomly distributed holes perpendicular to the length of the tube (figure 2.5D). These tests were carried out to determine which of these designs would best facilitate the dispersion of ozone in the reactor.

It can be seen from the data in table 2.4 that the open tube gas inlet line used in the initial conditions (experiment 1) gave one of the highest aerodynamic resistance values of 4.09 s cm^{-1}. Changing to the other gas inlet lines provided some improvement, with the best results being observed using the holed glass inlet under F11 conditions (experiment 16, R_a = 2.41 s cm^{-1}). Three repeats were run under these conditions and also under the F9 and F10 conditions to compare the impact of changing the ratio of carrier to ozone flow rate whilst keeping the total flow rate through the tube consistent. The average aerodynamic resistance for F9, F10 and F11 conditions were calculated to be 3.53 $\pm$ 0.25, 2.69 $\pm$ 0.19 and 2.64 $\pm$ 0.25 s cm^{-1}, respectively. This suggests

Table 2.3: Flow rates for each of the flow systems investigated in the testing of the flow reactor

Flow system	O_3 flow rate / sccm	Carrier flow rate / sccm	Total flow rate / sccm
F1	500	0	500
F2	1000	0	1000
F3	400	600	1000
F4	600	400	1000
F5	800	200	1000
F6	625	625	1250
F7	900	600	1500
F8	1200	300	1500
F9	400	1600	2000
F10	1000	1000	2000
F11	1600	400	2000
F12	1660	840	2500
F13	2000	500	2500
F14	2000	1000	3000
F15	2400	600	3000

Table 2.4: Results of the aerodynamic resistance tests under various flow conditions

#	Inlet Line	[Iodide] / M	Flow System #	R_a / s cm^{-1}
1	Open tube	0.02	F2	4.09
2	Holed glass	0.1	F4	3.71
3	Holed glass	0.02	F5	3.49
4	Holed glass	0.1	F5	3.30
5	Holed glass	0.1	F7	3.23
6	Holed glass	0.1	F7	3.45
7	Holed glass	0.1	F8	3.13
8	Holed glass	0.1	F8	3.06
9	Holed glass	0.1	F9	3.76
10	Holed glass	0.1	F9	3.27
11	Holed glass	0.1	F9	3.56
12	Holed glass	0.1	F10	2.90
13	Holed glass	0.1	F10	2.54
14	Holed glass	0.1	F10	2.62
15	Holed glass	0.1	F11	2.87
16	Holed glass	0.1	F11	2.41
17	Holed glass	0.1	F11	2.45
18	Holed glass	0.1	F11	2.83
19	Holed glass	0.1	F15	2.91
20	Sinter	0.02	F5	3.93
21	Sinter	0.02	F6	4.40
22	Teflon Cap	0.1	F8	3.50
23	Teflon Cap	0.1	F8	3.07
24	Teflon Cap	0.1	F11	2.95
25	Teflon Cap	0.1	F11	3.60
26	Teflon Cap	0.1	F12	4.07
27	Teflon Cap	0.1	F13	3.74
28	Teflon Cap	0.1	F14	3.41
29	Teflon Cap	0.1	F15	3.25

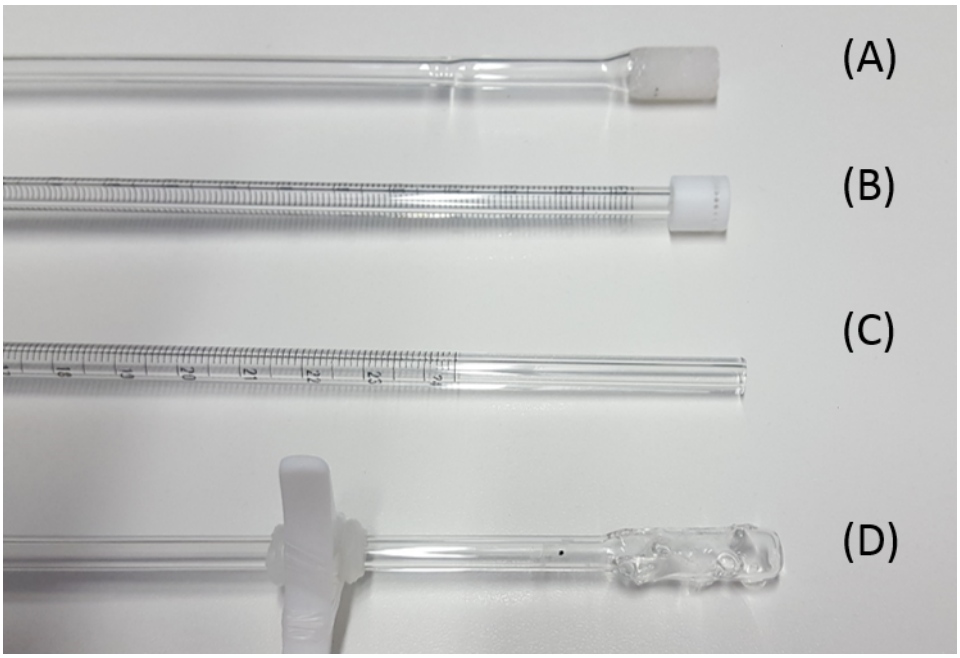

Figure 2.5: The four different inlet lines tested for the optimal flow conditions, (A) sintered glass, (B) Teflon cap, (C) open tube and (D) glass holes

that increasing the proportion of the flow through the ozone inlet reduces the aerodynamic resistance, though there is a high level of uncertainty suggesting little measurable difference between the F9 and F11 conditions.

In general, it appeared that the glass holes gas inlet line gave the greatest improvement over the original open ended tube and the lowest measured values of R_a. For this reason, the glass holes inlet was selected to be used for all subsequent experiments.

2.9 Dead space volume around the flow tube inlet

To investigate how well the ozone and carrier gases mixed inside the flow reactor, a second movable line was added to the outlet of the tube beneath the inlet line to monitor the profile of O_3 along the flow tube around the injection region. This new outlet was at a similar height in the tube to the surface of the liquid sample. To avoid disturbing the internal flow of the tube with

the suction from the ozone monitor pump the flow to the ozone monitor was restricted to 200 sccm. To ensure the pump was operating under atmospheric pressure, an ozone scrubber was connected to the monitor inlet line through which air was drawn from the surroundings to make up the rest of the flow (note: the total flow demand into the monitor was 2.54 SLM). The remainder of the gas flow exited the tube from the regular gas outlet which was connected directly to an ozone scrubber. As the distance between the inlet and outlet was changed, the ozone concentration was recorded. Figure 2.6 shows the ozone levels recorded around the ends of the inlet under F9, F10 and F11 systems.

It can be seen from figure 2.6 that under F11 conditions, the ozone reading appears to be well mixed for all positive distance values (i.e. downstream of the inlet). However, a large amount of retro-diffusion behind the inlet line was observed for F11 conditions, with the furthest data point 186 mm behind the inlet still giving a positive ozone reading. This suggests that under these conditions, the carrier gas was not being effective in 'pushing' the gas from the movable inlet line forward through the tube. A better case was observed for the F10 flow system, with a zero ozone reading being recorded at 70 mm behind the inlet and a stable ozone level being recorded at all positive distances. An unexpected reading was observed at a distance of 0 mm, i.e. when the movable outlet was positioned just below the end of the inlet line with a reading 13 ppb lower than the stable final reading. This could be due to the random positioning of the holes at the end of the inlet line creating several small scale jets of ozone that are only observable at very small distances. Under F9 conditions, a zero reading was observed at just 36 mm behind the inlet, suggesting that the carrier gas was effective at moving the gas coming out of the movable inlet line. However the O_3 readings after the inlet showed increasing O_3 mixing ratios out to 146 mm, followed by a decrease in $[O_3]$. This indicates that under these flow conditions ozone is not well mixed in the tube.

From these tests, F10 flow conditions were considered optimal of the flow conditions studied although containing a degree of undesired retro-diffusion.

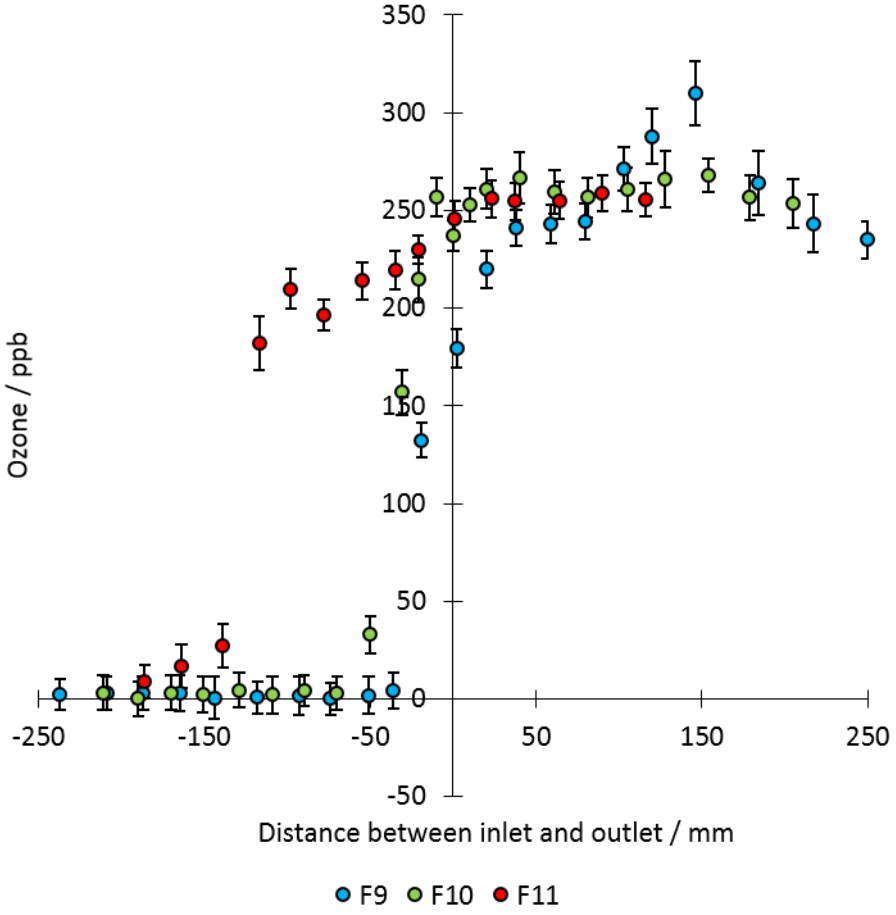

Figure 2.6: Retro-diffusion spatial profiles measured in the flow reactor around the end of the inlet at 250 ppb ozone line under F9 (blue), F10 (green) and F11 (red) flow conditions. Error bars show one standard deviation of the mean of at least 5 minutes of data

The impact of ozone mixing ratio on the dead space volume resulting from retro-diffusion was monitored under F10 flow conditions as shown in figure 2.7.

Modelled fits were calculated for the data in figure 2.7 using equation 2.25 where β is the minimum point of the curve, (defined here as 0 ppb), L is the maximum height of the curve (defined here as the average measured O_3 mixing ratio after stabilisation), T is the constant of asymmetry, k is the slope of the curve and x_0 is the midpoint of the curve (estimated here as the halfway point between the last zero reading and the first stable maximum reading). Values for T, k and x_0 were varied for each fit using Microsoft Excel's Goal Seek to give the lowest possible residuals. These values for the modelled fits are given in table 2.5.

$$[O_3] = \beta + \frac{L}{(1 + Te^{-k(x-x_0)})^{1/T}} \tag{2.25}$$

Once an equation was known for each profile, an estimate for the retro-diffusive distance (RTD), i.e. the distance behind the inlet that ozone can be measured, could be calculated. As the ozone concentration behind the inlet was not constant, this distance was estimated by integrating the curve between 0 and -100 mm (to find the total ozone behind the inlet) and dividing by the maximum ozone concentration (L) to find the width of the rectangle of equal area. Estimates for the RTD are given in table 2.5.

It can be seen from the data in table 2.5 that the modelled fits match the data well with the lowest R^2 value being calculated to be 0.9676. From figure 2.7 it can be seen that the curves all have very similar shapes and appear to stabilise at the L ozone level and reach 0 ppb at similar positions around the inlet. In addition, the calculated limits of retro-diffusion are relatively similar giving an average RTD of 47.38 ± 4.50 mm. Under the F10 flow conditions, this is equal to an additional 3.76 ± 0.36 s of ozone exposure at any point in the flow reactor.

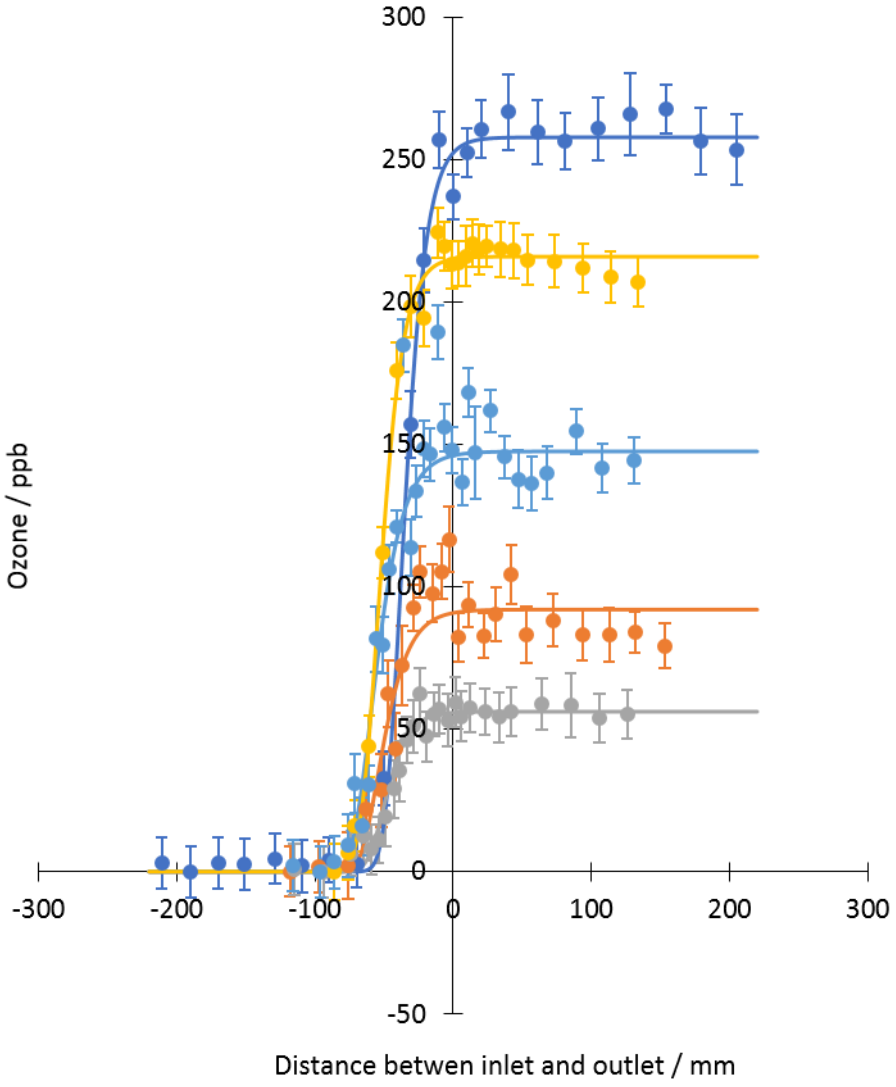

Figure 2.7: Retro-diffusion spatial profiles measured in the flow reactor around the end of the inlet under F10 flow conditions with varying ozone levels (each colour is a different exposure). Error bars are one standard deviation of the mean of at least 5 minutes of data

Table 2.5: Variables for the modelled fits for the retro-diffusion profiles under F10 flow conditions and variable ozone levels

L / ppb	T	k	x_0	R^2	RTD / mm
56.2	0.2076	0.1023	-50.33	0.9936	45.79
92.0	0.0008	0.0802	-54.50	0.9676	47.45
147.6	0.0602	0.0777	-59.40	0.9736	52.49
216.0	0.3019	0.1016	-54.45	0.9891	50.37
257.9	0.2076	0.1023	-37.60	0.9965	40.79

To account for the extra exposure time in the flow reactor due to retro-diffusion, equation 2.9 can be rewritten in the form: $y = m(x + a) + c$, as shown in equation 2.26 where t_{RTD} is the additional exposure time due to retro-diffusion. By multiplying out the brackets, as in equation 2.27, it can be seen that by including the additional exposure time due to retro-diffusion the gradient of a $ln[O_3]$ vs t graph is still equal to the observed pseudo first order rate constant, k_{obs}.

$$ln[O_3]_x = -k_{obs}(t_x + t_{RTD}) - ln[O_3]_0 \tag{2.26}$$

$$ln[O_3]_x = -k_{obs}t_x - (k_{obs}t_{RTD} + ln[O_3]_0) \tag{2.27}$$

It can therefore be seen that that the magnitude of the limit of retro-diffusion will have no impact on the results obtained using the flow reactor as values for resistance are calculated only from the gradient of the first order log plot and the RTD affects only the intercept.

2.10 Ozone deposition to solutions of iodide in a flow reactor

In addition to the aerodynamic resistance and retro diffusion tests, four sets of flow conditions were selected for a more detailed test with multiple solutions of iodide at concentration levels where there would be a surface component to the resistance to ozone deposition. A summary of these flow conditions is given in table 2.6. The glass holes gas inlet line was used in all cases.

Table 2.6: Flow conditions used in ozone deposition to iodide experiments

Flow system	O_3 flow rate / sccm	Carrier flow rate / sccm	Total flow rate / sccm
F1	500	0	500
F2	1000	0	1000
F10	1000	1000	2000
F11	1600	400	2000

The goal of flow system optimisation was to maximise usability and sensitivity; these flow systems were selected for a more comprehensive analysis and comparison with iodide/resistance profiles for the reasons listed below. F2 was selected as it was the starting point for the flow optimisation process. F1 was selected because it had the lowest total flow rate and therefore the maximum exposure time, which was hypothesised to lead to the greatest ΔO_3. F11 was selected because it gave the lowest aerodynamic resistance of those tested (2.56 cm^{-1} s). F10 was selected because it gave a low aerodynamic resistance (2.69 cm^{-1} s) and a low limit of retro-diffusion (6 cm). A low aerodynamic resistance would give a higher proportion of the total resistance (and therefore also ΔO_3) corresponding to the surface chemistry, which would indicate a better sensitivity.

For each concentration of iodide (n = 4−5), several repeats (n = 2−4) were carried out by making another pass of the inlet line over the sample. For each

repeat, the measured ozone mixing ratio at each exposure time was plotted and a line of best fit found using the weighted least squares method where the standard deviations of each ozone measurement were used as weights. The gradients of the lines of best fit were used to calculate surface resistances for each repeat by assuming pseudo first order kinetics as shown in equations 2.6 − 2.12 [120]. All experiments were carried out at 293 K.

Once a surface resistance had been calculated for each line of best fit, these were then averaged to give a mean surface resistance for each iodide measurement. As an example, a comparison between each of the flow systems at $[I^-] = 1 \times 10^{-6}$ mol dm^{-3} is shown below in figures 2.8 − 2.11.

For many of the iodide solutions examined, one of the repeats gave a line of best fit with a gradient quite different to the others as in figure 2.8 ($m_1 = -0.00601$, m_2 -0.00705, m_3 -0.00454). In these cases, the decision was made not to discard the most extreme data point from the average as the number of repeats was too low to determine if it was an outlier. The R^2 values for each repeat are generally quite high (> 0.95) indicating that lines of best fit fit the trends of the data well.

To check the quality of the results, the square root of the iodide concentration was plotted against the inverse of the measured surface resistance. These two values should have a linear relationship according to equation 2.13. Lines of best fit were calculated again using the weighted least squares method, with the standard deviation of the replicates of each measurement used as weights.

From figure 2.12, it can be seen that F1, F10 and F11 conditions all give very similar results, with a much larger resistance shown for the original conditions F2. In theory, the flow conditions of these experiments should not have any impact on the surface resistance as, by definition, these effects are accounted for in the aerodynamic resistance term of equation 2.7. It is possible then that this difference was produced by experimental error in the preparation of the sample solutions. For all future analysis, this data is discarded as an outlier.

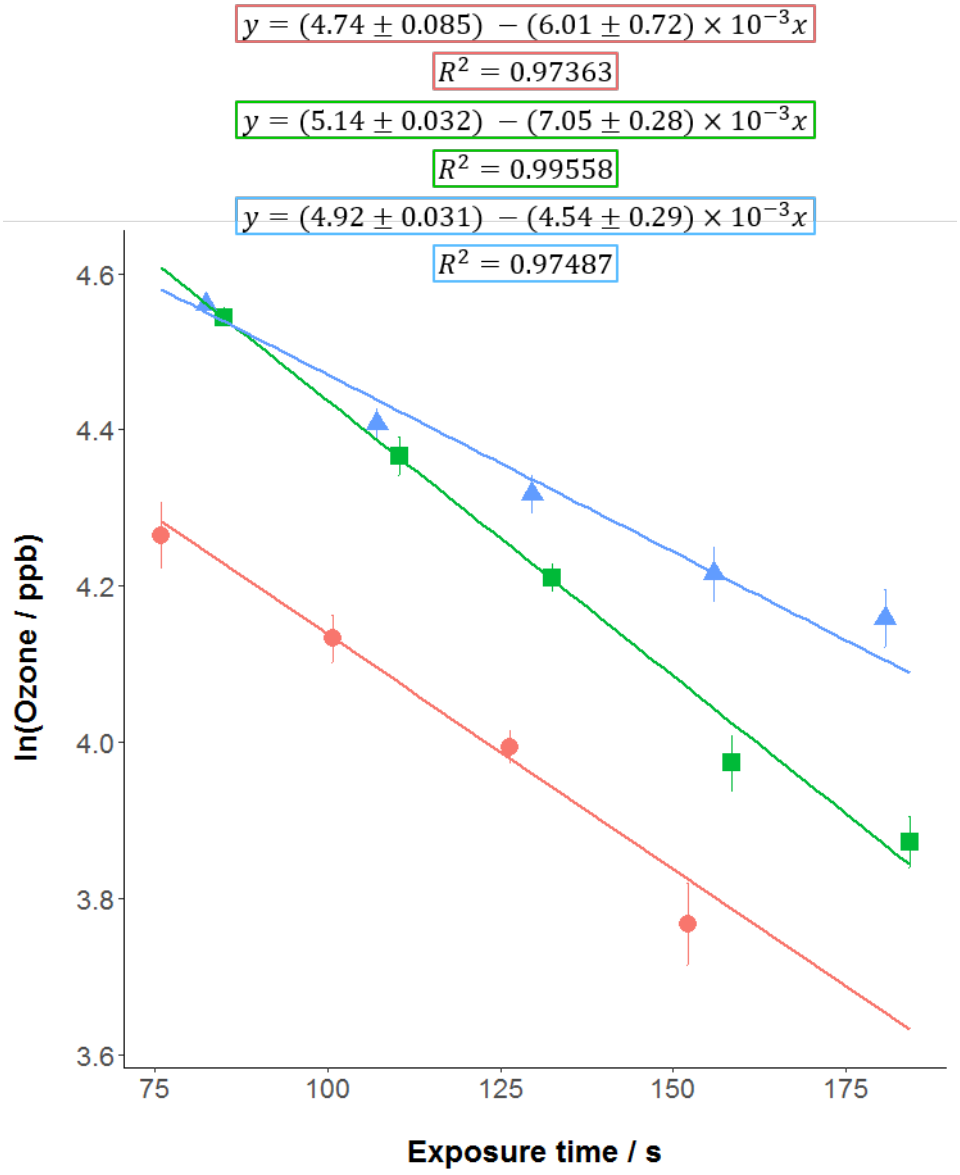

Figure 2.8: Measured ozone mixing ratios at different exposure times for a solution of iodide at 1×10^{-6} mol dm^{-3} under F1 flow conditions at 293 K. Error bars are calculated from the standard deviation of the average ozone measurement for each exposure time using at least 5 mins of data. Gradient and intercept ranges are the standard error as produced in a weighted least squares regression

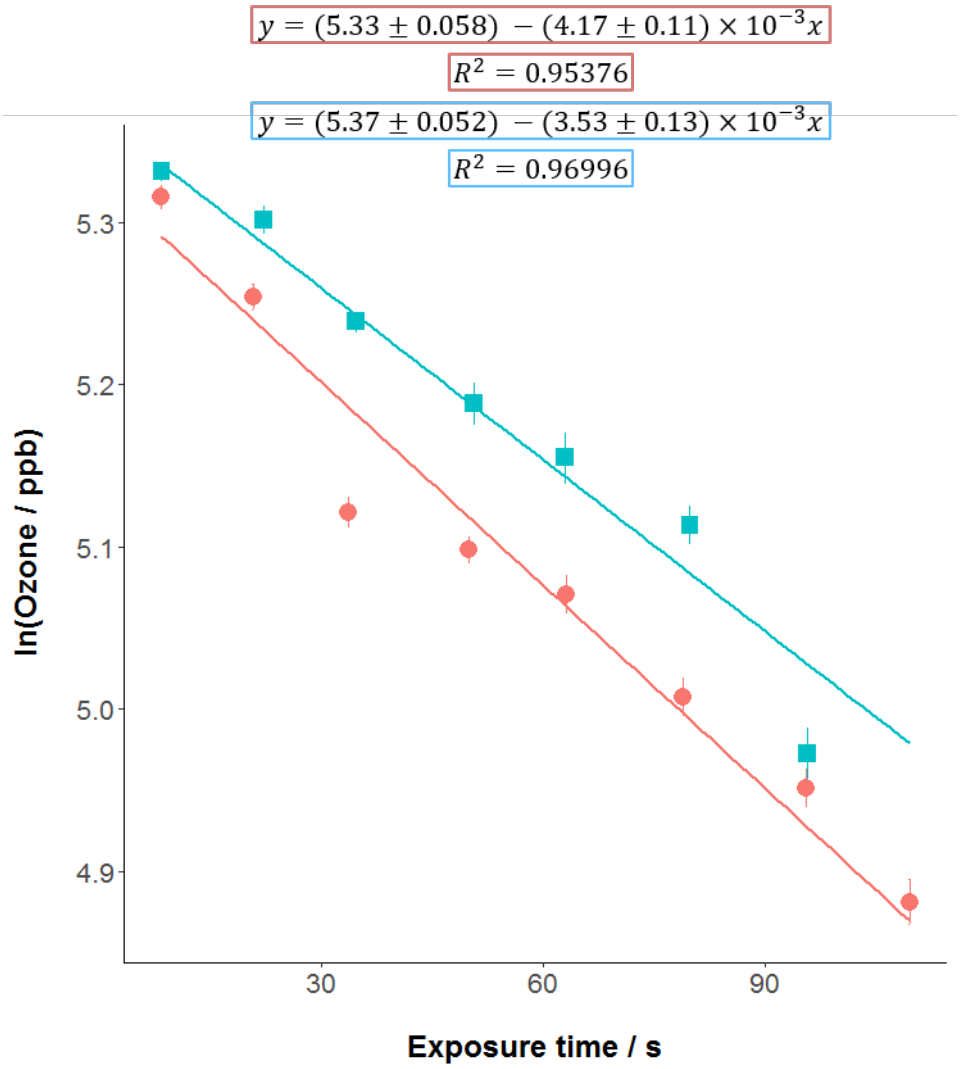

Figure 2.9: Measured ozone mixing ratios at different exposure times for a solution of iodide at 1×10^{-6} mol dm^{-3} under F2 flow conditions at 293 K. Error bars are calculated from the standard deviation of the average ozone measurement for each exposure time using at least 5 mins of data. Gradient and intercept ranges are the standard error as produced in a weighted least squares regression

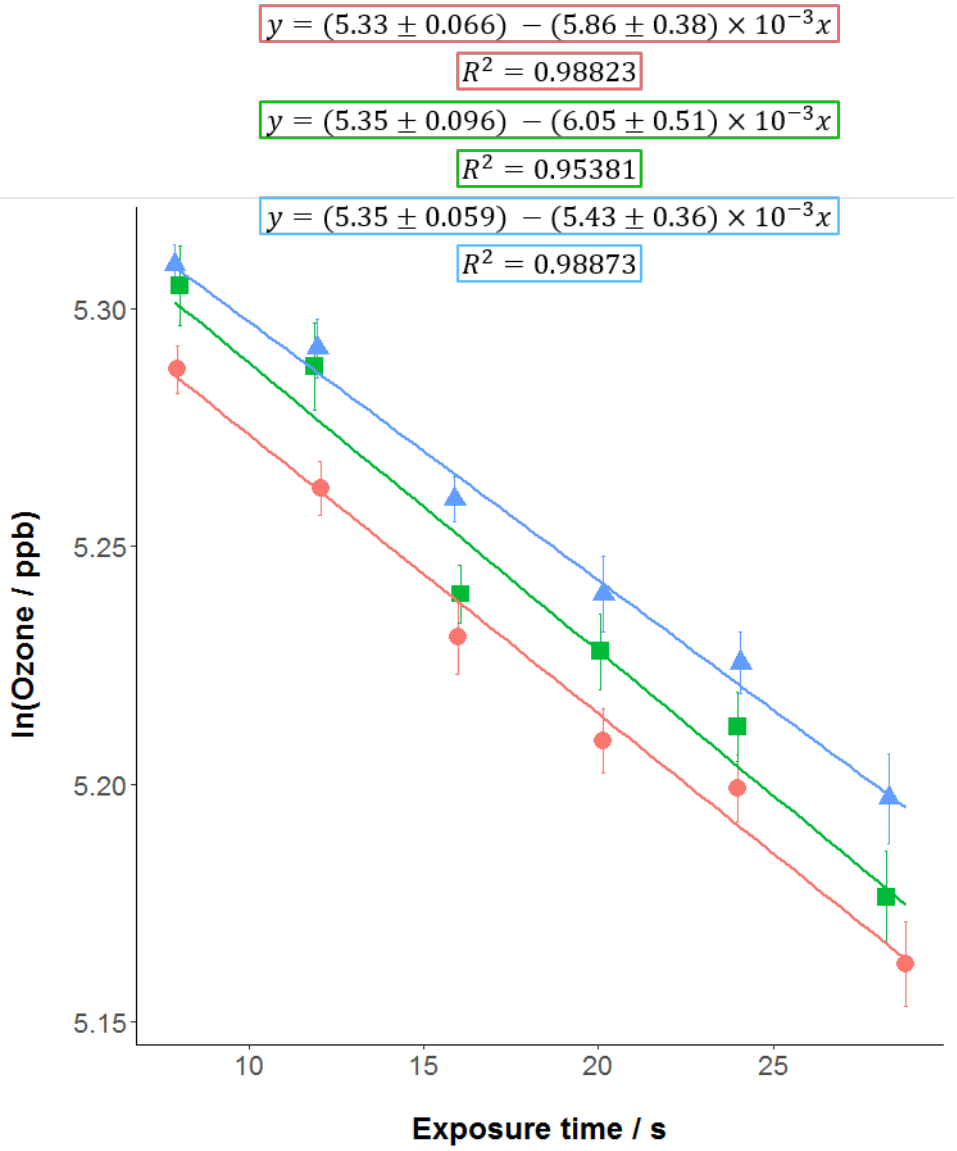

Figure 2.10: Measured ozone mixing ratios at different exposure times for a solution of iodide at 1×10^{-6} mol dm^{-3} under F10 flow conditions at 293 K. Error bars are calculated from the standard deviation of the average ozone measurement for each exposure time using at least 5 mins of data. Gradient and intercept ranges are the standard error as produced in a weighted least squares regression

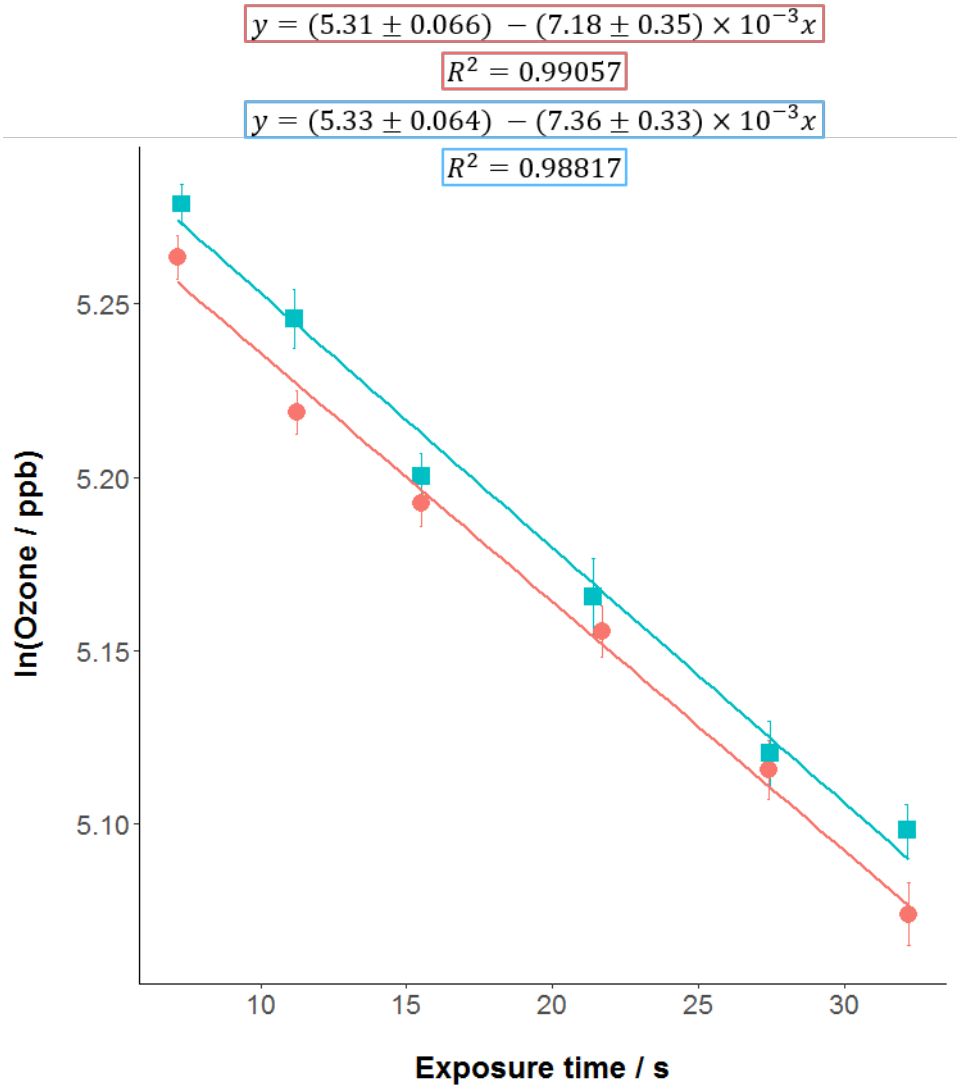

Figure 2.11: Measured ozone mixing ratios at different exposure times for a solution of iodide at 1×10^{-6} mol dm^{-3} under F11 flow conditions at 293 K. Error bars are calculated from the standard deviation of the average ozone measurement for each exposure time using at least 5 mins of data. Gradient and intercept ranges are the standard error as produced in a weighted least squares regression

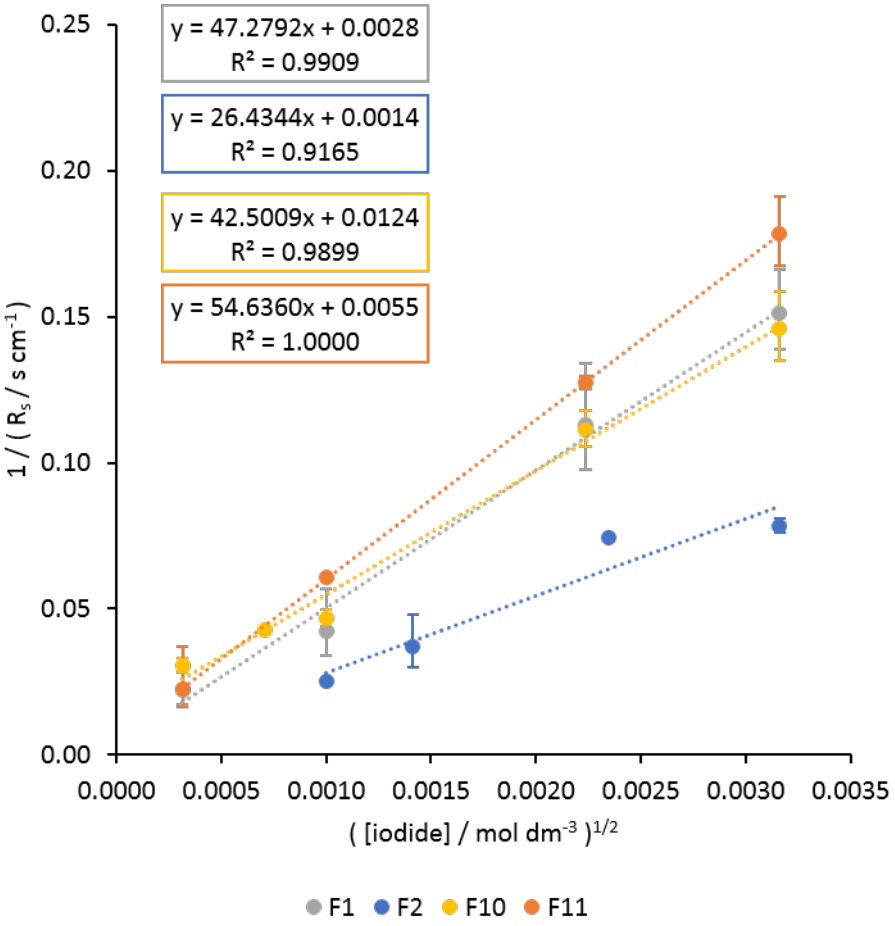

Figure 2.12: Measured and predicted surface resistance at varying iodide concentrations for four different sets of flow conditions at 293 K. Error bars are calculated from the standard error of the gradients of the ozone/exposure time log plots

The gradients of the lines of best fit for F1, F10 and F11 in figure 2.12 can be used to calculate an estimate for the second order rate constant between ozone and iodide as shown in equation 2.13, these are given in table 2.7. These values can be compared to the literature, which is quite sparse in terms of experimentally derived values of k. Measured and literature rates are shown in figure 2.13.

Table 2.7: Estimates for the second order rate constant between ozone and iodide under different flow conditions at 293 K. Ranges are calculated from the standard error on the gradients in figure 2.12

Flow system	$k_{O_3+I^-}$ / $\times 10^9$ M^{-1} s^{-1}
F1	2.83 ± 0.99
F10	1.79 ± 0.32
F11	4.31 ± 0.39

From figure 2.13 it can be seen that the rate constants estimated for flow systems F1, F10 and F11 are all within good agreement of the literature value at the same temperature from Magi *et al.*, Shaw and Carpenter and Rouvière *et al.*, and with a similar, although slightly smaller magnitude of error [79, 111, 120]. It is worth noting that the y axis scale on figure 2.13 is logarithmic compressing the error bars at higher values of $k_{O_3+I^-}$. The errors here are calculated from the standard error in the gradient of the lines of best fit shown in figure 2.12.

It can be seen from table 2.7 that there is a large uncertainty between the three different flow systems (as much as a factor of 2.4) that is greater than the individual uncertainties on any of the three values. The spread of values measured here ($\Delta k_{O_3+I^-} = 2.52 \times 10^9$ M^{-1} s^{-1}) is similar to the spread of values already presented in the literature at this temperature ($\Delta k_{O_3+I^-} = 1.40 \times 10^9$ M^{-1} s^{-1}) and all values appear to cluster around the measurement for the temperature dependant study from Magi *et al.*.

Using the data presented above, any of the flow conditions F1, F10 or

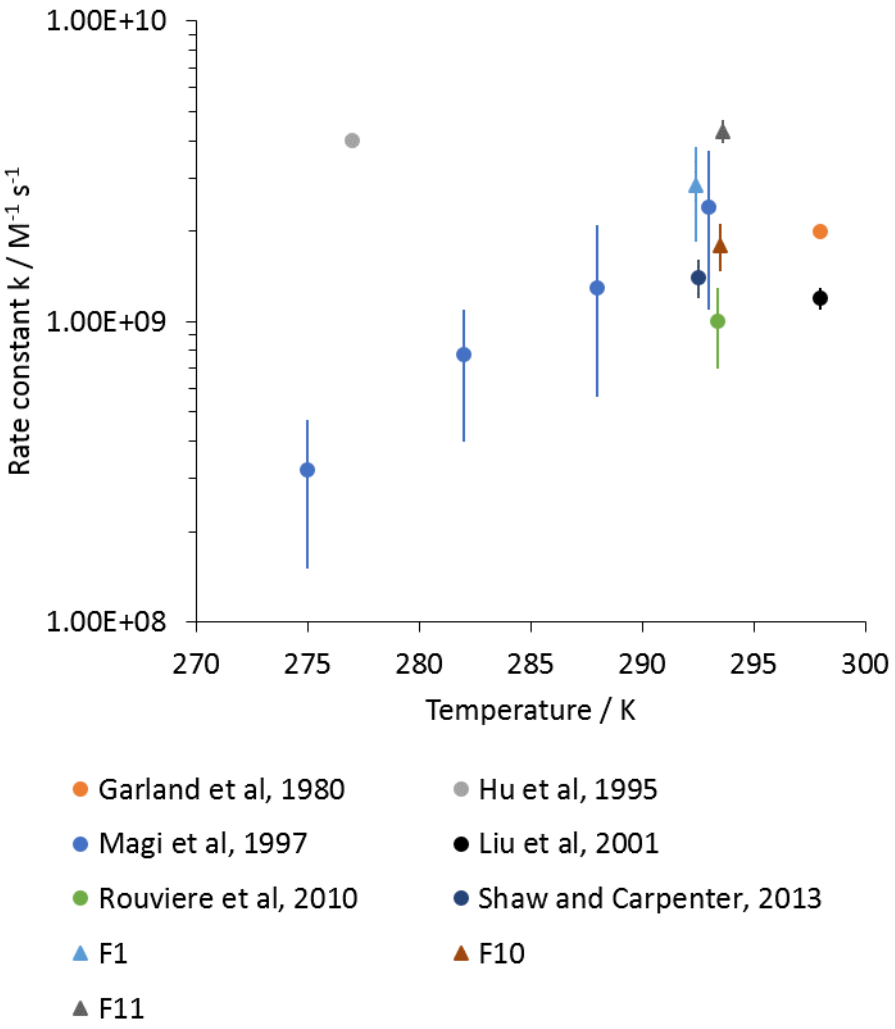

Figure 2.13: Second order rate constants for the reaction between ozone and iodide calculated for the F1, F10 and F11 flow systems in this work (triangles) compared to values from the literature (circles)

F11 appear to be suitable for use in measuring ozone deposition to aqueous surfaces. An average value for $k_{O_3+I^-}$ can be calculated from the values in table 2.7 as 2.98 ± 0.37 M^{-1} s^{-1}. Taking into account all measurements taken at 293 K from the literature, an average value for $k_{O_3+I^-}$ can be calculated as 1.94 ± 0.20 M^{-1} s^{-1}.

2.11 Conclusions

A series of optimisation experiments was run using a movable injector flow reactor to minimise the contribution of gas phase diffusion (aerodynamic resistance) to the total measured resistance. It was found that the optimal conditions were F9 flow conditions, with F10 giving comparable results.

These two sets of conditions, as well as a third flow ratio at the same total gas flow rate, were examined to directly measure the diffusion profile around the inlet in the tube. It was found that the F9 conditions gave a very high level of retro-diffusion suggesting that the gases in the reactor were not well mixed - that set of conditions was discarded. F11 flow conditions showed a high level of mixing indicating a more homogeneous gas flow after the inlet than F9 and also featured a very small amount of retro-diffusion behind the inlet. F10 gave the best results overall with a small amount of retro-diffusion, well mixed gases after the inlet and a low aerodynamic resistance.

The impact of changing ozone inlet levels on the retro-diffusion was found to be small under F10 flow conditions, with an average estimate for the limit of retro-diffusion being 47.38 ± 4.50 mm behind the inlet over the ozone range of 56 − 258 ppb. It is possible that under different sets of flow conditions the limit of retro-diffusion may vary as a function of $[O_3]$, though for all other analyses in this work it was assumed this was not the case. Whilst this value can be used for comparing flow conditions to see how well mixed the flows are, fortunately it has little impact on the analysis directly as any changes to the retro-diffusion limit would only change the intercept value of a first order log

plot when it is only the gradient used for the calculation of resistance.

The surface reaction between ozone and iodide was measured in a flow reactor under four different sets of flow conditions at 293 K. Surface resistances and second order rate constants were calculated for each set of experiments and these values were compared to those reported in the literature. The initial set of flow conditions used in the flow reactor (F2 conditions) produced data that had the poorest fit to a linear model as shown by the R^2 values reported in figure 2.12 and was discarded as an outlier. Values for $k_{O_3+I^-}$ for each of the other flow conditions (F1, F10 and F11) were calculated to be 2.83 ± 0.99, 1.79 ± 0.32 and $4.31 \pm 0.39 \times 10^9$ M^{-1} s^{-1}, respectively. These values were similar to those reported at similar temperatures by Magi *et al.* [79], Shaw and Carpenter [120] and Rouvière *et al.* [111]. These three sets of flow conditions would appear to be suitable for use in further ozone deposition experiments.

Chapter 3

Measurement of ozone deposition to saturated and unsaturated fatty acids at the air water interface

3.1 Fatty acids at the ocean surface

The sea surface microlayer (SML) acts as a boundary between the Earth's atmosphere and oceans. The composition of this interfacial layer influences the transport of material across it. The SML is a complex mixture of compounds containing both organic and inorganic material [65, 104, 155]. It has been shown that the SML is enriched with naturally occurring carbohydrates [148], proteins [3], lipids and derivatives [39, 122], polymeric particles [3, 147, 148], humics [9, 110], and carbonyls [61, 62, 94]. In addition, several classes of anthropogenic materials have been detected in the SML such as chlorinated hydrocarbon pesticides [29, 117, 149], organotin compounds from paints [84, 149], petroleum hydrocarbons [4, 149], polyaromatic hydrocarbons [4, 19, 118, 149], heavy metals [29, 149], and microplastics [124]. Gašparović *et al.* (1998) demonstrated that the largest fraction of dissolved organic material (DOM) in the SML is of sunlight promoted biogenic origin, from plankton and bacteria, whilst anthropogenic hydrocarbons contribute approximately 10% [38].

As a subset of lipids, fatty acids (FA) have been often shown to be enriched in the SML compared to the subsurface water [82, 93, 114]. Gašparović *et al.* (2007) categorised the total FA into four groups, linear saturated fatty acids (SAFA), monounsaturated fatty acids (MUFA), polyunsaturated fatty acids (PUFA) and branched saturated fatty acids (BrFA). This work showed that the magnitude of the unsaturated fraction of FA in the SML can be quite varied, contributing between 22.8 and 64.1% to the overall fatty acid concentration [39].

3.2 The reaction between ozone and unsaturated organic molecules

Ozone is known to react with unsaturated organic molecules in oxidative cleavage reactions where the carbon-carbon double bond is broken in a series of steps as proposed by R. Criegee, shown in figure 3.1 [22]. In the first step, ozone

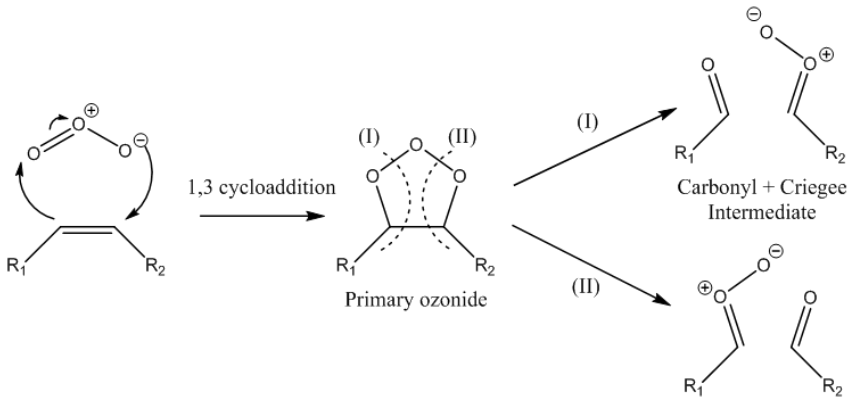

Figure 3.1: Reaction mechanism for the ozonolysis of unsaturated organic molecules showing the 1,3 cycloaddition of ozone over the double bond and the decomposition of the resulting primary ozonide

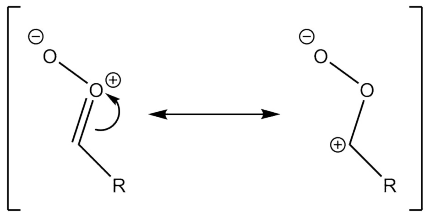

Figure 3.2: Zwitterion forms of a Criegee intermediate

and the unsaturated molecule undergo a 1,3 cycloaddition to form a primary ozonide (also called a molozonoide or a 1,2,3-trioxolane). The primary ozonide then decomposes via one of two pathways to form a carbonyl and a so-called Criegee intermediate.

The formation of this intermediate is stabilised due to the fact it is zwitterionic as shown in figure 3.2. It is sometimes possible for these products to re-combine in another 1,3-cycloaddition to form a secondary ozonide (a 1,2,4-trioxolane) or alternatively, due to the stability and therefore relatively long lifetimes of both species, the Criegee intermediate and carbonyl can be isolated or transported away from one another to undergo further reactions elsewhere. It is not uncommon therefore to observe multiple primary and secondary prod-

ucts from the ozonolysis of even simple alkenes [155].

3.3 Ozone dry deposition

The reaction of ozone with a molecule in the sea surface can be categorised as a bimolecular surface phase reaction. There area two main mechanisms for such reactions, the Langmuir-Hinshelwood (LH) and Eley-Rideal (ER) mechanisms. In the LH mechanism, two reactive species must be transported through the respective bulk phases, adsorb onto the surface layer, and then collide in the surface to react. In the case of SML ozonolysis, the first step involves an ozone molecule dissolving/adsorbing onto the surface and a reactive substrate molecule moving through the bulk solution phase to the surface. Once at the surface, the two surface-phase molecules must collide and react. These are shown in the scheme below.

$$O_{3(g)} \rightleftharpoons O_{3(surface)} \tag{3.1}$$

$$X_{(aq)} \rightleftharpoons X_{(surface)} \tag{3.2}$$

$$O_{3(surface)} + X_{(surface)} \longrightarrow Products_{(surface)} \tag{3.3}$$

Under these conditions, a steady state of adsorbed ozone will develop due to a balancing of the surface reactions and equilibrium of gas/surface ozone. If the gas phase ozone concentration increases, the steady state surface phase ozone concentration will rise as well. At a certain concentration of ozone, the oxidation rate of substrate X will no longer be limited by the concentration of ozone but by the probability of a collision between an adsorbed ozone and X molecule resulting in a successful reaction. Here, the reaction rate will be limited with increasing ozone.

The ER mechanism describes a bimolecular surface reaction where one species reacts directly from the bulk phase, i.e. a nonthermal surface reaction.

In the case of SML ozonolysis, a substrate molecule must diffuse through the bulk solution phase to the surface. Once in the surface phase, a heterogeneous reaction can occur between the substrate and a gaseous molecule of ozone. These steps are shown in the scheme below.

$$Y_{(aq)} \rightleftharpoons Y_{(surface)} \tag{3.4}$$

$$O_{3(g)} + Y_{(surface)} \longrightarrow Products_{(surface)} \tag{3.5}$$

In both these cases, as shown in equations 3.3 and 3.5, products are generated in the surface phase, where the reaction takes place. However, these products are likely to have vastly different solubilities and volatilities than the reactive substrates they were formed from and so the transport of these products into either the bulk solution phase (dissolution) or the bulk gas phase (evaporation) is possible. The exact fate of any product of surface ozonolysis will therefore depend on its individual physical properties.

3.4 Aims of the work presented in this chapter

The sea surface microlayer has been shown to contain various unsaturated fatty acid compounds that can react with ozone. The first aim of this work was to measure the deposition of ozone to synthetic seawater solutions containing fatty acids and compare the impact of the degree of unsaturation of the fatty acid molecule on that deposition.

The second aim of this work was to measure the deposition of ozone to synthetic seawater samples containing both unsaturated organic material and dissolved iodide and compare the relative contributions of these two constituent species.

3.5 Measuring ozonolysis in a flask reactor

A flask reactor was used to measure the ozone deposition onto fatty acid samples as in figure 3.3. To a three necked round bottomed flask (500 mL) was added a sample of synthetic seawater (200 mL) containing NaCl (0.5 M), NaBr (8.0×10^{-4} M) buffered with phosphate (0.12 M, pH 8.0). Compressed air was passed through moisture and hydrocarbon filters and the flow rate controlled using a mass flow controller (Aalborg, 1260 sccm). The ozone mixing ratio was set on a pen ray lamp ozone generator (UVP ltd.); ozone was directed into the flask and then into an ozone monitor (model 205B, 2B Technologies). The flow demand of the ozone monitor (1200 sccm) was controlled by a needle valve inside the flow path of the monitor, between the sample and reference cells and the gas pump. Any excess flow was allowed to pass out of a black carbon filter ensuring the lines stayed at atmospheric pressure. The ozone mixing ratio being supplied to the flask was monitored by switching the flow of gas through a bypass line directly from the generator into the monitor. The flask was held at room temperature (293 K) for all experiments.

To the synthetic seawater solutions in the flask, fatty acid (nonanoic, oleic, linoleic or linolenic acid; 20 - 130 μL) and/or iodide (final solution concentration 10^{-4} M) was added. The solution was stirred vigorously (200 rpm) for 5 minutes then more gently (50 rpm) for the remainder of the experiment. This was to allow the synthetic seawater mixture to mix thoroughly and then settle to form a discrete organic surface layer with continuous movement in the 'bulk' water beneath.

The flow reactor discussed in the previous chapter was not suitable for use in these experiments as the fatty acids would not form a homogeneous layer when the synthetic seawater solution was stirred. If the distribution of reactive material over the aqueous surface was not even, the ozone mixing ratio results obtained would not be representative of a single, consistent sample.

The uptake coefficient (γ_{eff}) was calculated from the initial ($[O_3]_i$) and final ($[O_3]_f$) ozone measurements using equation 3.6 [113]. These were converted

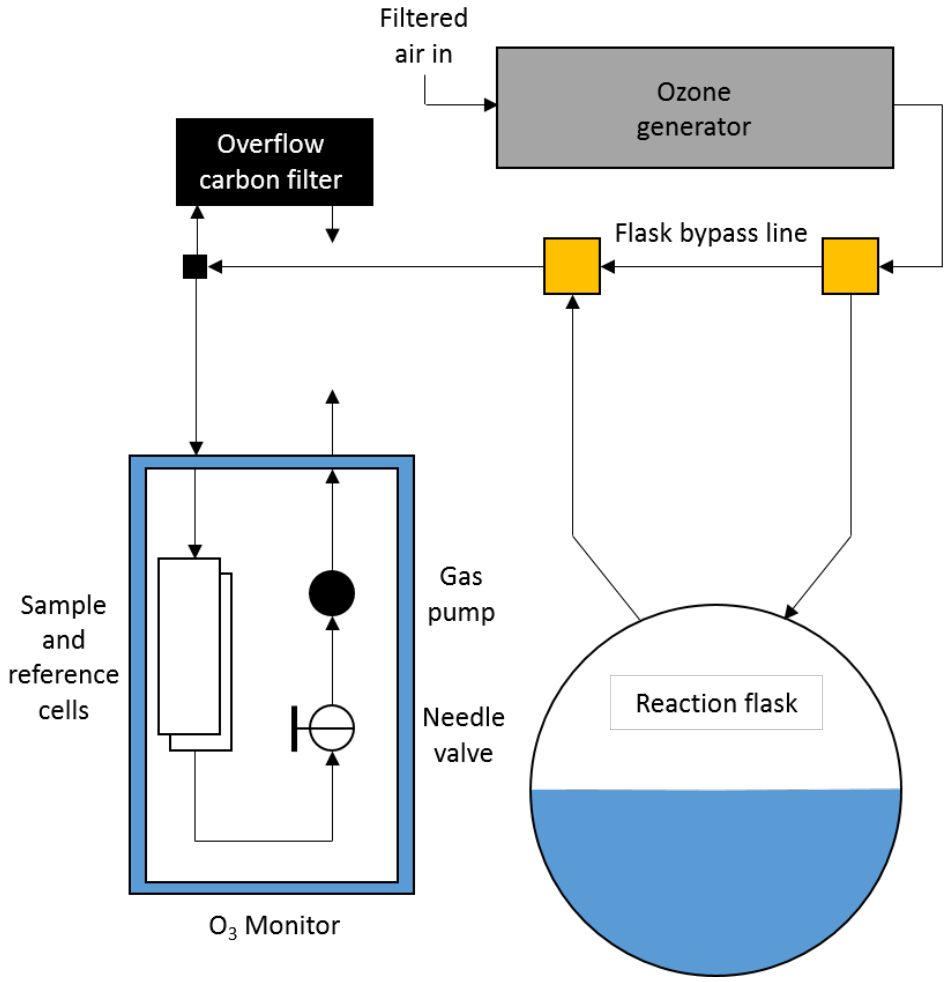

Figure 3.3: Flask reactor setup for measuring ozone deposition, the yellow squares represent switching valves and the black square represents an open t-union

into deposition velocities using equation 3.7. The surface only deposition velocity ($v_{D,s}$) or uptake coefficient ($\gamma_{eff,s}$) can be calculated using equations 3.8 and 3.9.

$$\gamma_{eff} = \frac{ln[\frac{[O_3]_i}{[O_3]_f}]}{\frac{A}{V}\frac{u_{av}}{4}t} \tag{3.6}$$

$$v_D = \frac{u_{av}}{4}\gamma_{eff} = \frac{1}{R_t} \tag{3.7}$$

$$R_t = R_a + R_s \tag{3.8}$$

$$\frac{1}{R_s} = v_{D,s} = \frac{u_{av}}{4}\gamma_{eff,s} \tag{3.9}$$

In equation 3.6, A and V refer to the surface area of the sample (74.79 cm^2) and headspace volume of the flask (300 cm^3) respectively, $u_{av}/4$ refers to the mean molecular speed of a gas phase ozone molecule ($u_{av} = 3.60 \times 10^2$ cm s^{-1} at 293 K) and t is the residence time of ozone in the flask (14.29 s) which relates to the flow rate through the headspace (1260 sccm) [113].

An ozone mixing ratio was recorded by the monitor every 2 seconds. For each exposure before and after measurement, at least 10 minutes of data were recorded (at least 300 data points). To reduce the error from the instrument noise, all data outside 2 standard deviations from the mean was discarded as noise artefact outliers (remaining number of data points = $0.95n$, where n is the original number of data points). The data was then smoothed with a 15 point square moving average for every time point (leaving $n - 14$ total data points). An example of this smoothing process is shown in figure 3.4.

It can be seen from figure 3.4 that the smoothing process gives a much cleaner signal than the raw data. The smoothing process gave an average to within 0.005% of the raw data with a much lower standard deviation (raw:

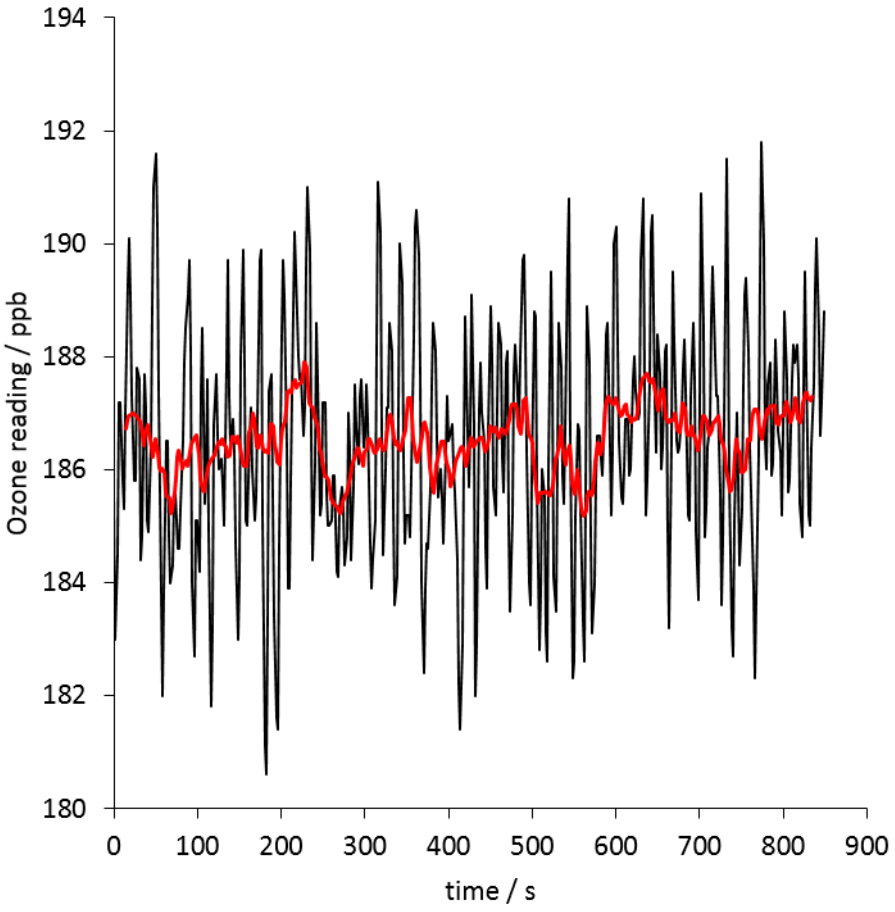

Figure 3.4: Example of the data smoothing process where the black line is the raw ozone signal from the monitor and the red line is the processed data ($n = 425$)

186.51 ± 2.06 ppb; smoothed 186.52 ± 0.55 ppb). All smoothed data points were averaged to find values for $[O_3]_i$ and $[O_3]_f$ for equation 3.6.

3.6 Flask reactor control experiments

A control experiment using MQ grade water was run in the flask over the ozone range 0 - 330 ppb, as shown in figure 3.5.

From figure 3.5 it can be seen that there is again virtually no uptake of ozone to the control sample or to the walls of the reactor to within a 98% confidence margin. In all future experiments involving the flask reactor, the losses to dissolution and the reactor walls are approximated to zero.

A second control experiment was run with the buffered synthetic seawater solution without any organic or iodide. The reaction between ozone and aqueous chloride ions occurs on a much slower timescale than that of ozone and iodide, Levenov *et al.* report a rate constant of this reaction of $k < 6 \times 10^{-3}$ M^{-1} s^{-1} [71]. Typical natural iodide concentrations occur on the order of 10^{-7} M, thus even though chloride is more concentrated than iodide by a factor of approximately 10^8, the loss of ozone to chloride will be much less significant than that to iodide as the rate is slower by a factor of approximately 10^{11}. A similar effect is expected for bromide, a reaction rate between ozone and bromide was reported as 2.48×10^2 M^{-1} s^{-1} by Liu *et al.* [77], an approximate factor of 10^6 slower than that of iodide which is not made up for by an increased concentration factor of approximately 10^3.

A control experiment was carried out with the buffered bromide and chloride salts only at the previously specified concentrations; ozone was exposed to the flask at various mixing ratios and the resulting ozone level recorded. Three repeats were carried out with three separate samples of synthetic seawater (number of mixing ratios per repeat = 8), average ozone mixing ratios are shown in figure 3.6.

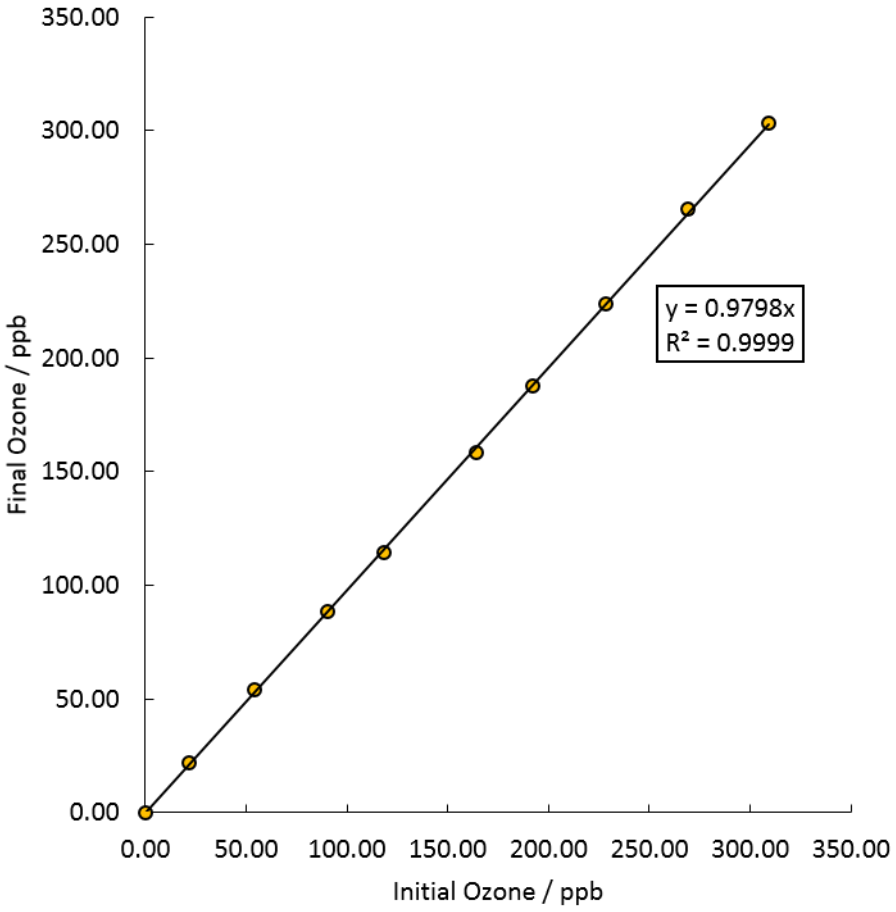

Figure 3.5: Final measured ozone levels after exposure to a control sample of MQ grade water over a range of initial supplied ozone levels

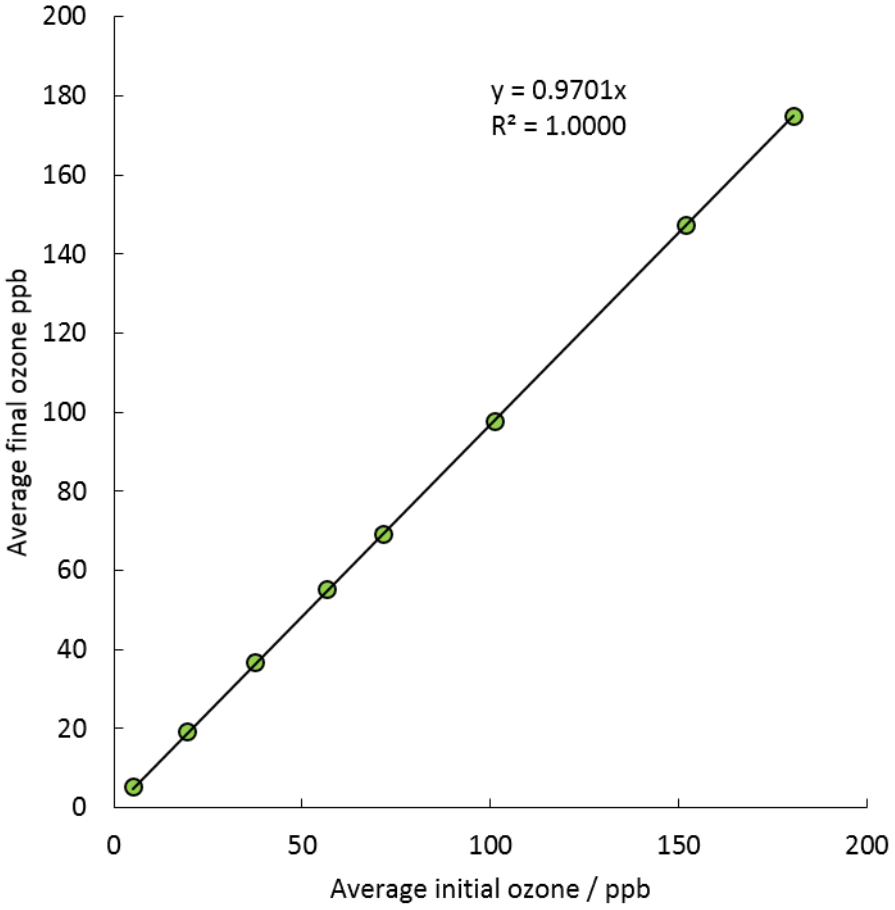

Figure 3.6: Final ozone mixing ratios recorded after exposure of buffered chloride/bromide synthetic seawater to ozone

It can be seen from figure 3.6 that there is virtually no uptake of ozone to synthetic seawater samples containing only buffered chloride and bromide, as expected. There was a high degree of reproducability between repeats as shown by the low standard deviations in the average mixing ratios presented (highest absolute standard deviation = 1.69 ppb), which are not visable on the scale of the graph.

Aerodynamic resistance was measured for a sample of high concentration iodide (0.1 M) under the conditions mentioned previously. The resistance profile at changing ozone exposure is shown in figure 3.7. The aerodynamic resistance measured was constant across the range of ozone exposure levels examined and gave an average $R_a = 1.57 \pm 0.51$ s cm^{-1} (error calculated using equation 2.23).

3.7 Ozone deposition to synthetic seawater solutions containing organic fatty acids

Unsaturated C_{18} fatty acids have previously been used as analogues of the complex natural sea surface microlayer [59, 88, 131, 151, 152]. These fatty acids have relatively low solubilities in water, low melting points and high boiling points so they remain in a distinct, liquid layer on top of an aqueous surface. The exact composition and morphology of the organic surface layer, even in these simple cases with few compounds in the synthetic seawater mixture, is difficult to predict. However, it is expected that the molecules will behave as surfactants, roughly orienting themselves with the acid group facing down towards the bulk water and the organic tails facing up towards the bulk atmosphere.

Three such molecules were selected for comparison here, representing the mono-, di- and tri-unsaturated C_{18} straight chain fatty acids, oleic, linoleic and linolenic acid, figure 3.8.

In addition to the three molecules described above, a saturated organic

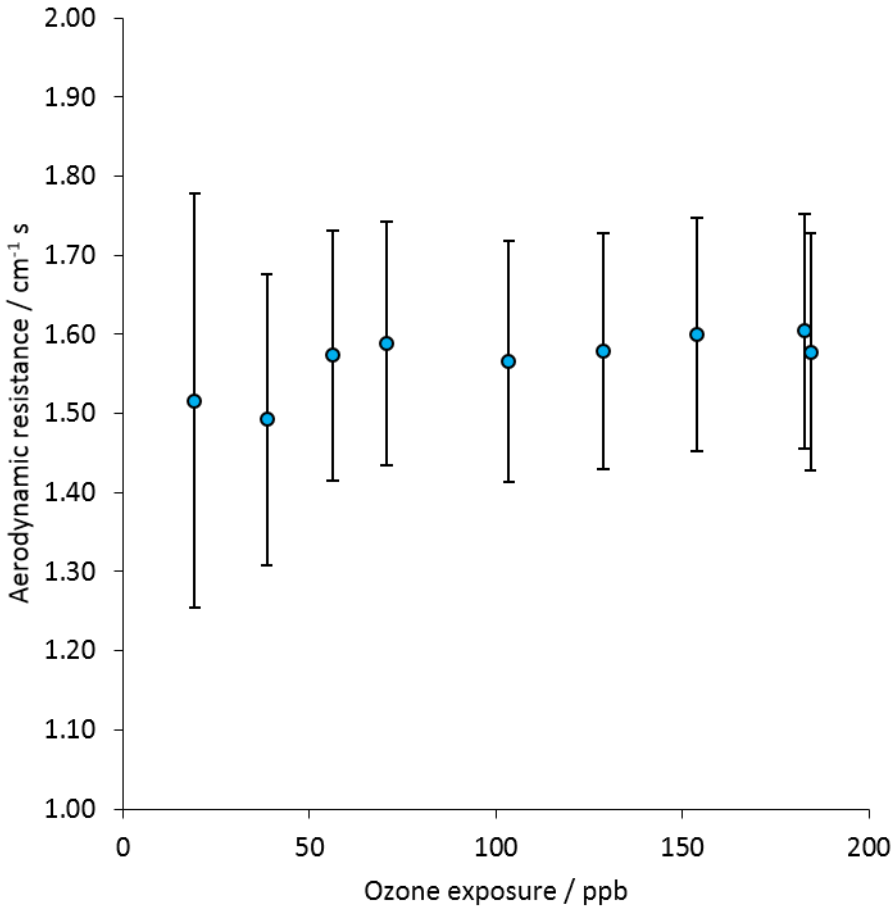

Figure 3.7: Aerodynamic resistance for the flask reactor. Error bars are calculated from the uncertainty in each average initial and final ozone measurement using equation 2.23

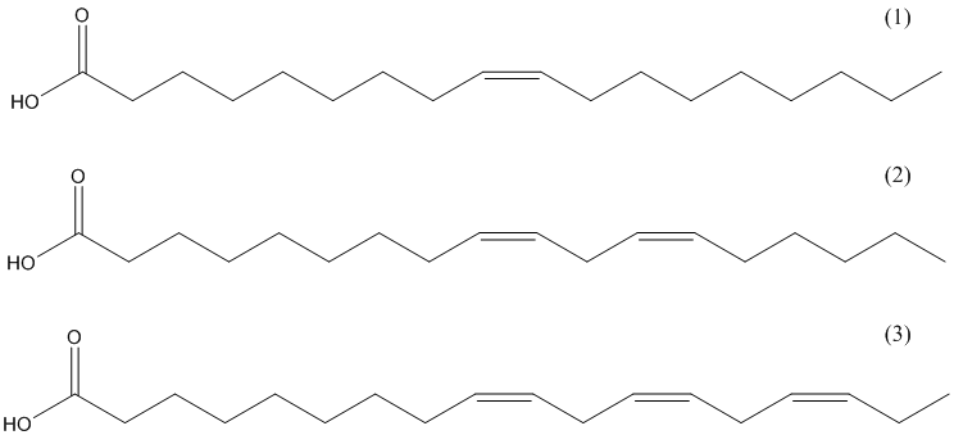

Figure 3.8: Structures of oleic acid (1), linoleic acid (2) and linolenic acid (3)

molecule, assumed to be unreactive towards ozone, was analysed for comparison. The saturated C_{18} straight chain fatty acid, stearic acid, was not suitable for these experiments as it was not liquid at room temperature. A replacement compound was selected based on the criteria that it must have a low melting point (lower than room temperature) and must not be soluble in water. This was made more difficult by the fact that as the molecular weight decreases, the solubility increases and melting point decreases. Nonanoic acid was selected as the saturated organic molecule for these experiments. It was expected that this compound would be essentially unreactive towards ozone as it has previously been shown that some higher carbon number saturated organic acids (C_{10} - C_{18}) were unreactive to ozone [108].

To test whether the nonanoic acid would dissolve rather than form a surface layer, three different sized additions were made to the buffered bromide/chloride synthetic seawater, 20, 85 and 135 μL. The surface only uptake coefficients (that is, the uptake coefficients with aerodynamic resistance taken into account) of these three additions are shown in figure 3.9.

The ozone uptake shown in figure 3.9 shows an unexpectedly high level of deposition of ozone to nonanoic acid that appears to fit the Langmuir-Hinshelwood model of a surface reaction. Chiu *et al.* demonstrated that saturated fatty acid (including nonanoic acid) surfaces can react with ozone in the presence of UV light by measuring the mixing ratio of glyoxal, an ozonolysis product, over an exposed organic surface [17]. An exposure of approximately 500 ppb ozone to a nonanoic acid surface gave glyoxal mixing ratios of almost 200 ppt but only under direct UV irradiation. This is attributed to the conversion from the saturated molecule nonanoic acid to the unsaturated 2-nonenal under UV light. In this work, the flask reactor was not exposed to any UV source other than the ambient light of the lab which may include a small amount of sunlight. It is unlikely then that this reaction pathway is the source of the measured deposition.

As this behaviour in this case cannot be attributed to reactivity, it must instead be attributed to other methods of deposition such as dissolution. It has

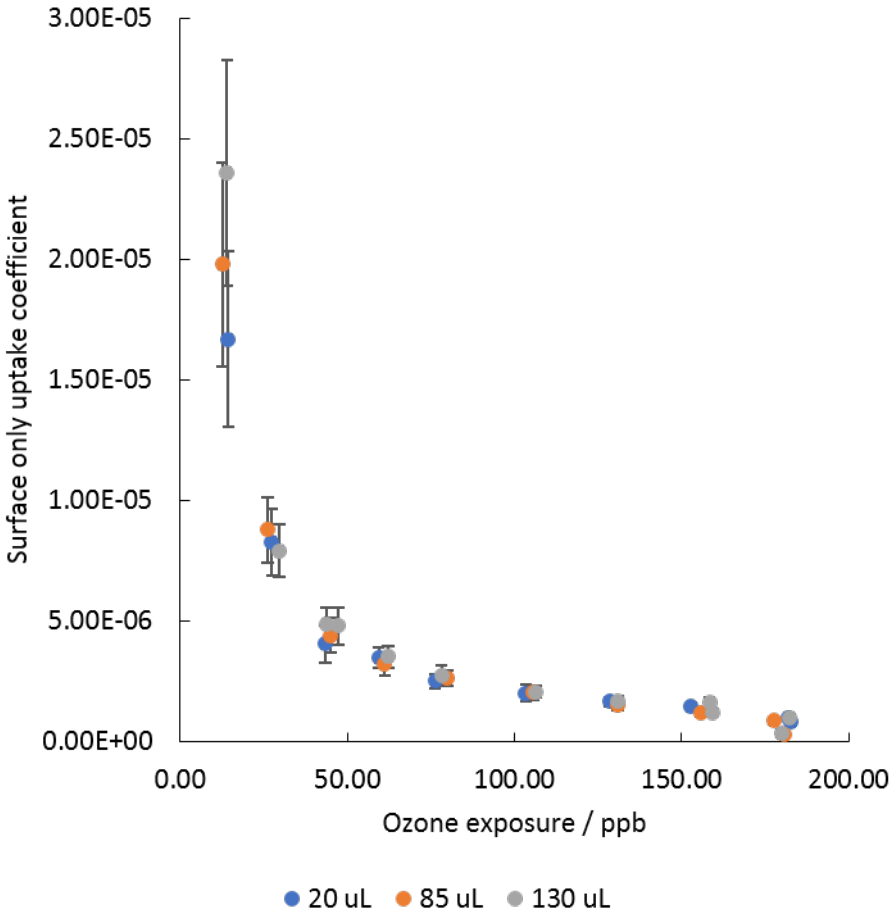

Figure 3.9: Surface only ozone uptake coefficient at changing ozone exposure levels for three additions of nonanoic acid to the buffered bromide/chloride synthetic seawater. Error bars are calculated from the uncertainty in each average initial and final ozone measurement using equation 2.23

been established that ozone is far more soluble in organic solvents than in water [7] (and references therein) which could account for the increased deposition. For all of the organic liquids referred to by Biń (2006), the dimensionless Henry's Law constant had values less than one indicating a preference for the solution phase rather than the gas phase (for example, for acetone and hexane $H = 0.711$ and 0.811, respectively). For comparison, the dimensionless Henry's Law constant for ozone in water is 3.9 at 293 K [64].

At ozone exposure levels above 20 *ppb*, the three different additions of nonanoic acid give identical values for the surface only uptake coefficient, suggesting that under each set of conditions a similar surface layer is being presented to the ozone. At very low ozone exposure levels (< 20 *ppb*) the three uptake coefficients for each of the additions are more widely spread, with a lower volume of addition corresponding to a lower measured uptake coefficient, though the error bars for these measurements overlap in such a way as to make it impossible to infer a difference between the three additions.

The first of the unsaturated molecules tested was oleic acid, surface only ozone uptake coefficient profiles are shown for three repeat additions of 20 μL in figure 3.10.

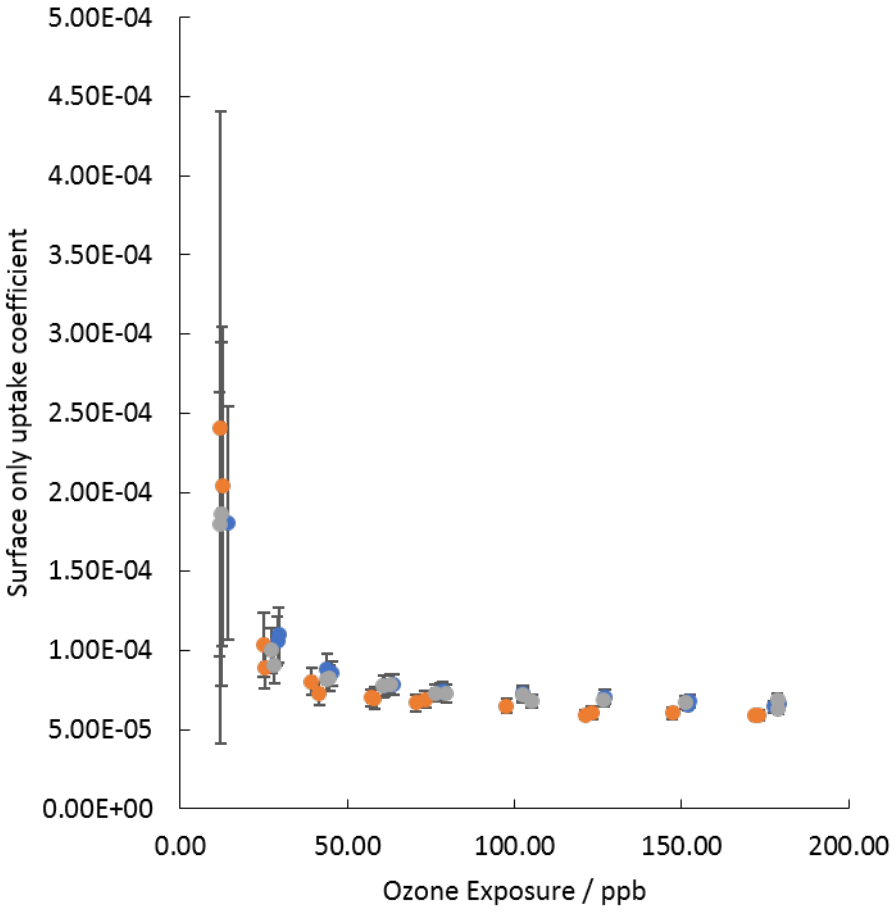

Figure 3.10: Surface only ozone uptake coefficient at changing ozone exposure levels for three repeat additions of 20 μL oleic acid to the buffered bromide/chloride synthetic seawater. Error bars are calculated from the uncertainty in each average initial and final ozone measurement using equation 2.23

Table 3.1: Ozone uptake coefficients onto saturated fatty acids (group 1), unsaturated fatty acids (group 2), oleic acid and derivatives (group 3), linoleic acid (group 4), linolenic acid (group 5) and fatty acid mixtures (group 6) from the literature and this work. N/a denotes values that were not available in the referenced work

Compound	Group	γ_{eff}	γ_{eff} error	Ozone mixing ratio	T / K	Sample morphology	Ref.
Nonanoic acid	1	4.53E-06	3.83E-07	45 ppb	293	3.46 μm liquid film on salt water	This work
hexadecane	1	2.00E-05	6.00E-06	4.06 ppb	298	Rotating wall flow reactor - liquid sample	[91]
Tridecane	1	3.00E-05	1.20E-05	25 ppb	268	Wetted wall 0.57 mm liquid layer	[24]
Octenyl-trichlorosilane	2	1.30E-04	1.00E-05	4.06 ppb	245	Organised Organic Thin Film	[91]
1-octadecene	2	2.40E-04	4.00E-04	100 ppm	N/a	800 nm aerosol particle	[49]

Compound	Group	γ_{eff}	γ_{eff} error	Ozone mixing ratio	T / K	Sample morphology	Ref.
1-hexadecene	2	3.80E-04	6.00E-05	4.06 ppb	298	Rotating wall flow reactor - liquid sample	[91]
1-tridecene	2	7.50E-04	5.00E-05	25 ppb	263	Wetted wall 0.57 mm liquid layer	[24]
1-octene	2	1.30E-03	1.00E-04	4.06 ppb	243	Rotating wall flow reactor - liquid sample	[91]
Oleic Acid	3	2.60E-07	1.00E-08	8 ppm	296	liquid layer on pendant drop	[41]
Oleic Acid	3	3.00E-06	N/a	20 ppm	296	Langmuir trough monolayer on pure water	[139]
Oleic Acid	3	4.00E-06	N/a	170-487 ppb	293	langmuir trough 2 nm layer on salt water	[107]

Compound	Group	γ_{eff}	γ_{eff} error	Ozone mixing ratio	T / K	Sample morphology	Ref.
Oleic Acid	3	4.70E-06	1.80E-06	77-690 ppb	295	langmuir trough liquid layer on pure water	[63]
Oleic Acid	3	5.20E-05	1.00E-06	4.06 ppb	271	Rotating wall flow reactor - solid sample	[92]
Oleic Acid	3	8.18E-05	5.17E-06	43 ppb	293	2.67 μm liquid film on salt water	This work
Oleic Acid	3	3.40E-04	3.00E-05	24 ppmv	290	2 μm liquid drop	[100]
Oleic Acid	3	5.50E-04	5.00E-05	0.45 ppm	273	10 μm particles on Ge crystal (solid)	[54]
Oleic Acid	3	7.50E-04	1.20E-04	100 ppm	N/a	800 nm aerosol particle	[49]
Oleyl alcohol	3	7.50E-04	1.30E-04	100 ppm	N/a	800 nm aerosol particle	[49]

Compound	Group	γ_{eff}	γ_{eff} error	Ozone mixing ratio	T / K	Sample morphology	Ref.
Oleic Acid	3	8.00E-04	1.00E-04	N/a	298	Coated wall 0.6 mm film	[131]
Oleic Acid	3	8.30E-04	2.00E-05	4.06 ppb	288.5	Rotating wall flow reactor - liquid sample	[92]
Oleic Acid	3	8.80E-04	5.00E-05	10-100 ppm	298	800 nm aerosol particle	[48]
Oleic Acid	3	9.90E-04	9.00E-05	100 ppm	298	2.45 μm aerosol particle	[123]
Oleic Acid	3	1.10E-03	1.40E-04	0.45 ppm	277	10 μm particles on Ge crystal (solid)	[54]
Methyl Oleate	3	1.23E-03	1.00E-04	10-100 ppm	298	800 nm aerosol particle	[48]
Oleic Acid	3	1.50E-03	1.00E-04	25-1100 ppb	295	150nm aerosol particles	[88]

Compound	Group	γ_{eff}	γ_{eff} error	Ozone mixing ratio	T / K	Sample morphology	Ref.
Oleic Acid	3	2.12E-03	2.80E-04	0.45 ppm	290	10 μm particles on Ge crystal (liquid)	[54]
Oleic Acid	3	2.17E-03	4.20E-04	0.45 ppm	282	10 μm particles on Ge crystal (liquid)	[54]
Oleic Acid	3	2.23E-03	1.40E-04	0.45 ppm	282	10 μm particles on Ge crystal (solid)	[54]
Oleic Acid	3	3.43E-03	1.14E-03	0.45 ppm	298	10 μm particles on Ge crystal (liquid)	[54]
Oleic Acid	3	7.30E-03	1.50E-03	100 ppm	298	680 nm aerosol particle	[123]
Linoleic Acid	4	1.40E-04	1.00E-05	4.06 ppb	259.5	Rotating wall flow reactor - solid sample	[92]
Linoleic Acid	4	1.62E-04	1.87E-05	43 ppb	293	2.62 μm liquid film on salt water	This work

Compound	Group	γ_{eff}	γ_{eff} error	Ozone mixing ratio	T / K	Sample morphology	Ref.
Linoleic Acid	4	3.50E-04	2.00E-05	N/a	298	0.2 μm liquid film on solid surface	[152]
Linoleic Acid	4	1.10E-03	2.00E-04	100 ppm	N/a	800 nm aerosol particle	[49]
Linoleic Acid	4	1.20E-03	2.00E-04	4.06 ppb	269.5	Rotating wall flow reactor - liquid sample	[92]
Linoleic Acid	4	1.30E-03	1.00E-04	N/a	298	Coated wall 0.6 mm film	[131]
Linolenic Acid	5	2.26E-04	1.75E-05	44 ppb	293	2.67 μm liquid film on salt water	This work
Linolenic Acid	5	1.80E-03	2.00E-04	N/a	298	Coated wall 0.6 mm film	[131]
Oleic Acid / Myristic acid mix	6	9.70E-05	1.00E-05	24 ppmv	290	2 μm liquid drop	[100]

Compound	Group	γ_{eff}	γ_{eff} error	Ozone mixing ratio	T / K	Sample morphology	Ref.
Canola oil	6	8.00E-04	5.00E-05	25 ppb	298	Wetted wall 0.57 mm liquid layer	[24]
10% Oleic Acid / Stearic Acid	6	1.53E-04	1.87E-04	1-50 ppm	298	0.2-0.5 μm liquid drop	[58]
30% Oleic Acid / Stearic Acid	6	2.05E-04	1.85E-04	1-50 ppm	298	0.2-0.5 μm liquid drop	[58]
50% Oleic Acid / Stearic Acid	6	1.54E-04	1.84E-04	1-50 ppm	298	0.2-0.5 μm liquid drop	[58]
60% Oleic Acid / Stearic Acid	6	5.93E-04	1.84E-04	1-50 ppm	298	0.2-0.5 μm liquid drop	[58]
75% Oleic Acid / Stearic Acid	6	8.38E-04	2.56E-04	1-50 ppm	298	0.2-0.5 μm liquid drop	[58]
90% Oleic Acid / Stearic Acid	6	1.11E-03	2.57E-04	1-50 ppm	298	0.2-0.5 μm liquid drop	[58]
100% Oleic Acid / Stearic Acid	6	1.25E-03	2.00E-04	1-50 ppm	298	0.2-0.5 μm liquid drop	[58]

The deposition shown in figure 3.10, with values of surface uptake coefficient, $\gamma_s = 0.6 - 2.4 \times 10^{-4}$, falls well within the range of values reported in the literature (table 3.1, group 3). Literature values for ozone uptake coefficient onto oleic acid are very broad, with a range of $2.60 \times 10^{-7} - 7.3 \times 10^{-3}$. The uptake coefficient is controlled primarily by the structure of the sample compound, with saturated molecules giving much lower values of uptake coefficient than unsaturated compounds (e.g. 25 times increase in γ_{eff} from tridecane to 1-tridecene [24] and 19 times increase in γ_{eff} from hexadecane to 1-hexadecene [91]). For samples containing mixtures of saturated and unsaturated compounds, increasing the mole fraction of the saturated compounds decreases the observed uptake coefficient [58, 100].

Sample state is also very important to ozone deposition, with samples in the solid state giving lower uptake coefficients than the corresponding liquids (e.g. 16 times increase in γ_{eff} from solid to liquid oleic acid and 8.6 times increase in γ_{eff} from solid to liquid linoleic acid [92]). It has also been shown that for mixed compound samples, once the mole fraction of a high melting point compound is sufficiently high, the overall sample becomes more crystalline and the measured γ_{eff} stabilises at a low value [58]. While the physical state of a sample was shown to strongly impact uptake coefficient, sample temperature showed much less of a dependence [92], though a temperature effect has been observed for samples in the solid phase [54].

It has also been shown that the morphology of samples in the same state and at the same temperature can heavily impact ozone uptake. Hearn *et al.* observed that for similarly sized particles of oleic acid an methyl oleate, the acid gave a lower uptake coefficient which was attributed to increased rigidity in the surface structure due to hydrogen bonds [48]. Moise and Rudich compared two similar compounds, one able to exist as a free liquid (1-octene) and another bound onto a silicate backbone as an Organised Organic Thin Film (OOTF) to force the regular alignment of the hydrophobic chains (octenyltrichlorosilane). It was observed that the compounds bound in the OOTF gave lower values of uptake coefficient than the free counterparts ($\gamma_{eff} = 0.13 \pm 0.01$ - 1.3 ± 0.1

$\times 10^{-3}$) [91]. In this case, the OOTF was said to only offer surface reactions, whereas the free liquids gave higher uptake due to the additional dissolution and bulk reactions.

In general, it can be seen from table 3.1 that samples comprised of solely a pure liquid fatty acid give higher values of uptake coefficient than fatty acids on an aqueous surface. Very low depositions were observed by Kleber *et al.* ($4.7 \pm 1.8 \times 10^{-6}$ [63], González-Labrada *et al.* ($2.6 \pm 0.1 \times 10^{-6}$ [41]), Rennie *et al.* (4×10^{-6} [107]) and Voss *et al.* (3×10^{-6} [139]). In these works, the very low values of uptake coefficient were attributed to deposition proceeding via surface reactions only, and not dissolution or bulk reactions as the samples were prepared as monolayers.

The magnitude of the deposition observed in figure 3.10 suggests that in this case, the oleic acid is acting more like a pure organic film than a true monolayer. At 298 K, oleic acid has a density of 0.895 g ml^{-1} [102] and a solubility in water of approximately 1.15×10^{-2} mg L^{-1} [1]. It can be calculated that for the additions described, approximately 2.60 μg of the oleic acid dissolves leaving a layer approximately 2.67 μm thick on the surface of the synthetic seawater. This is much greater than the sample depth calculated by Rennie *et al.* for an oleic acid monolayer of 2 nm [107].

The deposition curve shown in figure 3.10 shows that with increasing ozone exposure levels there is a decrease in the uptake coefficient, which suggests that the Langmuir-Hinshelwood surface reaction is controlling the uptake. The uptake is clearly reactive as the uptake coefficient is much higher than that measured on the unreactive nonanoic acid surface in figure 3.9.

Good agreement is seen between the three repeats, with little deviation observed from the average at each exposure level apart from at the lowest exposures where once again the high error bars suggest there are no meaningful inferences to be made about any lack of reproducibility. The high error observed at low ozone exposure levels was primarily caused by the instrumental noise being a significant proportion of the signal when the absolute ozone

readings are low.

Deposition profiles for three repeat additions of linoleic acid are shown in figure 3.11 and a deposition profile for one repeat addition of linolenic acid is shown in figure 3.12.

The deposition shown in figures 3.11 and 3.12 also shows the Langmuir-Hinshelwood surface reaction profile, again with good agreement between repeats for linoleic acid, other than at low ozone. Due to time constraints, only one repeat was carried out for linolenic acid, though the results should still be comparable as all previous repeats have been very consistent. The uptake coefficients measured for the polyunsaturated linolenic and linoleic acids appear to be higher than those measured for the monounsaturated oleic acid in figure 3.10, with the greatest amount of uptake observed for linolenic acid.

Figure 3.13 shows the surface only ozone uptake coefficient at changing ozone exposure levels for all four fatty acids examined with all error bars removed for clarity.

It can be seen from figure 3.13 that as the degree of unsaturation of a molecule increases, the reactivity towards ozone also increases due to the increased number of available reactive sites in the sample. A similar effect was observed by Thornberry and Abbatt (2004) [131] where the uptake coefficients for oleic, linoleic and linolenic acids were found to be 0.8 ± 0.1, 1.3 ± 0.1 and $1.8 \pm 0.2 \times 10^{-3}$, respectively. All the fatty acids exhibit similar profiles, with a peak at low ozone quickly plateauing off to a lower uptake as ozone exposure increases. In most cases, there is little change in the ozone uptake coefficient above 60-70 ppb ozone exposure.

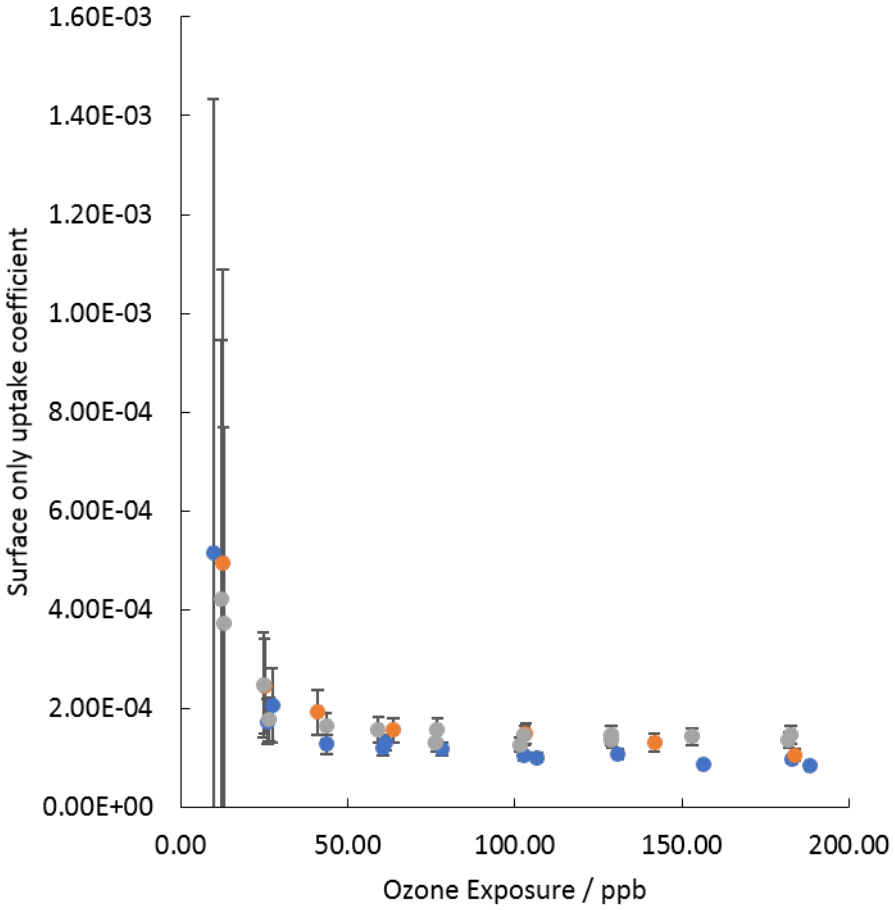

Figure 3.11: Surface only ozone uptake coefficient at changing ozone exposure levels for three repeat additions of linoleic acid to the buffered bromide/chloride synthetic seawater. Colours show different repeats. Error bars are calculated from the uncertainty in each average initial and final ozone measurement using equation 2.23

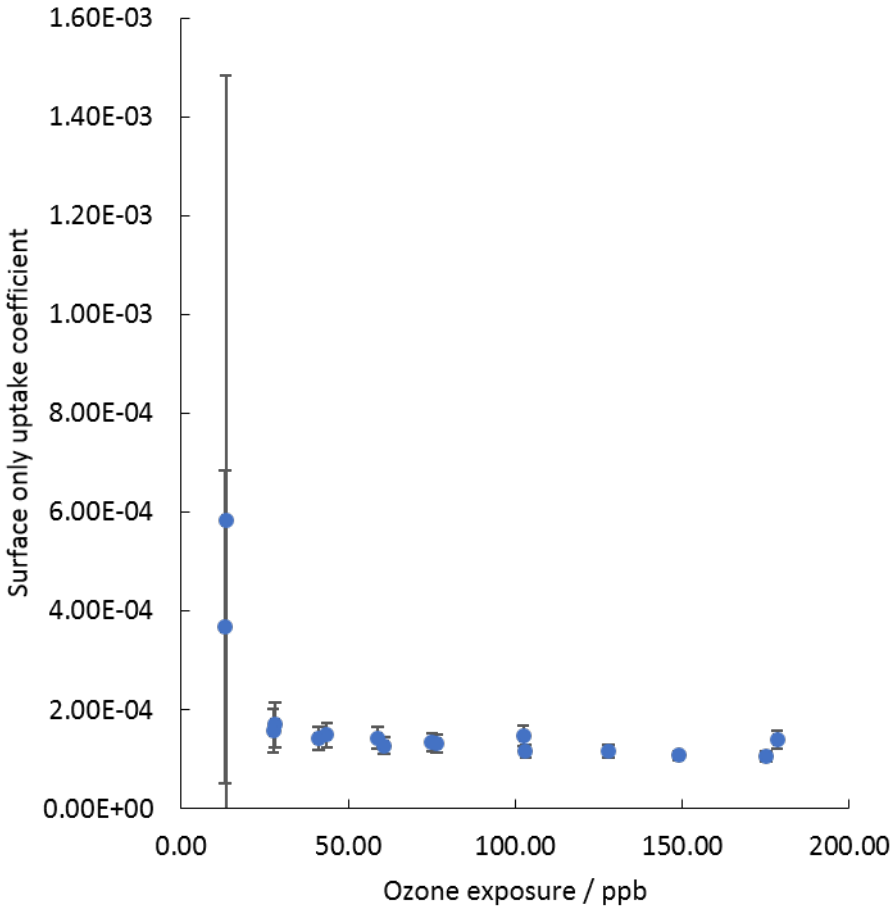

Figure 3.12: Surface only ozone uptake coefficient at changing ozone exposure levels for one addition of linolenic acid to the buffered bromide/chloride synthetic seawater. Error bars are calculated from the uncertainty in each average initial and final ozone measurement using equation 2.23

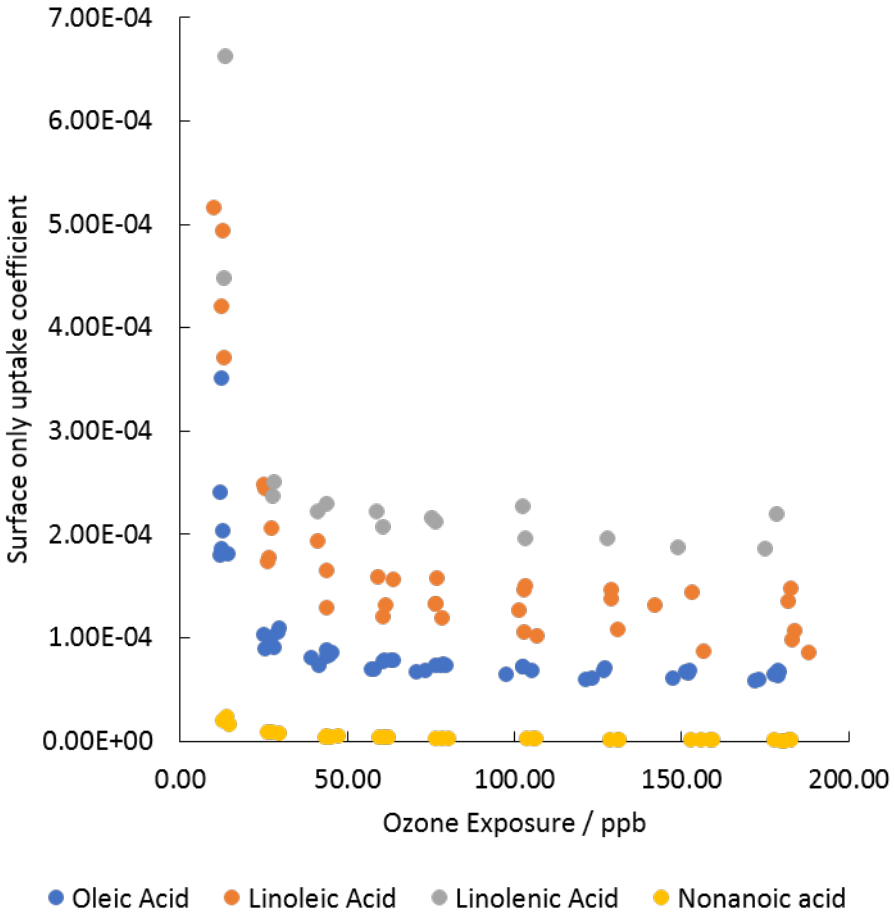

Figure 3.13: Surface only ozone uptake coefficient at changing ozone exposure levels for oleic (blue), linoleic (orange), linolenic (grey) and nonanoic (yellow) acids, error bars removed for clarity

3.8 Ozone deposition to synthetic seawater solutions containing mixtures of organic material and halide salts

As mentioned in chapter 1, Martino *et al.* measured ozone deposition onto samples of DOM, iodide and a mixture of both [81]. It was found that for concentrations of DOM and I^- that gave similar depositions that the mixture of both gave a higher total deposition but lower than the direct sum. A similar effect was observed by Shaw and Carpenter where the addition of DOM to solutions of iodide exposed to ozone reduced the emission of I_2 with similar observed ozone loss for both systems [120].

To compare the deposition of ozone onto aqueous iodide and organic surfaces, a comparison was made between iodide ([NaI] = 1.5×10^{-4} M) and oleic acid (20 μL addition). A high concentration of iodide was selected so that the deposition would be of a similar scale to that of oleic acid to facilitate a direct comparison between the uptake due to iodide and the uptake due to organics. The uptake onto a solution of iodide at 1.5×10^{-4} M is shown in figure 3.14. From this figure, an average surface resistance for iodide can be calculated using the method described previously in chapter 2, section 2.2 (equation 2.13; $R_s = 2.71 \pm 0.18$ cm^{-1} s [35].

To calculate a theoretical ozone uptake due to the bulk reaction with iodide and surface reaction with organics, equation 3.10 can be used from Clifford *et al.* [21].

$$\gamma_{obs} = \gamma_{bulk} + \gamma_{surf} \tag{3.10}$$

An expression for γ_{bulk} can be constructed (equation 3.11) by combining the expression for resistance (equation 2.13) with the expression for surface deposition and resistance (equation 3.9). This new equation is independent of ozone concentration and thus γ_{bulk} can be estimated as 5.18×10^{-5}.

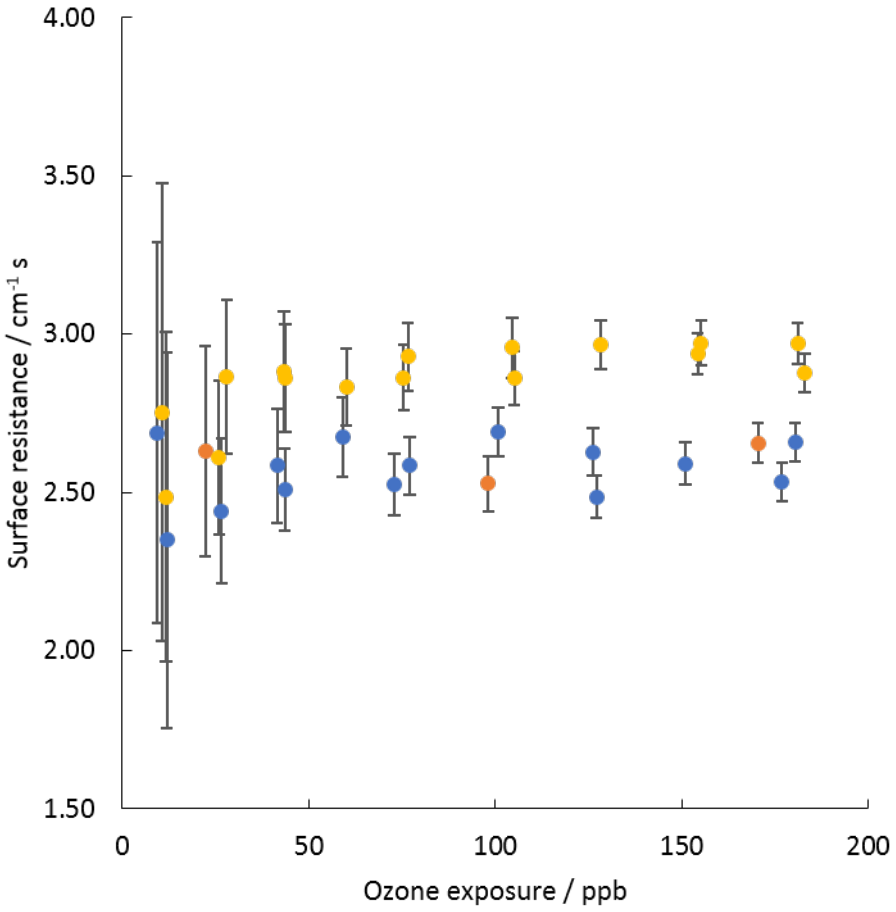

Figure 3.14: Surface resistances measured for three repeats of iodide (1.5×10^{-4} M) in the flask reactor. Error bars are calculated from the uncertainty in each average initial and final ozone measurement using equation 2.23, different colours represent different repeats

$$\gamma_{bulk} = \frac{4\sqrt{k[\mathrm{I}^-]D}}{Hred} u_{av} \tag{3.11}$$

An estimate of γ_{surf} is given by the Langmuir - Hinshelwood fit (equation 3.12), from Mmereki and Donaldson [90].

$$\gamma_{surf} = \frac{4A[\mathrm{O}_3]}{(\sigma\omega\mathrm{O}_3)(B + \mathrm{O}_3)} \tag{3.12}$$

In equation 3.12, the coefficient A is equal to the product of the second order rate constant and the number of surface sites available to ozone, B is the ratio of desorption/adsorption rate constants from the bulk gas to bulk solution phases, σ is the collision cross section of the surface molecule and ω is the mean thermal velocity of ozone.

Mmereki and Donaldson estimate the collision cross section of a molecule of anthracene to be equal to its face area [90]. This was because it is an unsaturated, fully aromatic molecule and its full face area represents a target for a reaction with an ozone molecule. Oleic acid has only one reactive site for ozonolysis, the unsaturated carbon-carbon bond. Here, it was estimated that the collision cross section for the C=C bond was equal to a proportion of the surface area of a cylinder wrapped around the double bond as shown in figure 3.15.

The height of the cylinder, h, was approximated as 1.5× the length of the bond ($h = 2.00 \times 10^{-10}$ m). The radius of the cylinder, r, was approximated as the distance perpendicular to h between the sp^2 and sp3 hybridised carbon atoms ($r = 1.33 \times 10^{-10}$ m). Ozone can only attack the double bond from the front or rear, and only one of those will present itself at the surface at once. Thus the collision cross section was estimated as one quarter of the total surface area of the body of the cylinder ($\sigma = 6.69 \times 10^{-15}$ cm^2 molec^{-1}).

Values of A and B were solved for oleic acid through trial and error using the Goal Seek function in Microsoft Excel. The values from Mmereki and Donaldson were selected as starting points ($A = 2.55 \times 10^{-3}$ s^{-1}, $B = 2.14 \times$

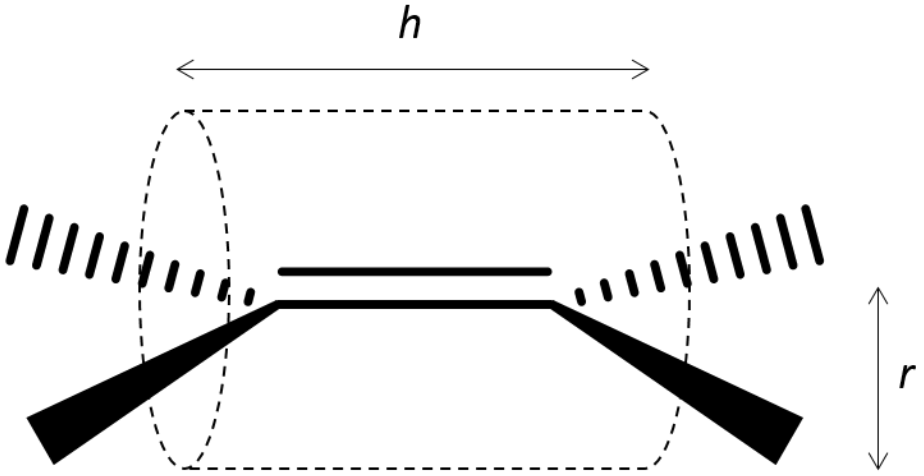

Figure 3.15: Collision cross section of a carbon-carbon double bond

10^{14} molec cm^{-3} [90]) then Goal Seek was employed iteratively to increase the R^2 value compared to the average uptake coefficient measurements for oleic acid (all oleic acid measurements in figure 3.10, averages shown in blue circles in figure 3.16). The final fit is shown in figure 3.16. The final values for A was found to be 2.36 $\times$ 10^{-3} s^{-1} and the final value for B was found to be 4.23 $\times$ 10^{11} molec cm^{-3}. The fit gave an R^2 value of 0.795.

It can be seen that the fit in figure 3.16 does not match the measured data well as the gradient of the curve is more shallow than the data. This is also evident in the R^2 value being lower than those given by Mmereki and Donaldson (0.898 and 0.981 for water/anthracene and water/anthracene/octanol mixtures, respectively) [90]. This could suggest that the Langmuir - Hinshelwood surface mechanism does not fully describe the mechanism of ozone loss being observed onto oleic acid in this case.

The value of A estimated here for oleic acid (A_{oleic} = 2.36 $\times$ 10^{-3} s^{-1}) is very similar to that estimated by Mmereki and Donaldson for the reaction of ozone onto anthracene on water surfaces ($A_{anthracene}$ = 2.55 $\times$ 10^{-3} s^{-1}) [90]. As mentioned previously, this coefficient depends on the rate constant and number of active surface sites, the latter of which is difficult to measure. The experiments carried out in the referenced work used 100 mL of reactive solution in a 250 mL flask. Assuming the flask is spherical this gives a surface

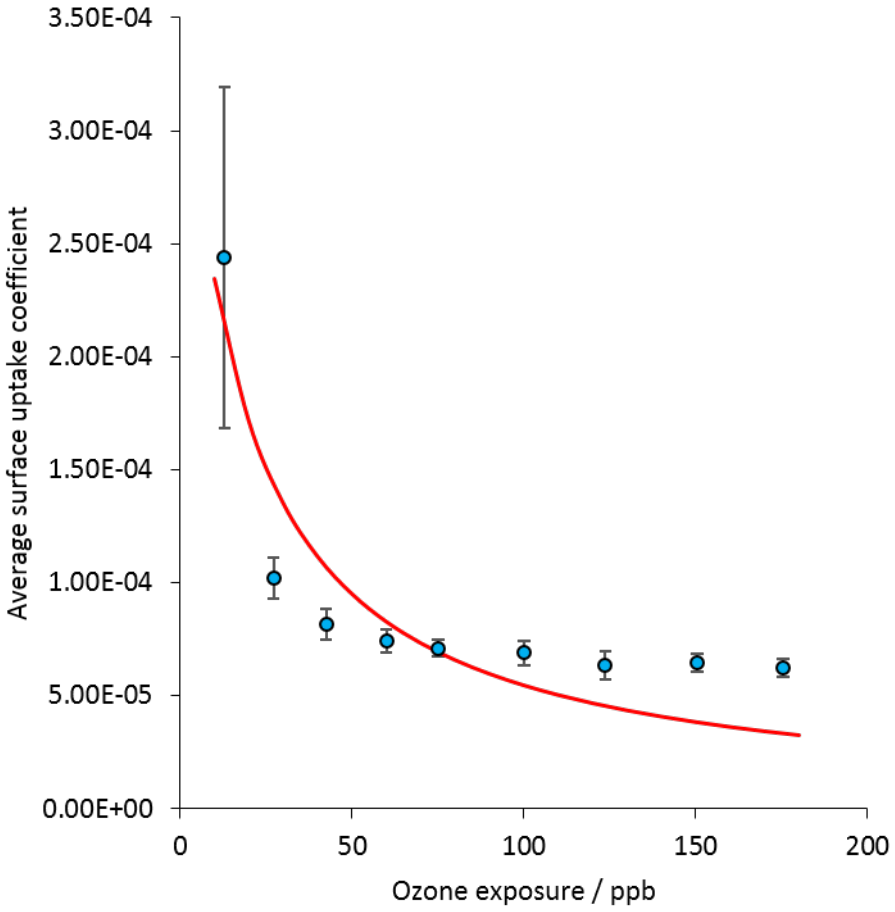

Figure 3.16: Langmuir - Hinshelwood fit (red line) to average oleic acid ozone uptake coefficients (blue circles). Error bars are calculated from the uncertainty in each uptake coefficient measurement using equation 2.23

area of 47.1 cm^2, approximately 1.6 times less than the surface area for the flask experiments in this work (200 mL sample in 500 mL flask, area = 74.8 cm^2). Assuming a similar density of surface sites this would suggest that the rate constant for the reaction of ozone with oleic acid is lower than that of anthracene by a similar factor. This gives an approximation for the second order surface reaction coefficient for oleic acid and ozone of 1.64×10^{-17} cm^2 $molec^{-1}$ s^{-1}.

The coefficient B represents the ratio of desorption to adsorption rate constants and as such a higher value suggests a surface onto which ozone is less readily adsorbed. Mmereki and Donaldson found that for the reaction of ozone and anthracene, the addition of the surface active species octanol increased surface adsorption as shown by a reduction in the value of B by a factor of approximately 4 (5.08×10^{14}, 21.43×10^{14} molec cm^{-3} for solutions with and without octanol, respectively) [90]. The value of B obtained here is several orders of magnitude lower than those reported in the referenced work (4.23×10^{11} molec cm^{-3}) which would suggest that the rate of ozone adsorption is much more favourable onto this oleic acid surface than those measured in the referenced work.

A synthetic seawater solution was prepared with oleic acid (20 μL) and NaI (1.5×10^{-4} M) and the deposition monitored, figure 3.17. Also shown in this figure are the average uptake coefficients observed in the oleic only experiment (figure 3.10), the average uptake coefficient of ozone onto a solution of iodide at the same concentration (figure 3.14) and the uptake coefficients for a bulk/surface system as calculated using equations 3.10, 3.11 and 3.12.

It can be seen from figure 3.17 that the deposition onto the solution containing both oleic acid and iodide is greater than just the deposition onto either constituent part alone suggesting that both the surface (organic) and the bulk (iodide) reactions are occurring in parallel. The deposition onto this solution is less than would be predicted by equation 3.10. This would indicate that there is some suppression of reactivity, probably caused by the organic layer on the aqueous surface blocking the transfer of ozone into the bulk water beneath it

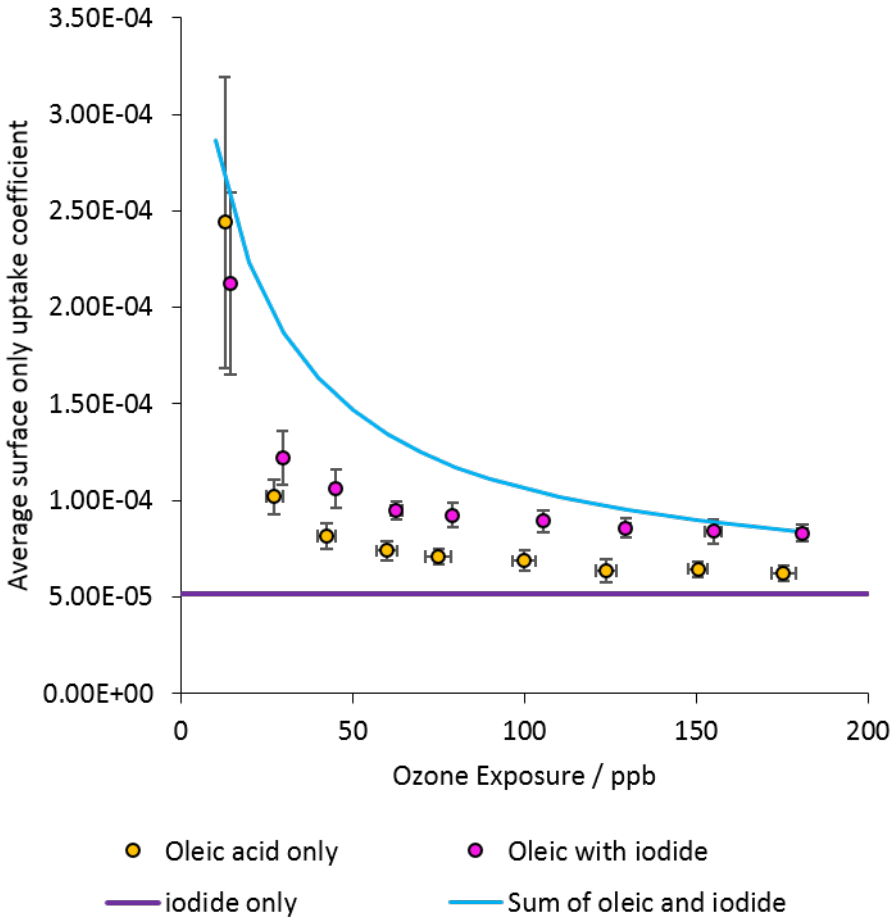

Figure 3.17: Surface only ozone uptake coefficient at changing ozone exposure levels for a synthetic seawater solution containing both oleic acid and iodide (pink circles) compared to the results of each component individually (oleic acid only - yellow circles, iodide only - purple line) and the mathematical combination of the two separate depositions (blue line). Error bars were calculated using equation 2.23

where the reaction with I^- can occur.

A curious phenomenon occurs at the lowest ozone mixing ratios, where the combination oleic/iodide uptake falls below that of oleic acid on its own. This could be indicative of a reactive system with a greater emphasis on the bulk (ozone-independent) reactivity, or could simply be a coincidence due to the high errors associated with uptake measurements at low ozone exposure in this setup.

3.9 Conclusions

The surface uptake coefficients of ozone onto nonanoic, oleic, linoleic and linolenic acids have been measured for ozone exposures between 20 and 190 ppb using a flask reactor. Uptake onto unsaturated fatty acids has been shown to occur via the Langmuir-Hinshelwood (LH) surface reaction pathway, as previously shown [48,86,152,154]. Apparent LH behaviour was also observed for the unreactive saturated fatty acid, nonanoic acid. Deposition here was attributed to dissolution of ozone, which is known to be more favourable than for a purely aqueous system. It is possible the observed LH behaviour is in fact an artefact of the dissolution if the organic substrate quickly reaches saturation. In this case, a constant offset would be observed from the ozone exposure level which would give a decreasing uptake profile with increasing exposure which would appear similar to a LH surface reaction. It has been shown that increasing the degree of unsaturation of a fatty acid increases the reactivity towards ozone. This can be attributed simply to the extra availability of reactive sites for compounds with more double bonds.

The uptake of ozone onto oleic acid was fit to a LH curve as carried out for the uptake of ozone onto solutions of anthracene and octanol by Mmereki and Donaldson [90]. The fit had a relatively low R^2 value (0.795) suggesting that the LH mechanism may not fully explain the reactivity occurring in this case. It is unlikely that bulk reactivity would account for the differences as bulk reactivity is independent of ozone concentration and the measured uptake of

ozone onto oleic acid shows a stronger ozone dependence than the LH fit.

An estimate for the surface reaction coefficient for oleic acid ($k^{II}_{oleic} = 1.64 \times 10^{-17}$ cm^2 molec^{-1} s^{-1}) was found to be lower than that reported in the literature for anthracene ($k^{II}_{anthr} = 2.6 \times 10^{-17}$ cm^2 molec^{-1} s^{-1}) which could be due to the much higher proportion of double bonds in the anthracene molecule offering more potential sites for a reaction with ozone to occur. A large potential source of error in this estimate is the estimation of collision cross section which makes lots of assumptions about the geometry of potential reactions including the angle of approach required for a reaction and the distance from the bond where reaction starts to occur. These are unavoidable approximations as calculating the surface area of a single bond is complex. A second error arises in the estimation of active surface sites.

A comparison between the reactivities of iodide and oleic acid to ozone was made by exposing ozone to a synthetic seawater sample containing both. The concentration of iodide used (1.5×10^{-4} M) had to be much greater than ambient marine concentrations so the magnitude of uptake for the two components would be similar. It was shown that at high ozone (> 30 ppb) the combination of iodide and oleic acid was more reactive then either oleic acid or iodide alone, though at low ozone exposure the combination could be less reactive. It is an unfortunate flaw of the method that the highest error bars are observed at the lowest ozone exposure values which is often when the most interesting results can be observed.

To develop this work further, combination experiments between iodide and linoleic or linolenic acid could be run to see if ozone is still able to penetrate into the bulk phase for more reactive organic surface layers. By averaging over an increased number of repeats the error bars could be reduced, even at the lowest ozone exposure levels which could give interesting information on the shape of the curve for the combination experiments.

Chapter 4

Measurement of ozone deposition to samples of seawater collected from the North Sea

4.1 Chemical controls on ozone deposition onto the surface ocean

The influence of various species to marine ozone deposition has been discussed several times in the literature. Chang *et al.* estimated the contribution of a number of processes including the surface chemical reactions of ozone with iodide, dimethyl sulfide (DMS) and alkenes (ethene and propene) by comparing the chemical ozone loss rates for each of those species [15]. Chemical ozone loss rates, q, were estimated based on reported second order rate constants and observed surface concentrations using equation 4.1. It was found that iodide had the greatest values for chemical ozone loss rate ($q_{I^-} = 7.3 \times 10^{-3} - 3.3 \times 10^{-2}$ m s^{-1}) compared to DMS ($q_{DMS} = 1.5 \times 10^{-4} - 1.3 \times 10^{-2}$ m s^{-1}) and alkenes ($q_{C=C} = 1.1 \times 10^{-5} - 1.5 \times 10^{-5}$ m s^{-1}). They therefore concluded that *"it is clear that the reaction between iodide and ozone is sufficient to explain the observed ozone deposition velocity"*. It is worth noting in this work that the concentrations of ethene and propene were used as proxies for the unsaturated organic content of the surface ocean which may not accurately represent the most reactive fraction of the marine organic content.

$$q_i = \frac{\sqrt{k_i C_i D}}{H} \tag{4.1}$$

The relative contributions to ozone deposition by the reaction with dissolved biogenically derived organic compounds was estimated by Clifford *et al.* [21]. In this work, chlorophyll was used as a proxy for this class of compounds as it is a significant marker for the ubiquitous activity of marine biota and is available for reaction with ozone due to its many unsaturated carbon carbon bonds. The ozone uptake coefficient for dissolved chlorophyll was determined to be $2 - 5 \times 10^{-6}$ at the atmospherically relevant ozone concentration of 1×10^{12} molecules cm^{-3}. This was compared to extrapolated uptake coefficients based on those measured for the reaction between ozone and dissolved iodide by Magi *et al.* [79]. These were determined to be of the same

order of magnitude ($\sim 5 \times 10^{-6}$) as those measured for chlorophyll suggesting the reaction between ozone and organic material at the ocean surface may be significant.

The reaction between ozone and dissolved chlorophyll was studied again under dark and light conditions by Reeser *et al.* [106]. The dark reaction was found to occur via Langmuir - Hinshelwood kinetics however under illumination this changed to a mechanism linear in gas phase ozone concentration. In the presence of both light and dissolved salt, the reaction between ozone and chlorophyll was found to occur at a much higher rate than either in the dark or irradiated in pure aqueous solution. This suggests that ozone loss via reactions with photochemically active unsaturated organic molecules on the surface ocean may represent an even greater proportion of the total ozone dry deposition.

A direct comparison of the contributions of dissolved iodide and dissolved organic material was carried out by Martino *et al.* [80]. The commercially available Suwannee River Natural Organic Material was used in this work as a proxy for marine DOM, containing various large, unsaturated humic molecules. This material is more unsaturated than true marine DOM, which could lead to an overestimation of the contribution of organic reactions to ozone loss in this work. At naturally occurring concentrations ($[I^-] = 150$ nM, $[DOM] = 40 - 80$ nM) values for chemical deposition velocity ranged from $0.005 - 0.010$ cm s^{-1} for both dissolved iodide and DOM with exposure to an ozone mixing ratio of 40 ppb. Chemical deposition velocity values was also obtained for a sample containing both dissolved iodide and DOM, in this case $v_d^c = 0.012$ cm s^{-1} i.e. $\sim$80% of value of the combination of the measured depositions of iodide and DOM indicating that the competing reactive pathways may be suppressing one another. This agrees with the results presented previously in this work where the ozone uptake onto a sample containing both oleic acid and dissolved iodide was 75-85% of the value obtained by directly summing the measured depositions of the constituent parts in solution alone.

4.2 Aims of the work presented in this chapter

The first aim of this work was to determine experimentally the ozone uptake coefficient of samples of real SML and compare the reactivity to corresponding samples of underlying, bulk water.

The second aim was to compare the deposition of ozone due to iodide to that of the total measured deposition. This was done by measuring the dissolved inorganic iodine concentrations in each seawater sample and calculating an iodide only value for deposition, which could be directly compared with the measured deposition.

The third aim was to compare the reactivity to ozone of each particular seawater sample with other measurements of the composition and physical properties of the sample to see whether any relationships could be observed.

4.3 Methods for the collection of sea surface microlayer samples

The SML is nominally defined as being the top 1000 μm of the ocean surface, but in practice the layer is operationally defined by the thickness that can be collected during an in situ study. In most recent studies, SML samples have been collected using one of four methods, the screen sampler, the glass plate, the rotating drum and the rotating glass disk.

The screen sampler was developed by W. D. Garrett in 1965 to "collect and recover the constituents of natural oceanic slicks" [37]. The sampler comprised of a steel wire mesh which is dipped vertically into the surface ocean then withdrawn parallel to the surface. Water and surface material are held within the gaps of the mesh by surface tension. After multiple surface contacts, the surface efficiency was reported to have decreased to 70% as on the initial contacts some surface material adheres permanently to the screen deactivating

it to any further surface adhesion.

In this first study, the thickness of the SML collected was reported as 150 μm. The thickness of SML samples collected by this method has been shown to be largely independent of oceanic conditions such as water temperature and salinity [10], though there are conflicting reports on whether wind speed has any effect. A report from Carlson (1982) suggested that wind speed did not have any bearing on the thickness of the microlayer collected [10], though more recent reports from Falkowska (1999) found that increasing wind speed led to increases in the amount of microlayer collected by the screen method [26]. It was suggested that this effect was due to the increased turbulence of the surface ocean causing more organic material to be transported to the SML. However, at wind speeds higher than 8 m s^{-1} the thickness of SML collected decreased. It is known that increases above this critical speed produce a larger effect on wave height that increases below, but it is not yet known how exactly this causes the microlayer thickness to decrease [141].

The glass plate method is very similar in operation to the Garrett screen and was developed by Harvey and Burzell (1972) [47]. The glass plate (20 cm $\times$ 20 cm) is placed into the water and withdrawn vertically at a rate of about 20 cm s^{-1} and both sides wiped clean with a neoprene wiper. 1 L of SML material was collected in 45 minutes, at thicknesses slightly thinner than by the screen method of 60 – 100 μm. A comparison between the screen and glass plate samplers found that the glass plate was less efficient than the screen, taking approximately 8 times longer to sample 1 L of SML material though the glass screen did collect a thinner SML (40 – 60 μm compared to 200 – 300 μm) [34]. It has been shown that it is not only the thickness of the layer that changes from screen to glass plate method, but also the types of material collected. Momzikoff *et al.* (2004) showed that the glass plate method was more efficient at collecting amino acids, phytoplankton waste and biogenic saturated fatty acids. The screen method was shown to be more efficient as collecting phytoplankton organisms. The recommendation is that for the study of ocean atmosphere interactions the glass plate is used [93].

Many different versions of the rotating drum sampler have been used in the literature to collect SML samples. The first drum sampler was used by Harvey (1966) and could automatically collect SML samples from a remote-controlled boat [46]. The drum was 38 cm in diameter and 60 cm long and coated in a hydrophilic ceramic causing surface water to adhere to it as it rotates through the surface water. A neoprene wiper is held tightly against the downward side of the drum wiping all material off into a collection vessel. The thickness of the microlayer depends on the rotation speed of the drum and on the water temperature; an increase of 12% thickness was reported from 20 ^{o}C down to 16 ^{o}C (60.0 – 67.2 μm respectively). This method allowed for the collection of more material in less time than using a manual sampler and with much less effort. Versions of the rotating drum coated in other materials have been reported such as a glass coated drum [11] and a Teflon coated drum [45]. For best results the rotation axis of the drum must be parallel to direction of movement to avoid accumulation of solids and other unwanted material on the face of the drum [11].

A more recent advancement in the field of SML collection is the rotating disk method. First proposed by Eek (SOLAS, 2005) several discs are mounted onto the front of a remote-control boat and the base of the discs rotated through the water. A neoprene wiper on either side of each disc collects the material that accumulates on it. This method supposedly can operate in rougher conditions that the drum and causes a lesser disturbance on the surface water as its vertical profile is much slighter. The first rotating glass disc sampler was tested in the lab to determine the best method for estimating the thickness of SML collected by this method [121]. Two theoretical estimations, one taking into account liquid viscosity and disc angular momentum and the other taking into account surface tension and gravity [72, 119], were compared to two experimental methods, one comparing collected volume to active surface area and one using spectroscopy to measure the thickness of liquid on the disc. The spectroscopic method involved rotating the disc through a dye solution and measuring the absorbance through the disc and solution. Using the Beer-Lambert law the pathlength could then be found. There was poor

agreement between this method and the more traditional method of using the ratio of collected volume to active surface area with the traditional method estimating lower thicknesses at lower rotation speeds and greater thicknesses at higher rotation speeds. This could perhaps be due to differences in surface tension or viscosity of the samples containing the dye compared to salt water or sea water samples. Another possible reason for the divergence could be that at low rotation speeds recovery from the wipers is lower than 100% due to losses of the sample on the disc due to gravity. In a recent study, six glass discs were mounted onto the front of a remote catamaran to sample SML in the Baltic Sea and North Sea [109]. In order to minimise the uncertainty in SML thickness, the rotation speed of the discs were set to 7 rpm where the two methods are in agreement of thicknesses of 50-80 μm.

A comprehensive review from Cunliffe and Wurl provides a detailed summary of the best sea surface microlayer and underlying water sampling methods and protocols [23]. Table 4.1 provides a summary of the advantages and disadvantages of several sampling methods.

Table 4.1: Advantages and disadvantages of various SML sampling methods from Cunliffe and Wurl, 2014 [23]

Method	Advantages	Disadvantages
Garrett screen	• Can be deployed in rough seas • Rapid deployment and high sampling rates • Good time and spatial resolution • Reproducible sampling for analysis of dissolved gases • Well suited for collecting large biological species such as diatoms	• Collects very thick samples • SML material often diluted by material from greater depths • Sample thickness strongly dependant on environmental factors (water temperature, wind speed, wave height, etc.) • Some material remains on screen after collection
Glass plate	• Cheap to make and simple to operate • Can collect all sample adhered to plate • Can be highly reproducible sample thickness	• Sampling is time consuming and labour intensive • Large plates are heavy and unwieldy • Sample thickness dependant on consistency of withdrawal rate

Method	Advantages	Disadvantages
Glass plate (*cont.*)	• Well suited for collection of hydrophobic DOM and small particles • Collects thin SML samples	• Strong temperature effect on sample thickness • Poorly suited when large sample volumes required • Poor reproducability of dissolved gas content • Leaching of trace elements from glass can contaminate samples
Membrane sampler	• Can collect very thin samples (¡ 50 μm) • Little specialised equipment required • Low preparation and clean-up as samplers are single use • Well suited for collection of biological samples such as bacteria	• Low surface area leads to small sampling volumes • Fragile in windy conditions
Autonomous devices	• Can predictably control sampling thickness • Can have built in *in situ* measurements • Very fast collection of material • Simultaneous collection of SML and ULW samples	• Costly and difficult to transport • Complex setup and deployment procedures • Can be difficult to see the water being sampled if deployed at a distance

4.4 Sampling SML during the Microlayer at night Campaign

SML and subsurface waters were collected during the MILAN campaign. MILAN was carried out in Jade Bay, a large basin in the semitidal Wadden Sea region of the North Sea, figure 4.1. Seawater samples were collected during five sampling expeditions, including three diurnal cycles, using a remote control catamaran, the Sea Surface Scanner (S^3) [109]. Details of the sampling dates and times are given in table 4.2.

Table 4.2: Details of when samples were collected during the MILAN campaign. Day samples were collected at approximately midday, night samples were collected at approximately midnight

Date	Samples collected
03/04/17	Day only
04/04/17	Diurnal pair
06/04/17	Day only
08/04/17	Diurnal pair
11/04/17	Diurnal pair

SML samples were collected using the glass disk method; six glass disks (diameter 60 cm, thickness 0.8 cm, separation 5 cm) were mounted between the hulls of the catamaran and immersed in the ocean surface by approximately 15 cm. Figure 4.2 shows the glass disks on the catamaran prior to deployment and the surface sampler deployed on the ocean. The disks were rotated through the surface water at 7 rpm and adhered water was collected by wipers on the downward side of the disks.

Subsurface water was collected through a pipe mounted underneath the S^3 at a depth of 1 m. The pump was activated only when the disks were rotating for simultaneous collection of SML and subsurface water. SML and subsurface water samples were collected in large batches of 20 L every 2-3 hours at a rate of 20 L hr^{-1}. The S^3 was also fitted with a range of onboard sensors to measure

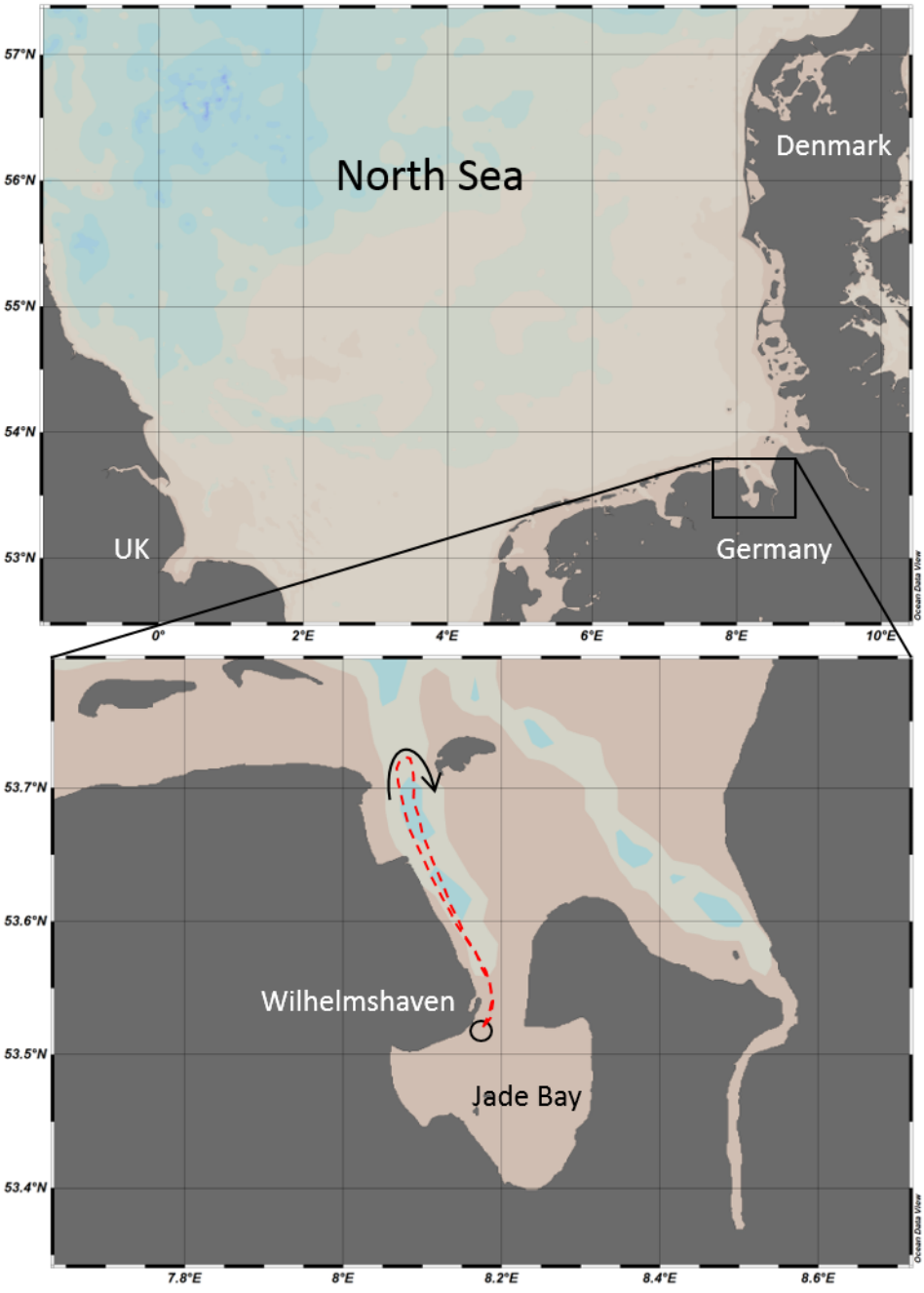

Figure 4.1: Locations of all samples collected during the MILAN campaign. On each occasion the remote control catamaran, supported by a research vessel, embarked from the jetty in Wilhelmshaven, Germany, and followed the red line on a loop out of the bay. A full loop lasted approximately 24 hours

Figure 4.2: Top: Glass disks mounted onto the front of the sea surface scanner (S^3). Bottom: the S^3 deployed in the Jade Bay

the physiochemical properties (such as temperature and conductivity) of the SML and subsurface waters *in situ*.

During each sampling expedition the S^3, accompanied by a research vessel, followed the path of a drifting buoy as it was carried by the tide through the bay.

SML and subsurface water samples were vacuum filtered through pre-combusted (5 hrs at 400 ^{o} C) Whatman GFF filters before being split for analysis: ozone deposition profiles (200 mL), iodide and iodate (50 mL), SPE-DOM (2 L SML, 7 L subsurface). All glassware used for transporting and storing samples had previously been rinsed with acid (HCl, 4%) and milli-q water.

4.5 SML sampling at Bridlington

Additional samplers were constructed for the manual collection of SML and subsurface water. A glass plate sampler was constructed from a pane of toughened glass (600 × 265 mm) with an acrylic handle. Ropes were tied through holes drilled into the handles of the sampler and the sampler lowered into the sea surface until fully submerged. Once the ocean surface had recovered (approximately 30 s) the sampler was lifted back through the sea surface at a steady rate (10 cm s^{-1}) with the glass plate perpendicular to the sea surface. Excess material was allowed to drain from the plate for approximately 20 s and then samples were wiped from both sides of the plate with a neoprene squeegee into an acid rinsed collection vessel (browned glass) with the aid of a plastic funnel. The glass plate and wiper were washed with ethanol (20 mL) and left in an acid bath for at least 12 hours; before use they were rinsed with milli-Q water. The plate, wiper, funnel and collection vessel were rinsed with sample by collecting and discarding the material from 10 dips.

A Garrett Screen was constructed out of stainless steel woven mesh (540 x 600 mm) mounted in a stainless-steel frame. The screen was cleaned by rinses

with ethanol (200 mL), tap water (3 L) and milli-Q water (4 L) before use. When sampling, the screen was lowered into the ocean by ropes mounted to each corner of the frame until it was fully submerged. Once the ocean surface had recovered (approximately 30 s) the screen was lifted back through the sea surface with the screen parallel to the sea surface. Excess material was allowed to drain off the screen and out of the hollow frame by holding the frame flat and still. To collect the SML sample, the frame was tilted so that all the remaining material on the screen poured out of a hole cut into the mesh and into an acid rinsed collection vessel (browned glass) with the aid of a plastic funnel. Immediately prior to sample collection the screen, funnel and collection vessel were rinsed with SML by collecting and discarding the material from three dips.

Subsurface water was collected with a plastic bottle mounted onto a pair of telescopic poles with one pole each attached to the body and lid of the bottle. With the lid screwed onto the bottle, the apparatus was submerged in the water at a depth of at least 20 cm. The pole attached to the bottle lid was rotated unscrewing the lid and allowing subsurface was to enter the bottle. To prevent contamination with surface material the bottle was resealed before the apparatus lifted out of the water. Samples were then poured into an acid rinsed collection vessel (browned glass) with the aid of a plastic funnel. Immediately prior to sample collection the subsurface sampler, funnel and collection vessel were rinsed with subsurface water by collecting and discarding the material from a single dip.

Prior to use on the ocean, the samplers were tested on the campus lake at the University of York on three separate occasions in January and February 2018. The number of dips for each sampler were recorded as well as the total volume of surface material and the total duration of sampling. Details of average sampling rate and surface sample thickness for each sampling method are given in table 4.3.

It was assumed that the values recorded in table 4.3 would be over estimations of the sampling capacity of the samplers in real seawater as the lake was

Table 4.3: Sampling details for the Garrett Screen and Glass Plate samplers during testing

Method	Average sample thickness / μm	Average sampling rate / L hr^{-1}
Garrett Screen	307 ± 12	5.32 ± 1.03
Glass Plate	47 ± 12	0.46 ± 0.02

much more still than the ocean surface and visible slicks on the surface indicated that there was a lot of organic material to be sampled. The glass plate was able to collect a much thinner layer of surface material than the Garrett Screen, as expected but at a much lower rate. It was decided that for sampling expeditions to collect real SML only the Garrett Screen would be used. This decision was made as the time available on the water for sample collection was very limited, and the Garrett Screen could collect more material in the same length of time. Garrett Screens are typically used in ocean studies of the SML, particularly when large volumes of material are required [**?**, 23]. As the definition of SML depth is essentially arbitrary and depends on the sampling method used in collection, it was decided that the sampling thickness was not an important factor for selecting which sampler behaved better.

SML and bulk underlying water (ULW) samples were collected from the North Sea, 6-8 km east of Flamborough Head, Bridlington on three occasions in 2018 (May 5^{th}, August 15^{th} and October 17^{th}), figure 4.3. Samples were stored in brown glass bottles after collection to minimise the effects of sunlight on the biology and photochemistry occurring within the samples. Upon returning to the lab, SML and subsurface water samples were vacuum filtered through pre-combusted (5 hrs at 400 ^{o} C) Whatman GFF filters and frozen at -18 ^{o}C.

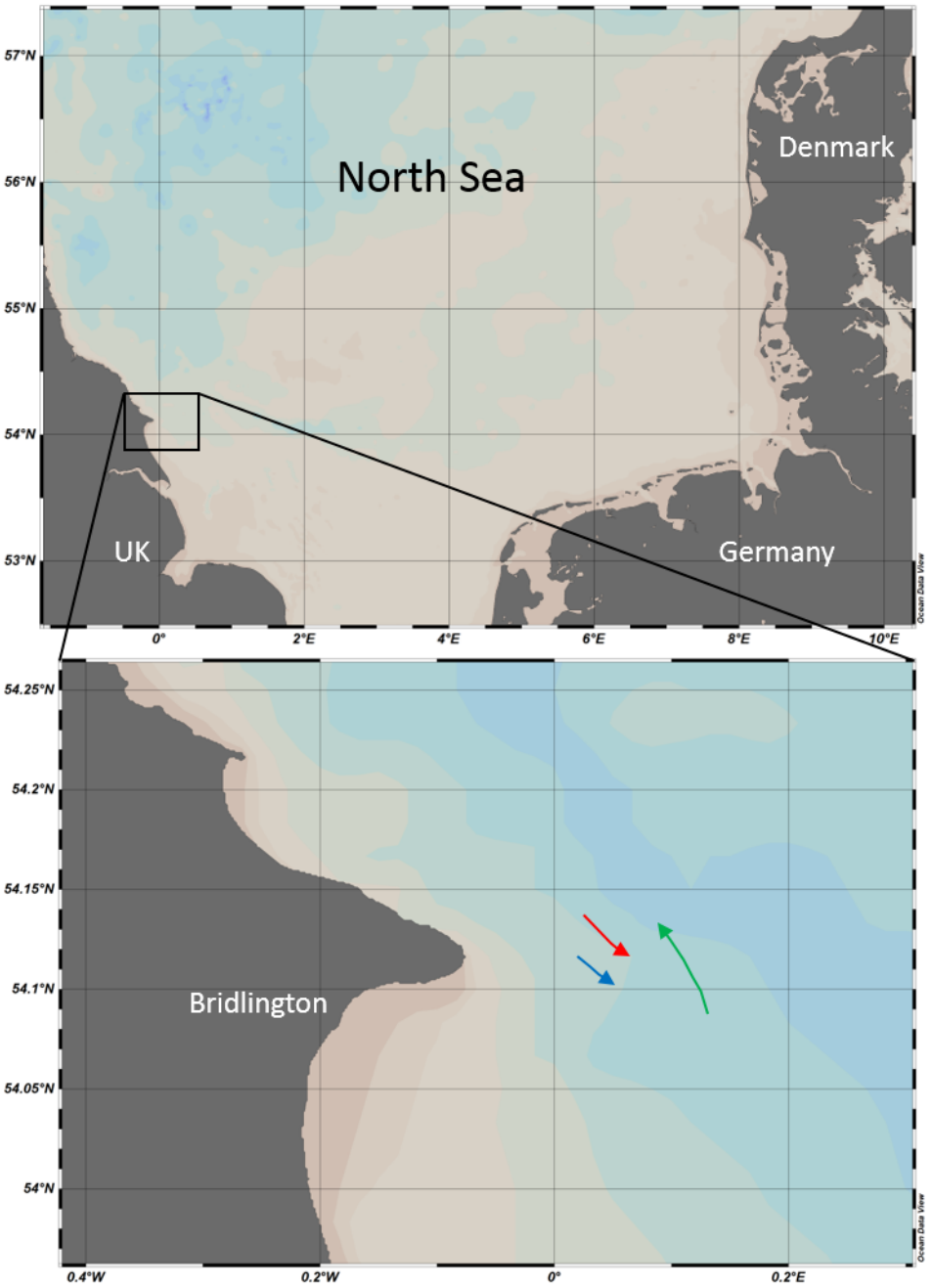

Figure 4.3: Locations of samples collected near Bridlington, UK on the 4^{th} May (red line), 15^{th} August (green line) and 17^{th} October (blue line) 2018. In each case when sampling, the engine of the boat was switched off and the boat drifted along the courses in the directions marked by the arrows. Samples were collected over the course of 2-3 hours

4.6 Control experiments in the flask reactor

Ozone deposition experiments were carried out using the round bottomed flask reactor as described previously (figure 3.3). Flow conditions through the flask and monitor are given in table 4.4. As the flow demand into the monitor was higher than the flow rate supplied through the flask for the MILAN experiments, the excess flow was made up by a diluent of filtered lab air using the overflow carbon filter in figure 3.3. A blank experiment was conducted with an empty flask under the MILAN flow conditions as given in table 4.4 to measure the ozone loss to the walls and tubing of the reactor setup (figure 4.4).

Table 4.4: Flow conditions and aerodynamic resistance values for the ozonolysis of seawater samples collected during MILAN and off Bridlington

Samples	Ozone flow rate / sccm	Monitor flow demand / sccm	R_a / cm^{-1} s
MILAN	2200	2550	1.58 ± 0.16
Bridlington	1260	1260	1.57 ± 0.51

From figure 4.4 it can be seen that there is a small increase of 4.7% in the ozone signal passing through the empty reactor compared to the bypass line. This small error is attributed to changes in the pressure occurring when the ozone moves through the flask. To account for this, all measurements of ozone through the flask under MILAN flow conditions are divided by the correction factor 1.0465.

Aerodynamic resistance values were measured over a buffered solution of iodide at high concentration (0.1 M, pH 8.0) over a range of ozone mixing ratios. Values of R_a are given in figure 4.5 for the MILAN experimental conditions and in the previous section (figure 3.7) for the Bridlington flow conditions. Average values for R_a under each set of flow conditions are given in table 4.4.

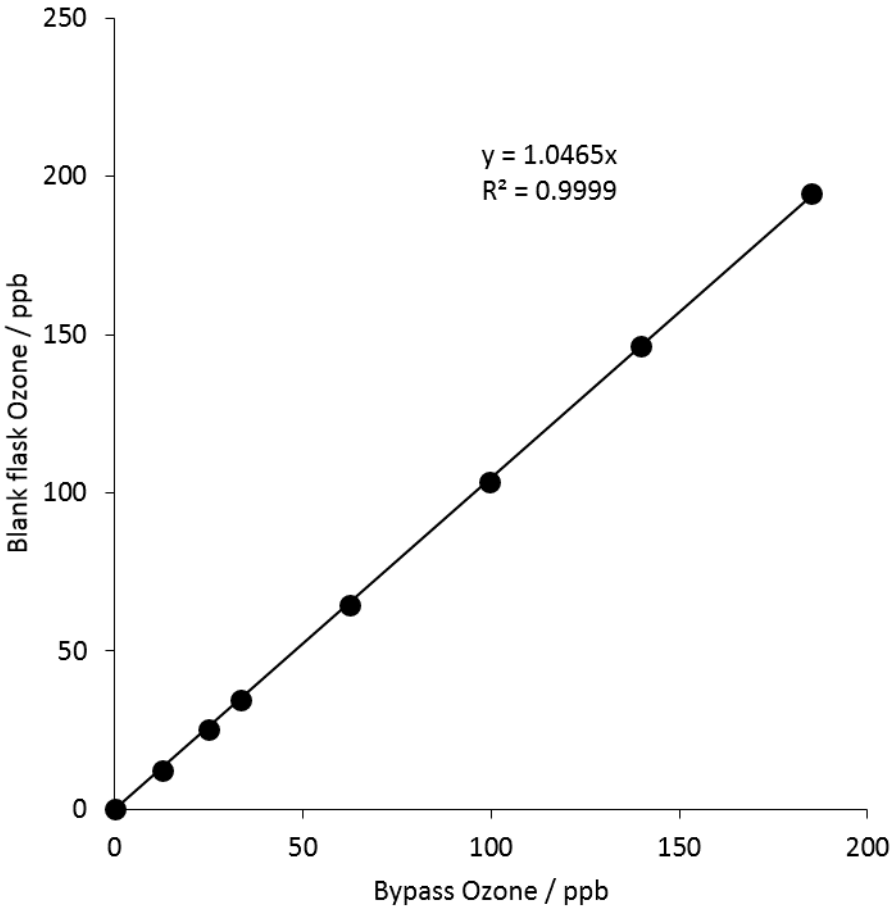

Figure 4.4: Average ozone mixing ratios measured through the bypass line and flask under MILAN flow conditions. Error bars of one standard deviation are too small to be seen on the scale of the graph

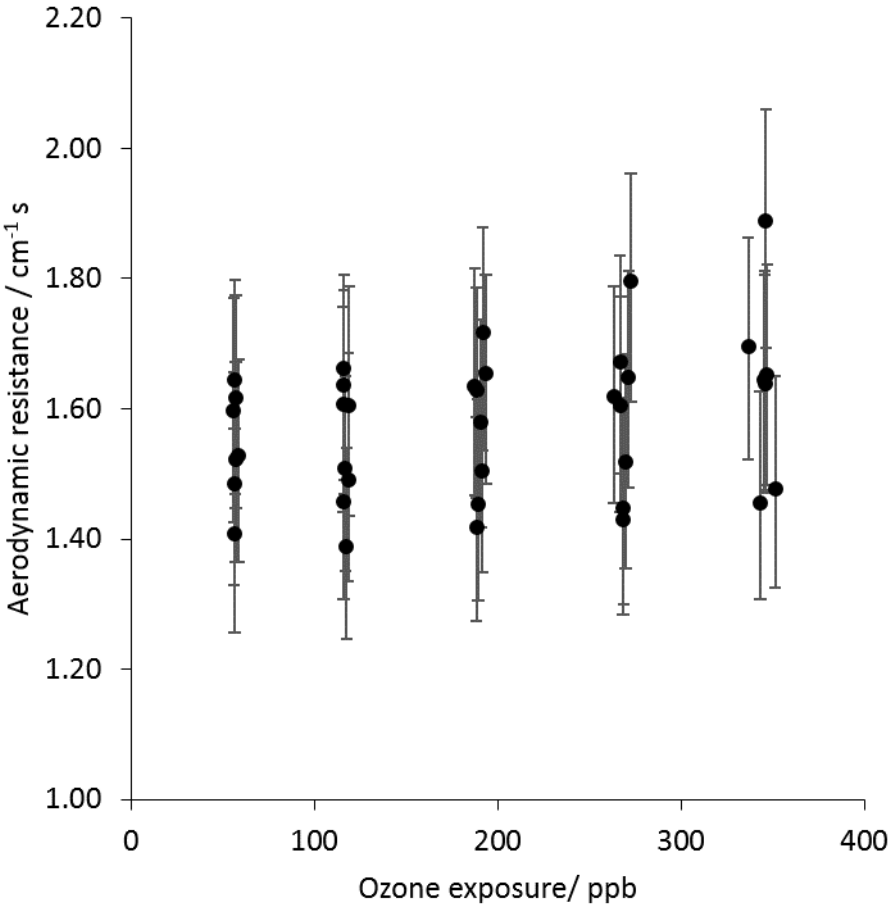

Figure 4.5: Aerodynamic resistances for the flask reactor under MILAN flow conditions. Error bars are calculated from the uncertainty in each average initial and final ozone measurement propagated forward

4.7 Measured ozone deposition to samples of SML and underlying water collected off the coast of Bridlington

Ozone deposition profiles showing the surface only deposition velocity (with aerodynamic resistance taken into account) for SML and ULW samples collected from near Bridlington are shown in figures 4.6, 4.7 and 4.8. Frozen samples were thawed overnight prior to analysis. Each sample was analysed in triplicate (yellow, grey and blue circles in figures 4.6, 4.7 and 4.8) starting at the highest mixing ratio of ozone ($180 - 200$ ppb) and descending through the exposures. After ozone deposition at the lowest mixing ratio was measured, the ozone level was returned to the maximum value to check the surface had not changed over the course of the experiment.

In general, it can be seen from figures 4.6, 4.7 and 4.8 that the repeats at the high ozone exposure levels are all close together, demonstrating that there is not a measurable change in the sample composition during the experiment. Overall the method demonstrates good reproducability, with exception of one repeat of the underlying water sample collected on May 4^{th} (blue circles) which shows a flat profile. All other repeats of all samples show the expected descending curve of ozone deposition velocity with increasing ozone exposure levels typical of the Langmuir - Hinshelwood surface mechanism.

As in previous experiments, the largest deviations between repeats and highest errors were observed at the lowest ozone exposure levels, although in all cases the deviations in deposition velocities are within error bar overlap. The source of these errors is again attributed to the noise from the ozone monitor which itself is independent of the ozone exposure and so is much more relevant at the lowest ozone levels.

Figure 4.9 shows the averaged surface only deposition velocities for the surface and subsurface samples from each sampling date. Error bars are propagated forward from those shown in figures 4.6, 4.7 and 4.8 as shown previously

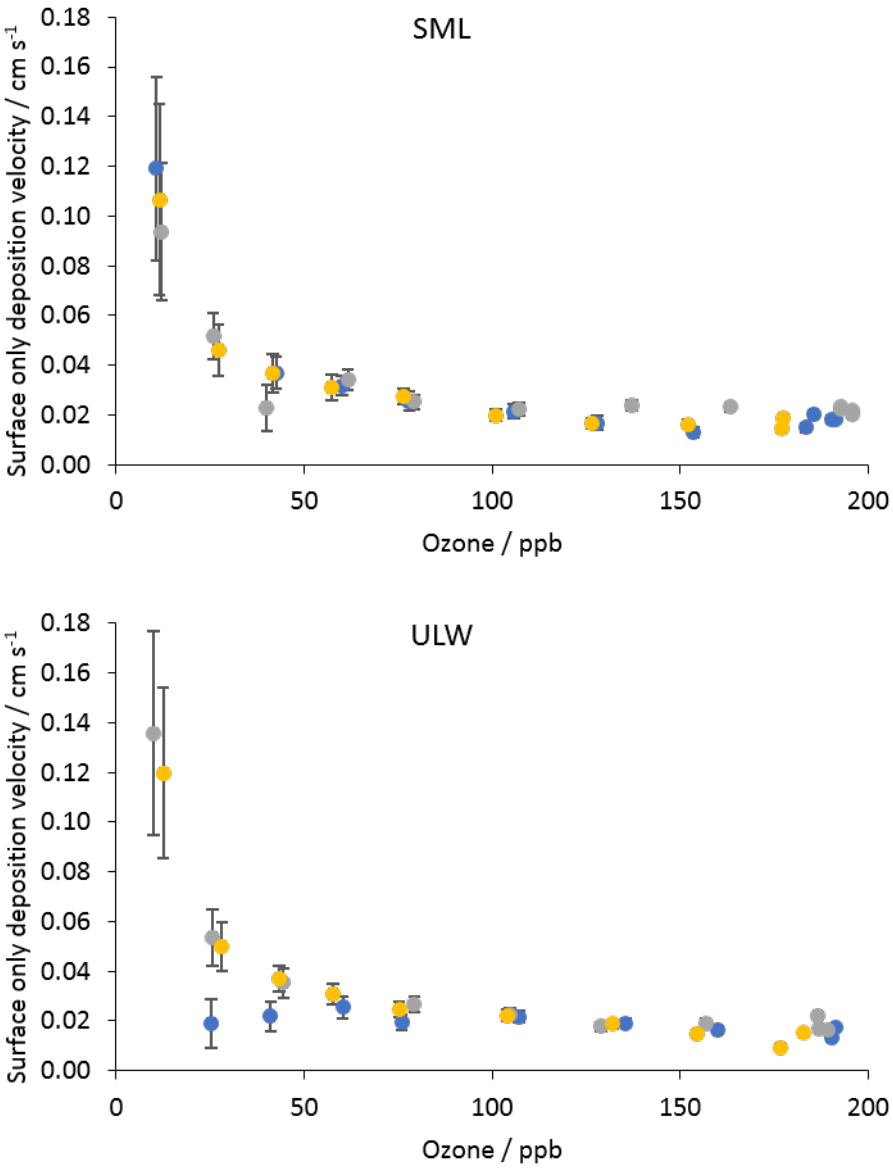

Figure 4.6: Surface only ozone deposition velocity onto SML (top) and ULW (bottom) samples collected off Bridlington on 04/05/2018. Coloured circles are different repeats. Error bars are calculated from the uncertainty in each average initial and final ozone measurement propagated forward

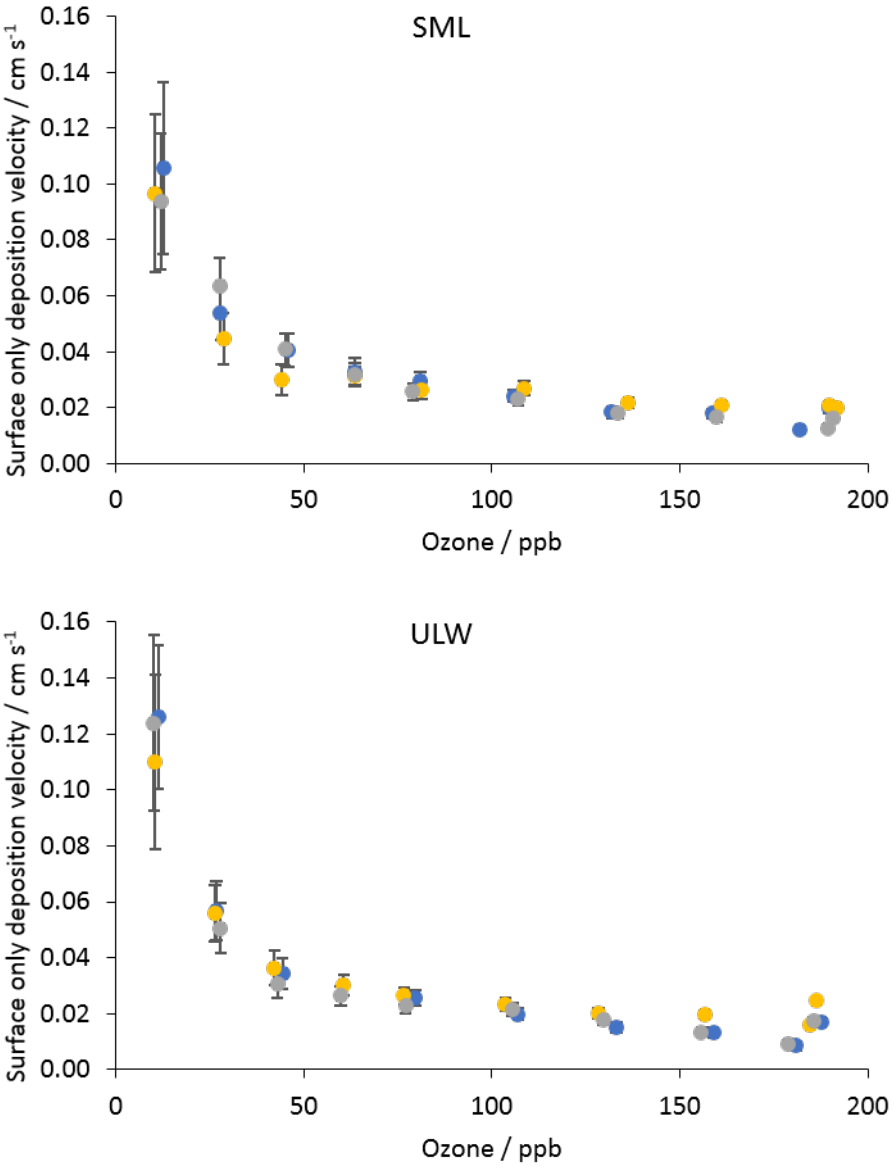

Figure 4.7: Surface only ozone deposition velocity onto SML (top) and ULW (bottom) samples collected off Bridlington on 15/08/2018. Coloured circles are different repeats. Error bars are calculated from the uncertainty in each average initial and final ozone measurement propagated forward

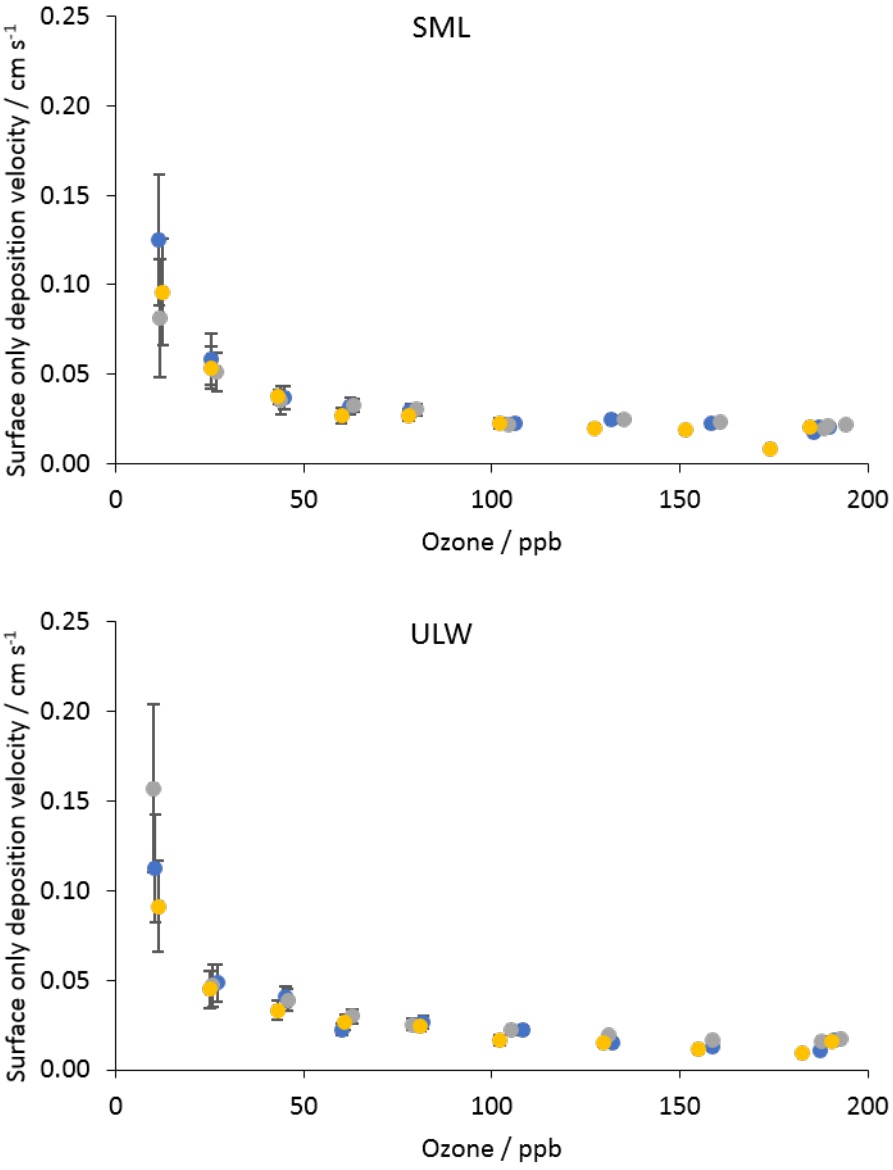

Figure 4.8: Surface only ozone deposition velocity onto SML (top) and ULW (bottom) samples collected off Bridlington on 17/10/2018. Coloured circles are different repeats. Error bars are calculated from the uncertainty in each average initial and final ozone measurement propagated forward

in equation 2.23.

It can be seen from the comparisons between surface and subsurface waters in figure 4.9 that the differences in the reactivities of these two classes of sample are very slight, and often fully within the error bars. In all cases, at the lowest ozone exposure levels the SML samples show lower reactivities than the underlying waters and at mid to high ozone exposure levels the two curves converge with a slightly higher deposition onto the surface water. This has the effect of reducing the angle of the slope of the SML curves which could indicate that the reactive mechanism has more bulk character to it than that of the underlying water samples.

The surface tension of each of the unfiltered, unfrozen samples were measured by L. King and L. Tinel (unpublished work) using the De Noüy ring method, values are shown in figure 4.10. In all three cases, the surface tension of the bulk, underlying water is significantly higher than that of the SML as would be expected of an organic film on an aqueous bulk [153]. Unlike in the ozone deposition experiments, the surface tension values shown in figure 4.10 demonstrate that there is a measurable difference in the composition of the SML and ULW samples. This would suggest that the chemical constituents of the SML and ULW responsible for the differences in surface tension are not reactive towards ozone and are probably saturated organic molecules.

4.8 Measured ozone deposition to samples of SML and underlying water collected during the MILAN campaign

Ozone deposition profiles showing the surface only deposition velocity (with aerodynamic resistance taken into account) for SML and ULW samples collected during the MILAN campaign are shown in figures 4.11, 4.12,4.13, 4.14 and 4.15. Samples were analysed immediately after filtering. Each sample

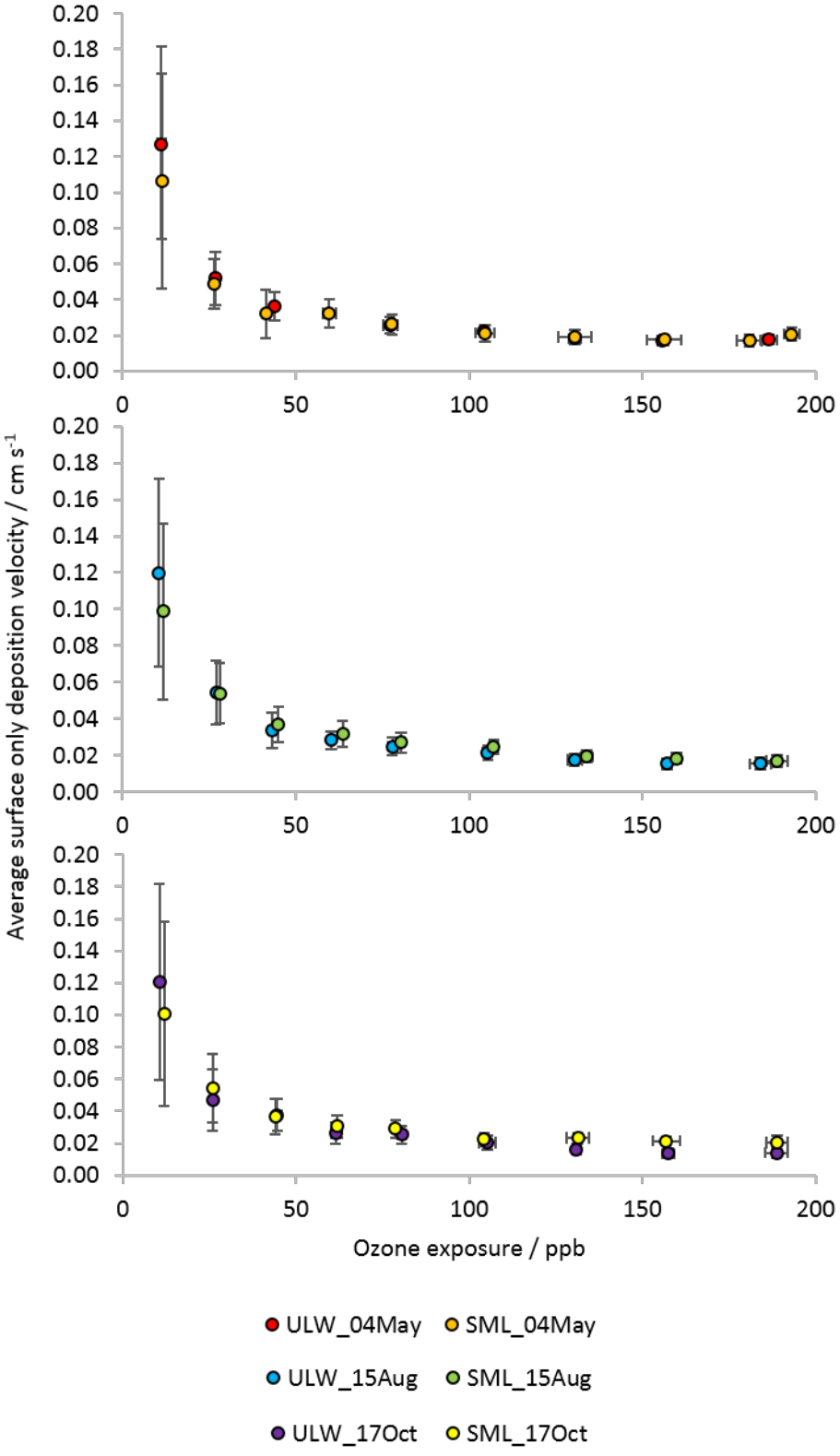

Figure 4.9: Average surface only ozone deposition velocity onto SML and ULW samples collected off Bridlington on 04/05/2018 (top), 15/08/2018 (middle) and 17/10/2018 (bottom). Error bars are calculated from the uncertainty in each average initial and final ozone measurement propagated forward

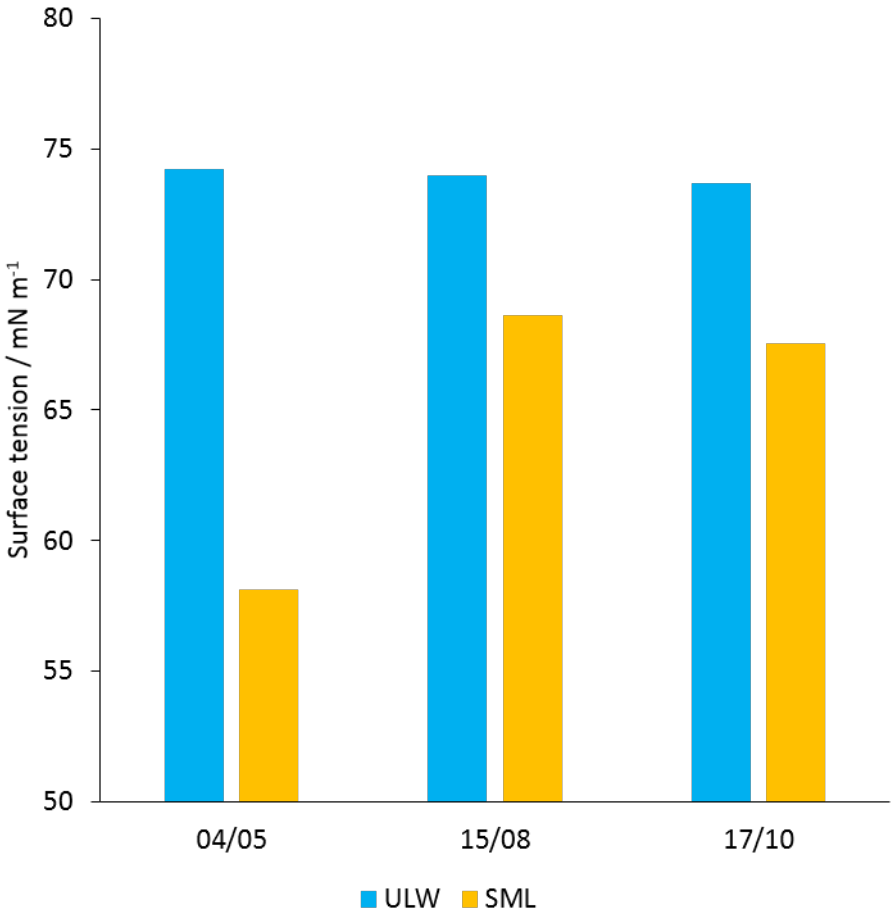

Figure 4.10: Surface tension values for the surface (yellow) and underlying (blue) water samples collected off Bridlington. Errors of one σ are too small for the scale of the graph

was analysed starting at the lowest mixing ratio of ozone ($10 - 20$ ppb) and ascending through the exposures.

The samples generally show Langmuir - Hinshelwood (LH) type curved profiles, though some show more pronounced LH behaviour than others. For the samples in the later end of the sampling period (for example the samples collected on 11/04/2017, figure 4.15), the profiles appear much flatter than those at the start of the sampling period, and are often, within error, totally flat i.e. showing constant ozone deposition with changing ozone exposure. This suggests that for the later samples in particular, the reactivity may be heavily influenced by a bulk reaction mechanism rather than LH kinetics. The heterogeneous reactions between ozone and organic material generally show LH behaviour, as demonstrated in the literature for the reaction with oleic acid [151], polycyclic aromatic hydrocarbons [57] and anthracene [67], for example.

It can be seen that in general the SML samples show similar reactivities to the underlying water samples though in some cases the subsurface water appears to be more reactive towards ozone (figures 4.11 and 4.14). The water around the Jade Bay was very turbid and visually concentrated in particulate matter. This could suggest a higher than normal organic concentration in the entire surface ocean, not just the SML. To compare between multiple sample pairs on multiple days, the ozone deposition at approx. 50 ppb was plotted for each SML and subsurface sample over time in figure 4.16.

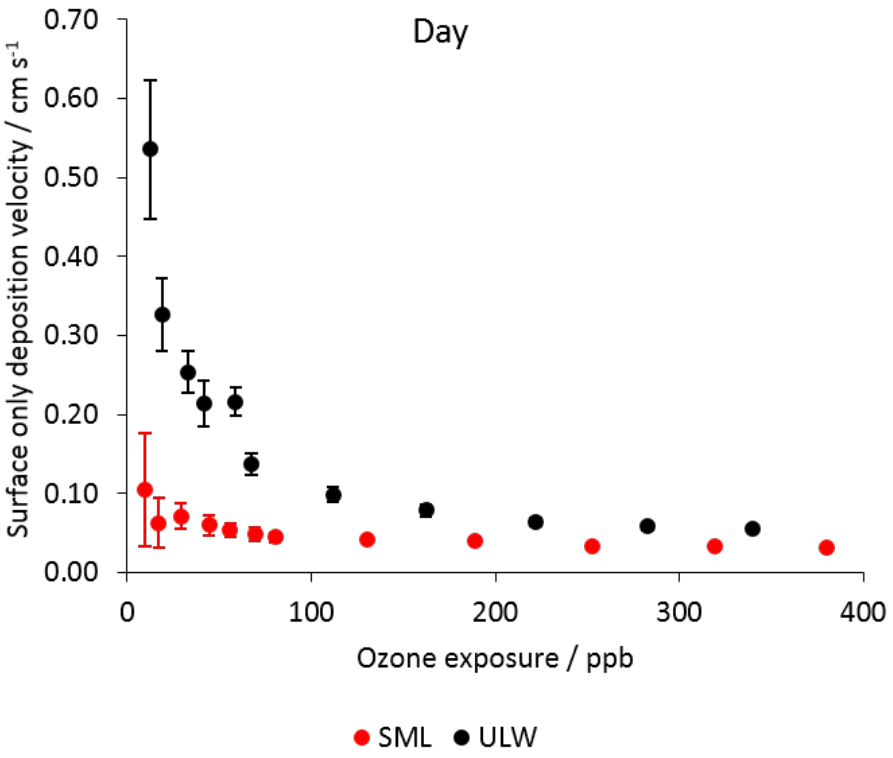

Figure 4.11: Surface only ozone deposition velocity onto day SML (red) and ULW (black) samples collected during the MILAN campaign on 03/04/2017. Error bars are calculated from the uncertainty in each average initial and final ozone measurement propagated forward

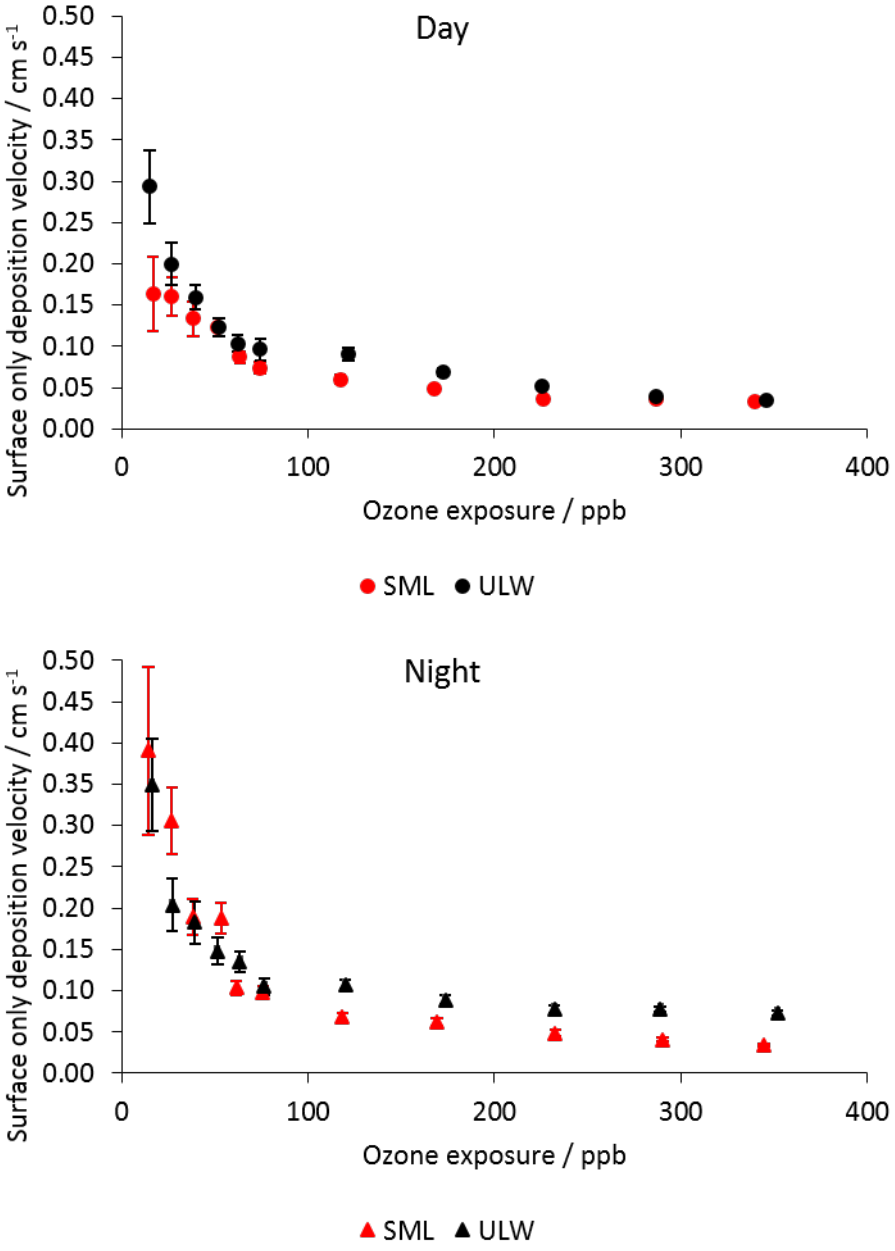

Figure 4.12: Surface only ozone deposition velocity onto day (circles) and night (triangles) SML (red) and ULW (black) samples collected during the MILAN campaign on 04/04/2017. Error bars are calculated from the uncertainty in each average initial and final ozone measurement propagated forward

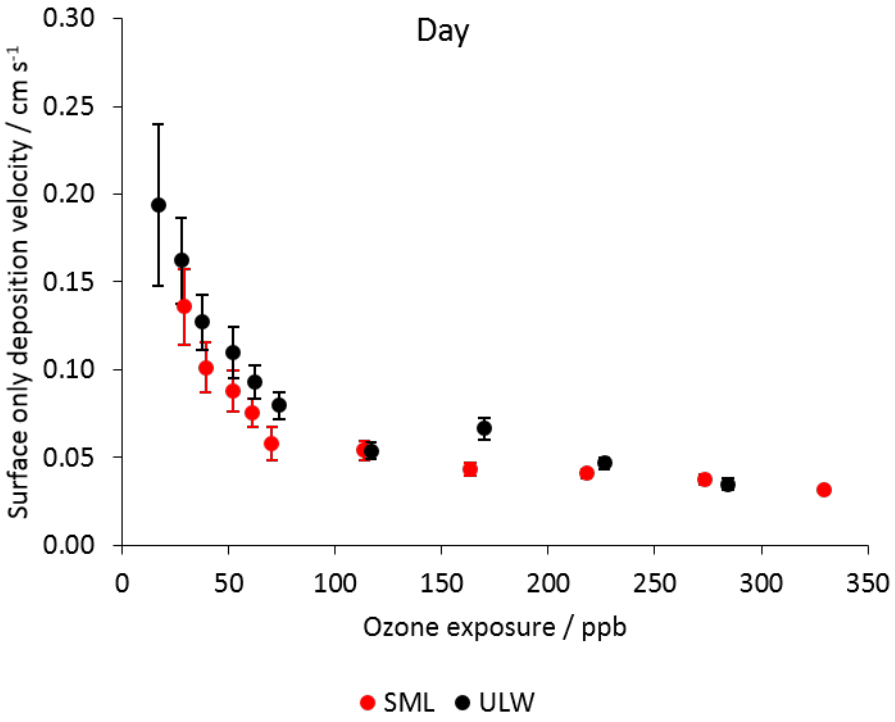

Figure 4.13: Surface only ozone deposition velocity onto day SML (red) and ULW (black) samples collected during the MILAN campaign on 06/04/2017. Error bars are calculated from the uncertainty in each average initial and final ozone measurement propagated forward

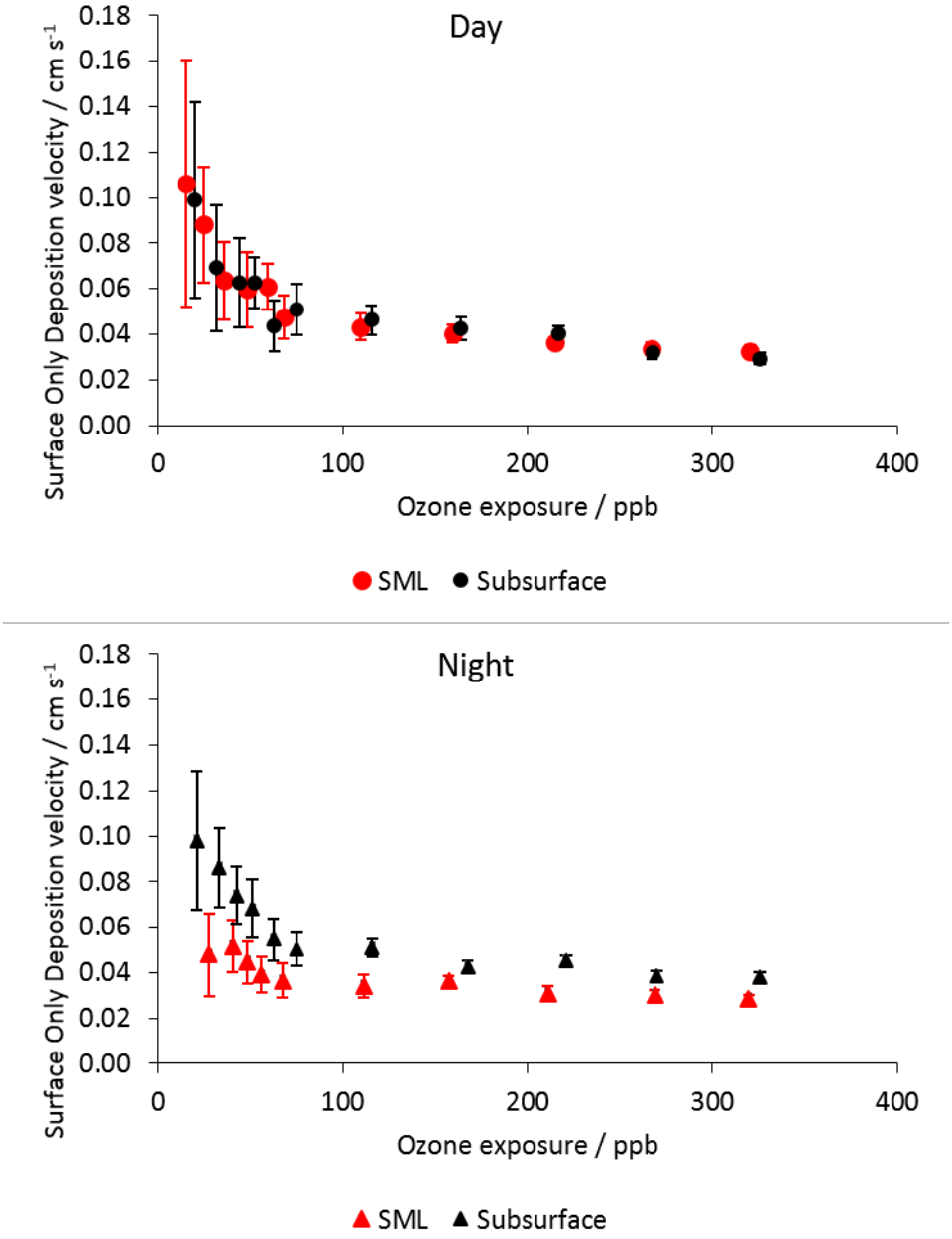

Figure 4.14: Surface only ozone deposition velocity onto day (circles) and night (triangles) SML (red) and ULW (black) samples collected during the MILAN campaign on 08/04/2017

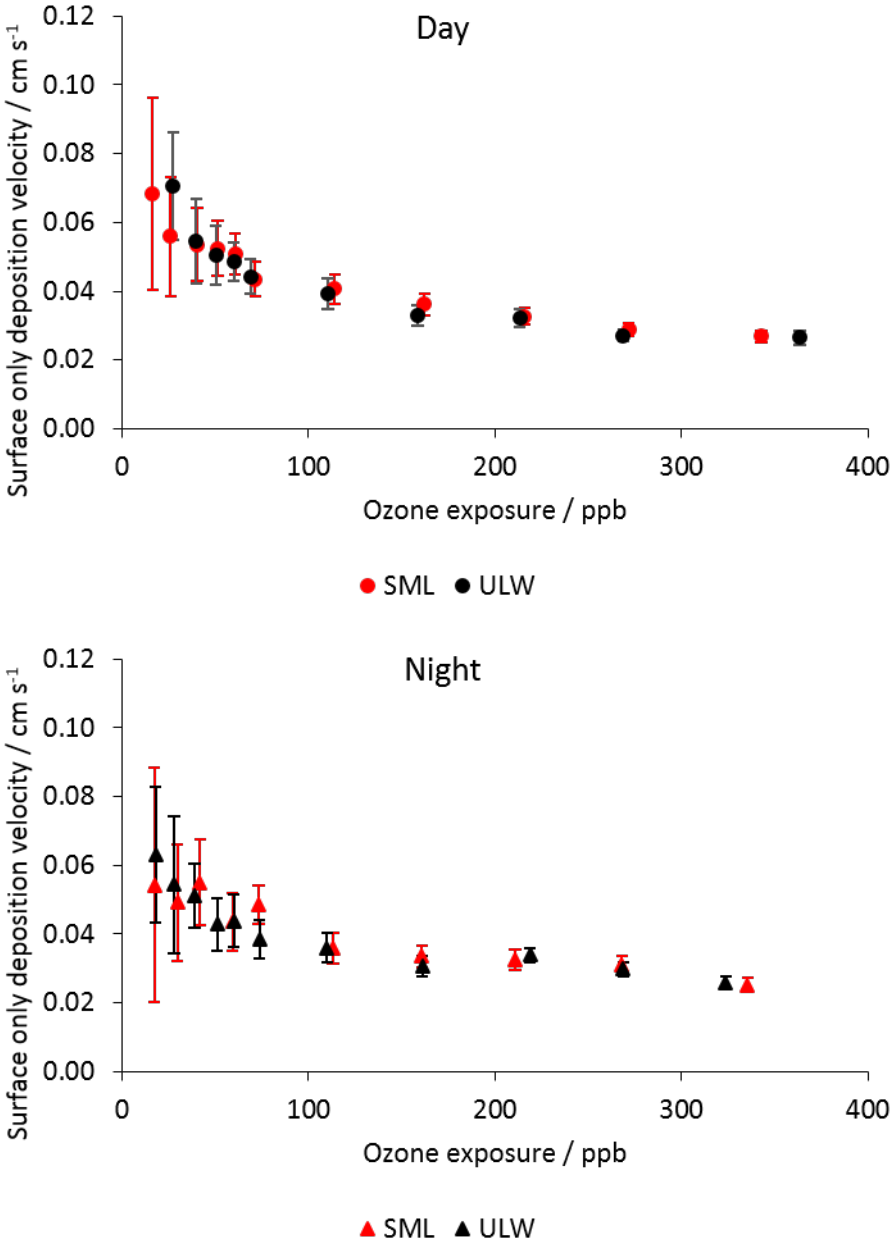

Figure 4.15: Surface only ozone deposition velocity onto day (circles) and night (triangles) SML (red) and ULW (black) samples collected during the MILAN campaign on 11/04/2017

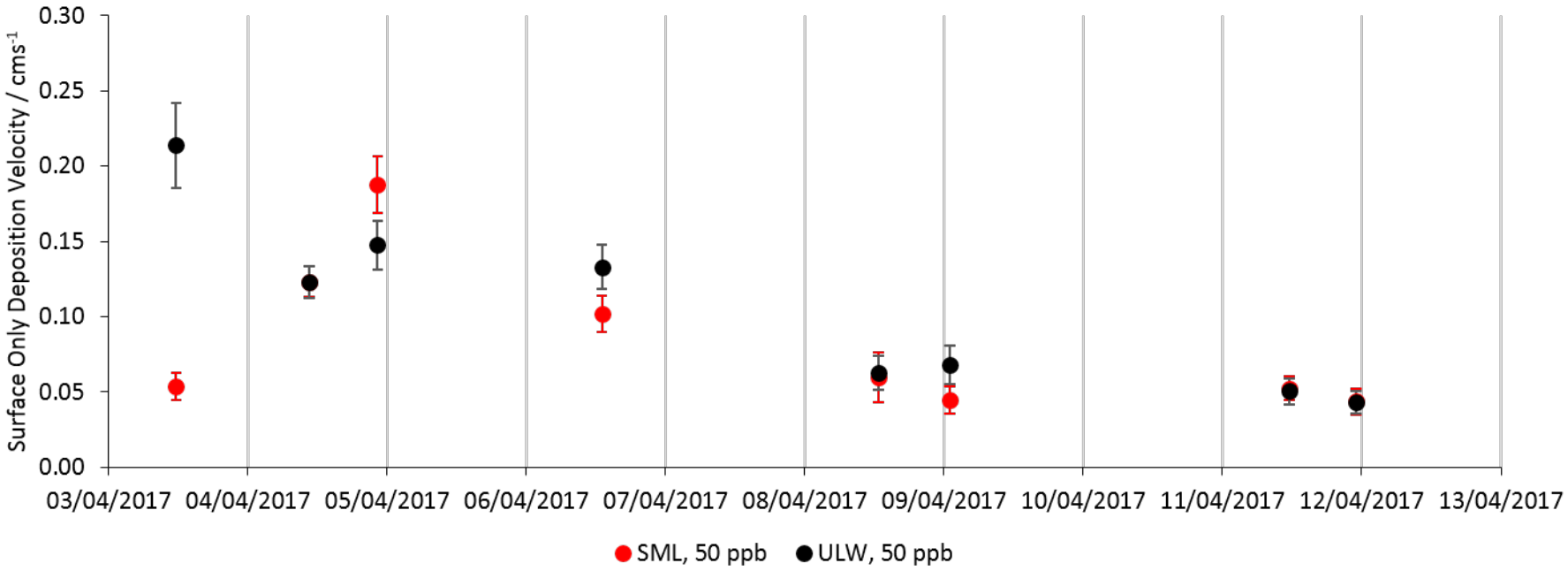

Figure 4.16: Surface only deposition velocity of ozone at 50 ppb ozone onto all the SML (red) and ULW (black) samples collected during the MILAN campaign. Error bars are calculated from the uncertainty in each average initial and final ozone measurement propagated forward

Figure 4.16 shows that the ratio of deposition between the SML and ULW is not consistent though for most sample pairs the deposition is roughly the same. This may not mean that the concentrations of reactive species within them are the same as the relative concentrations of iodide and organics may be changing with depth but in a way so as to compensate for one another. Apart from the initial SML reading which is surprisingly low, there appears to be a gradual drop-off in reactivity as the sampling period progresses. This could be due to increased biological activity as at the start of the sampling period the weather was very bright and calm which could have led to increased biogenic production of reactive materials.

4.9 Estimation of the contribution of inorganic iodine to ozone deposition in real seawater samples

SML and ULW samples for inorganic iodine analysis were frozen after filtering and stored at -18 oC. Prior to analysis samples were thawed overnight. Iodide concentrations were determined by square wave voltammetry.

Water samples were diluted in milli-Q water (50%) and an aliquot (12 mL) taken for analysis. To each sample, a solution of Triton X in milli-Q (0.2%, 90 μL) was added. The samples were purged with N_2 for 5 minutes prior to analysis to remove O_2. A square wave was applied to each sample from -0.1 V to -0.5 V with a step of -0.001 V at a frequency of 25 Hz. A series of standard additions were carried out with a solution of potassium iodide (1.3325×10^{-5} M, 20 μL, $\times 3$). Plotting the maximum current at each addition with the volume of standard added allows the concentration of iodide in the sample to be calculated by extrapolating the line of best fit as in figure 4.17.

Iodate concentrations were determined by spectrophotometry. In the presence of acid and iodide, iodate ions are converted into I_3^-, which absorbs light

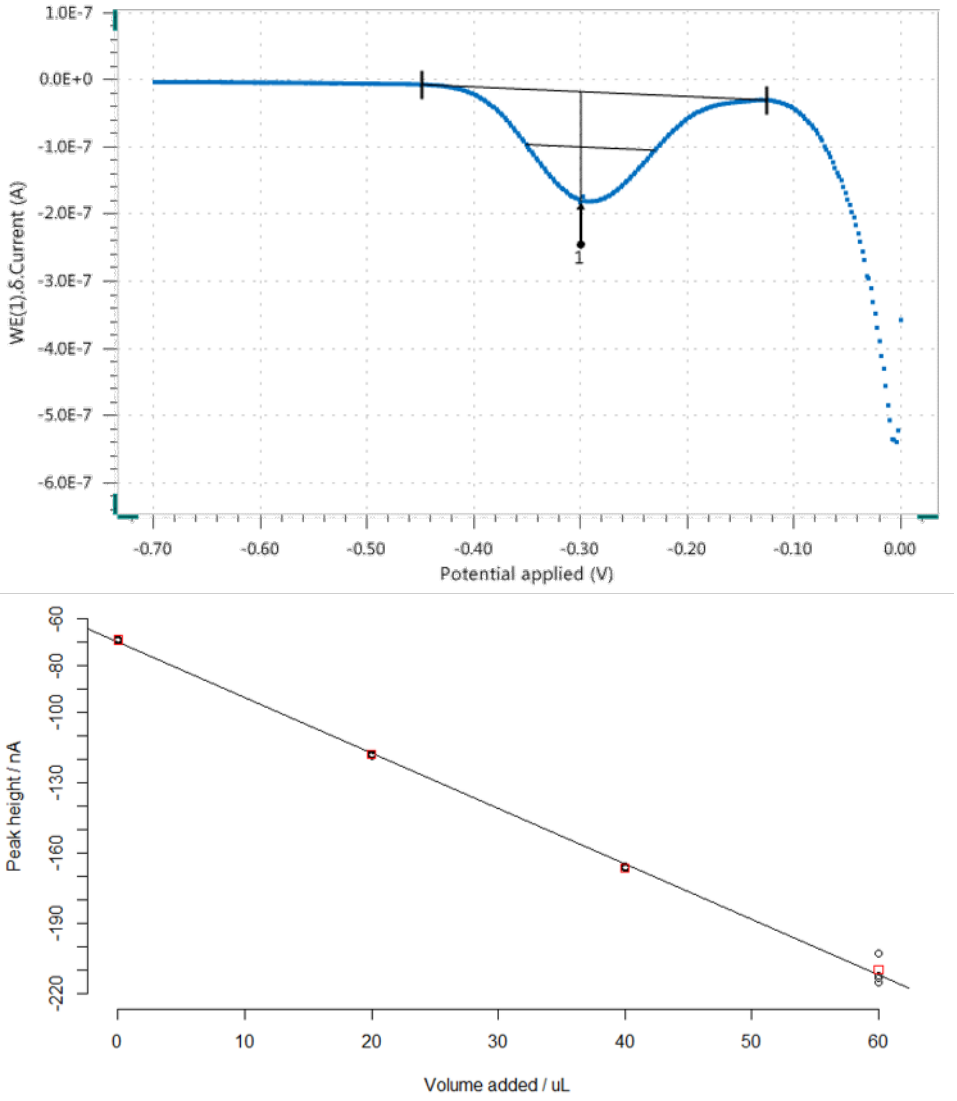

Figure 4.17: Example curve from square wave voltammetry showing the peak in applied potential due to iodide (top) and an example plot of peak height against standard addition (bottom)

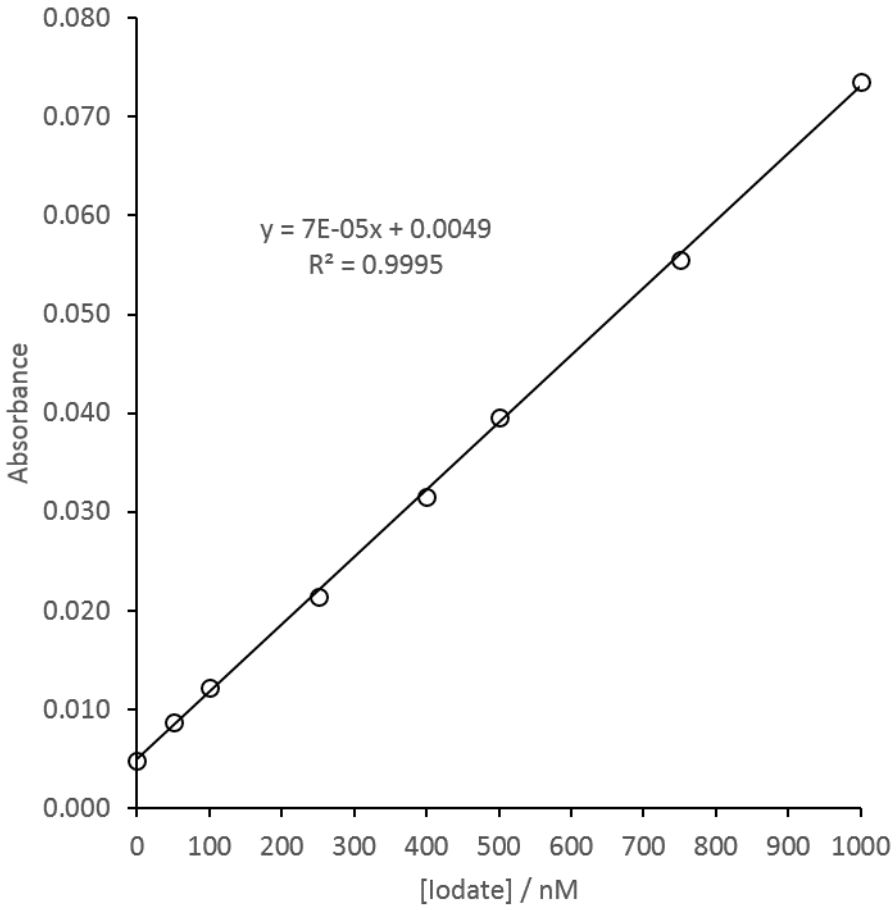

Figure 4.18: Example calibration curve of absorbance at 350 nm for different iodate standard solutions

in the UV region. To aliquots of sample or standard water (2.3 mL) a solution of sulfamic acid was added (50 μL) and the absorbance at 350 nm measured. A solution of iodide (150 μL) was then added and the absorbance measured again. Absorbance due to iodate was found by taking the difference of the two absorbances. At the start of each day of analysis, a calibration curve was produced with iodate standards at concentrations of 0 – 1000 nM. An example calibration curve is shown in figure 4.18.

Inorganic iodine concentrations measured in the samples collected during the MILAN campaign are shown in figure 4.19. These concentrations are in line with other measurements of inorganic iodine concentrations taken in the coastal North Sea. Data from Hou *et al.* is presented in figure 4.20 and a map of the sampling locations in figure 4.21. The depths of the samples are

unknown as the method used to collect them are not specified though they are quoted as being from "surface seawater", which is probably most comparable to the MILAN underlying water samples. Sample numbers 14, 16, 17, 18 and 25 were identified as being the most similar geographically to the MILAN samples.

It can be seen from figure 4.19 that there was little variation in the concentration of iodide and iodate with time of day or sampling date and no clear trends can be observed. From the map in figure 4.21 from Hou *et al.* it can be seen that sample numbers 19 and 20 were collected from estuarine or riverine environments respectively and the rest of the samples were collected from marine environments. The estuarine environment of sample 19 gave a similar iodide measurement but a low total inorganic iodine measurement compared to the marine samples and the riverine environment of sample 20 showed a very low total inorganic iodine measurement compared to the marine samples due to the reduced salt content of waters with more fresh water character. The values in figure 4.19 from the MILAN campaign are much more similar to the marine samples than the estuarine or riverine samples indicating that even though these samples were collected within a bay close to several large river mouths that the water being sampled was of marine nature.

Average values for iodide and iodate from the MILAN and Bridlington surface and subsurface samples and Hou *et al.*, 2007 are shown in figure 4.22. It can be seen that the measured errors for the MILAN and Bridlington samples are lower than those Hou *et al.*, which could be explained by the greater spatial variability in those samples. The reduction in the error of the Bridlington samples compared to MILAN is attributed to an optimisation of the experimental method between analyses. The MILAN samples show similar total inorganic iodide concentrations to those measured by Hou *et al.*, though the iodide concentrations are higher perhaps indicating a less oxidising environment. It can be seen in figures 4.19 and 4.22 that there is no significant enrichment of either iodide or iodate in the SML compared to the bulk underlying water, which is in agreement with previous measurements [14, 16].

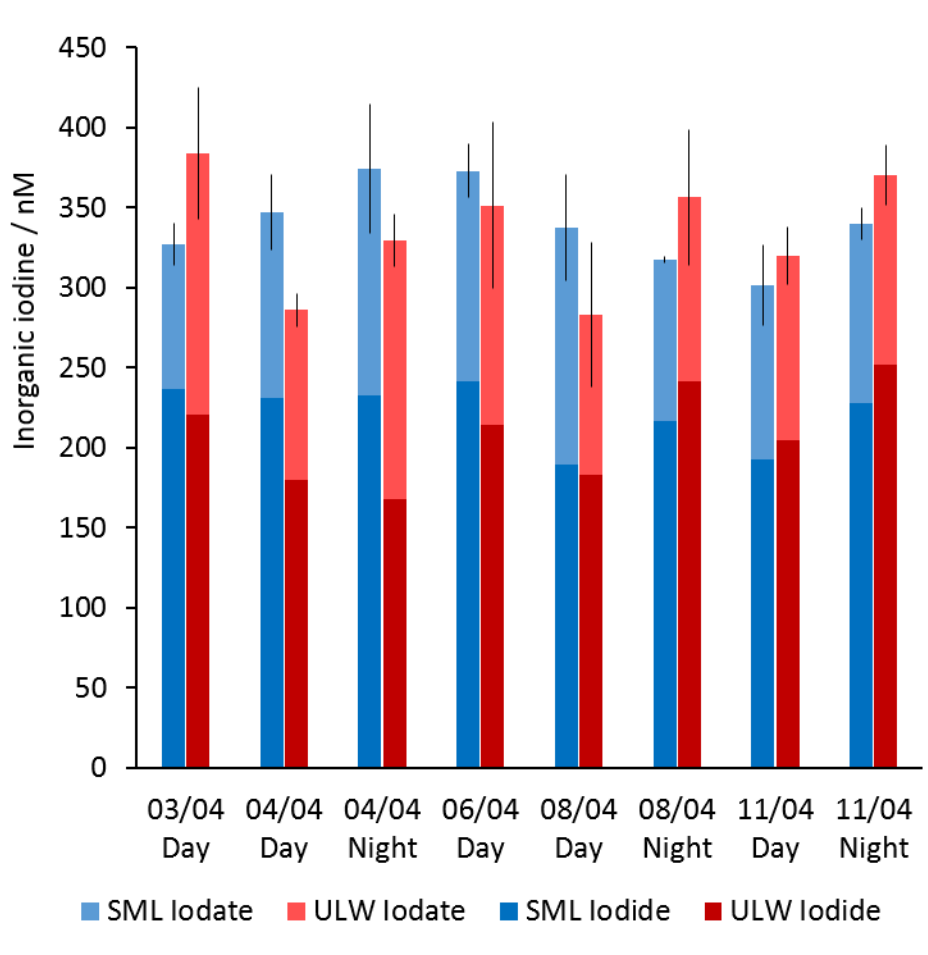

Figure 4.19: Iodide (bottom, dark bars) and iodate (top, lighter bars0 concentrations of surface (blue) and subsurface (red) water collected during the MILAN campaign

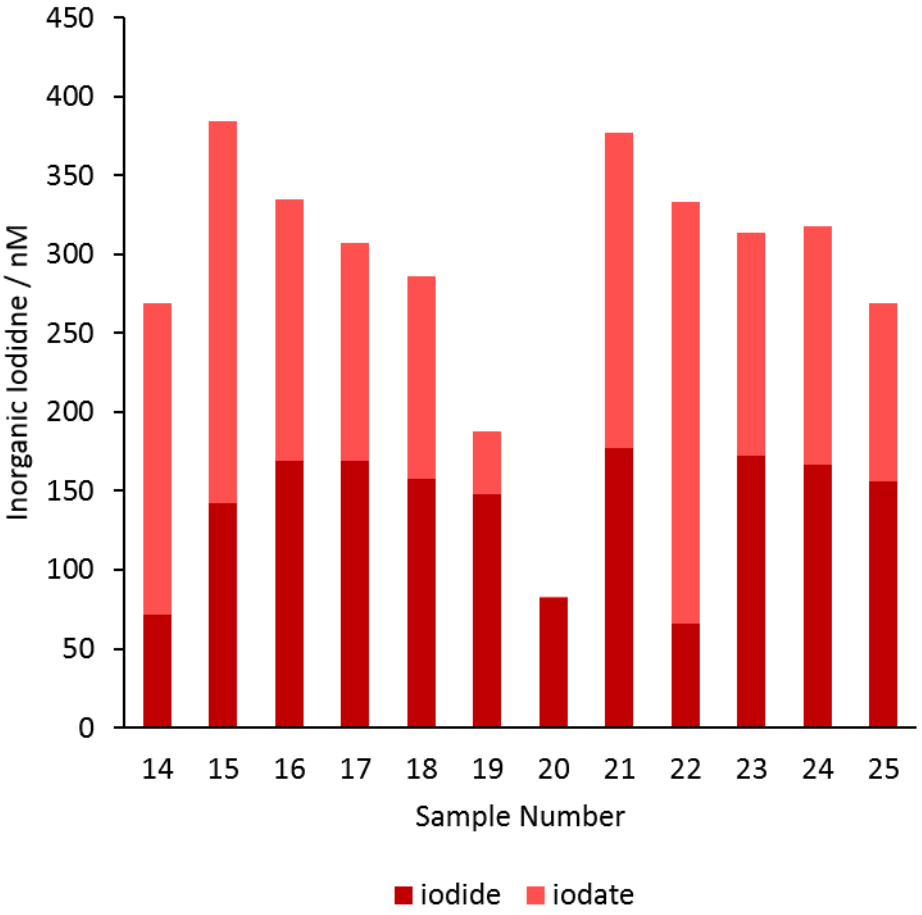

Figure 4.20: Iodide and iodate concentrations from coastal North Sea, data taken from Hou *et al.*, 2007 [51]

Using equation 4.2, resistance values for the deposition of ozone due to iodide for each sample could be estimated and from these surface deposition values could be calculated. Values for estimated surface deposition due to the reaction with iodide are shown in figure 4.23.

$$R = \frac{H}{\sqrt{k[\mathrm{I}-]D}} \tag{4.2}$$

Figure 4.21: Map of the North Sea showing where the seawater surface samples were obtained, reproduced from Hou *et al.*, 2007 [51]

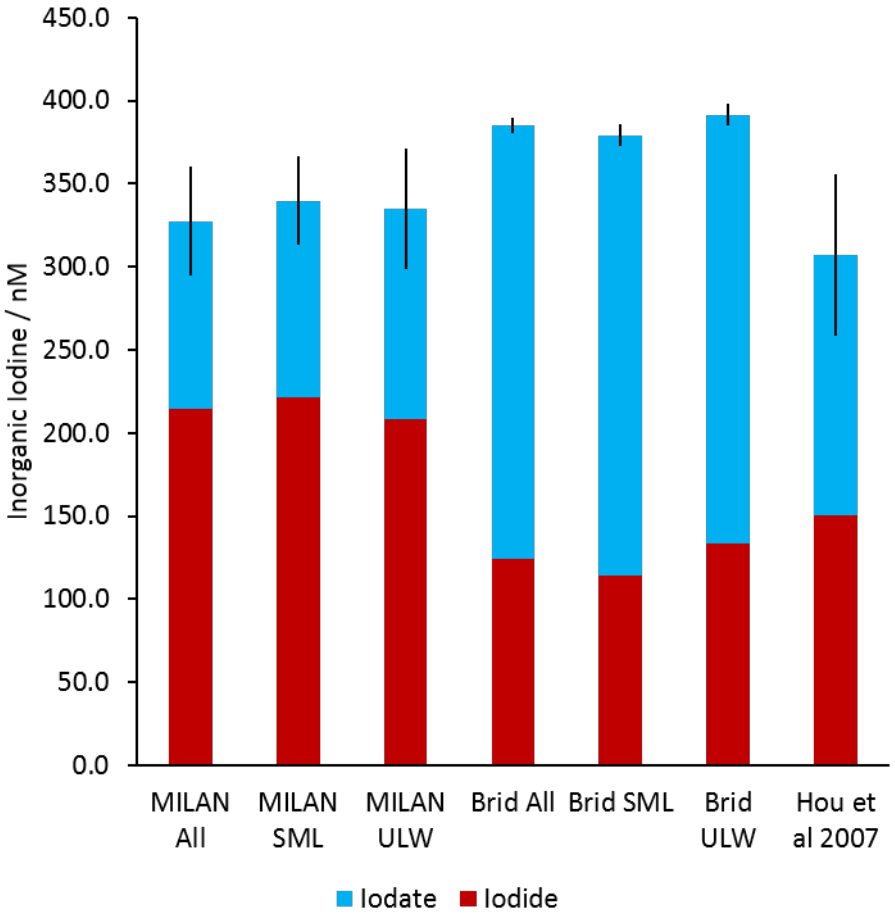

Figure 4.22: Average iodide (red) and iodate (blue) concentrations measured in SML and ULW samples collected from the North Sea. Error bars are one standard deviation of the mean

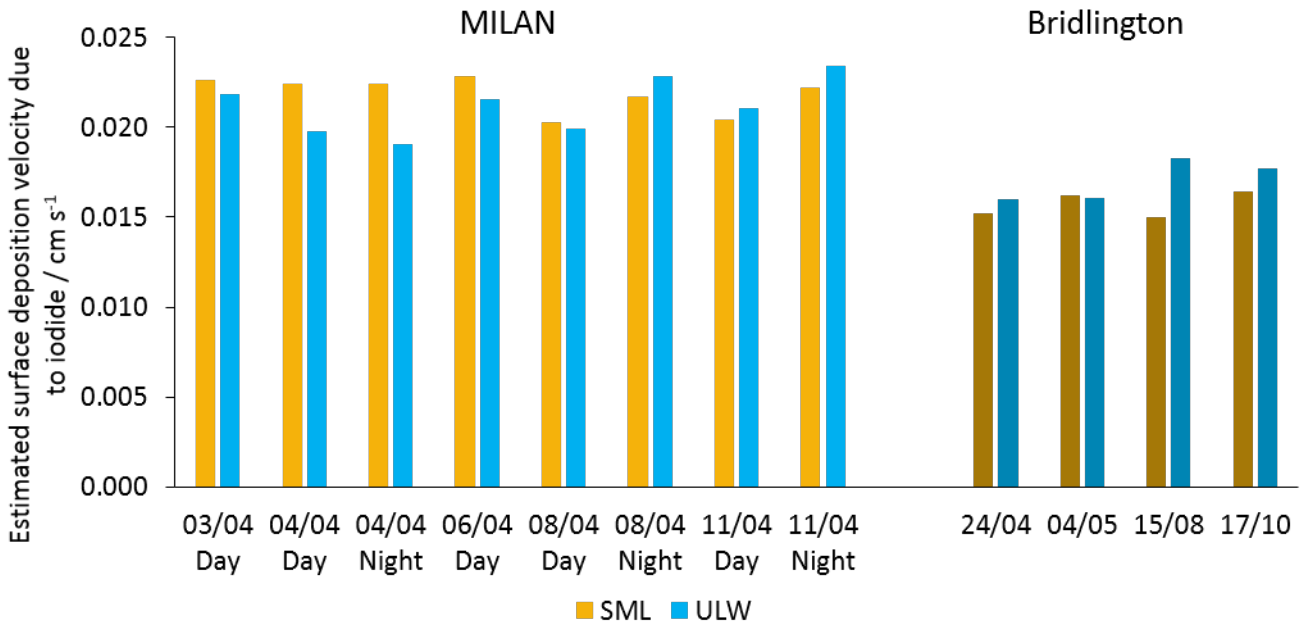

Figure 4.23: Estimated surface deposition velocity due to the reaction with iodide for SML and ULW samples collected during the MILAN campaign and off Bridlington

The total measured surface resistance ($R_{measured}$) can be expressed a function of the estimated resistance due to iodide (R_{iodide}) and some additional unknown resistance (R_x), equation 4.3. In the case of ozone deposition to the surface ocean, the unknown resistance is mostly due to the reaction with unsaturated organic material (R_o), with some small additional contributions from the reactions with bromide, chloride and other dissolved salts such as nitrate [12, 116]. Here it is assumed that the missing resistance is approximately equal to the resistance due to the reaction with organic material, equation 4.4. such that equation 4.3 becomes equation 4.5. Thus the organic only deposition velocity can be approximated using equation 4.6.

$$\frac{1}{R_{measured}} = f\left(\frac{1}{R_{iodide}}, \frac{1}{R_x}\right) \tag{4.3}$$

$$\frac{1}{R_x} \approx \frac{1}{R_o} \tag{4.4}$$

$$\frac{1}{R_{measured}} = \frac{1}{R_{iodide}} + \frac{1}{R_o} \tag{4.5}$$

$$v_{r,o} = \frac{1}{R_o} = \frac{1}{R_{measured}} - \frac{1}{R_{iodide}} \tag{4.6}$$

Using equations 4.2, 4.5 and 4.6, values for the deposition velocity of ozone due to the reaction with unsaturated organic molecules were calculated. Estimated organic contributions to measured surface deposition velocity at approximately 50 ppb ozone exposure for the MILAN samples are shown in figure 4.24 and those same organic contributions expressed as a percentage of the total measured surface only deposition velocity are shown in figure 4.25. Similar estimated organic contributions to measured surface deposition velocity at approximately 50 ppb ozone exposure for the Bridlington samples are shown in figure 4.26 and in figure 4.27.

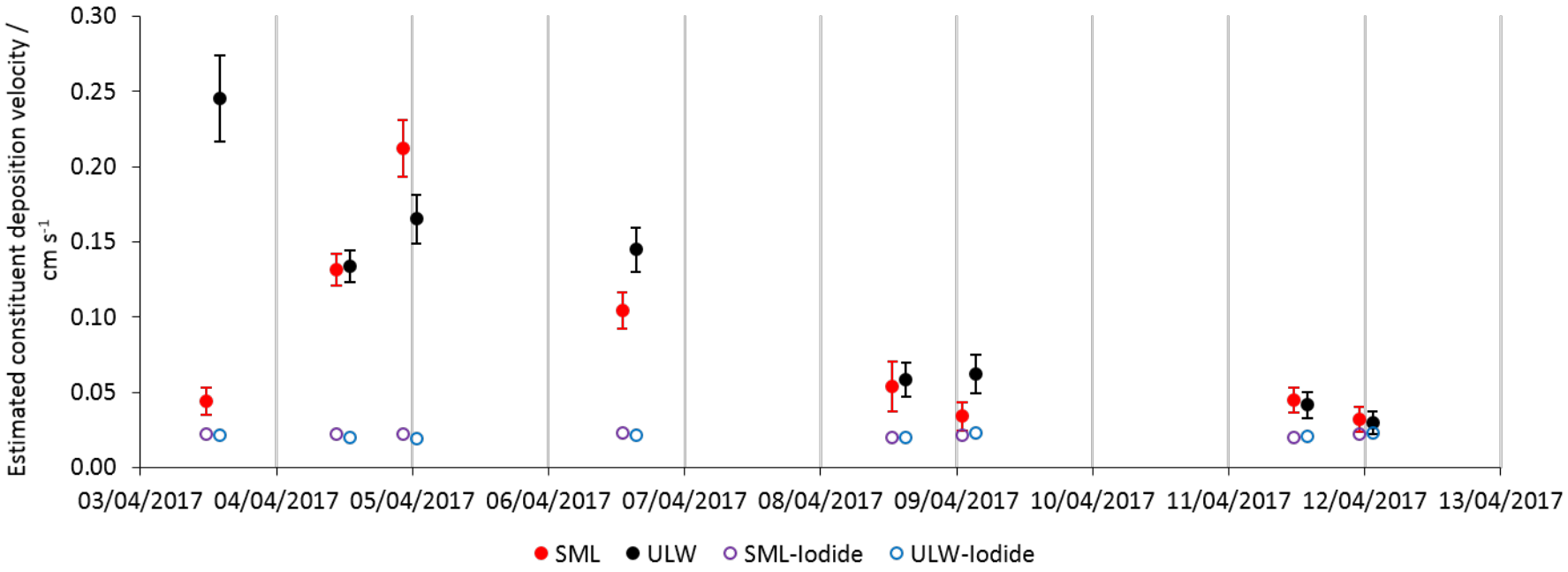

Figure 4.24: Estimated surface only deposition velocity at 50 ppb ozone exposure due to the reaction of ozone with organics for the SML and ULW samples collected on the MILAN campaign (solid circles). Also included for comparison are the corresponding estimated surface only deposition velocities due to the reaction with iodide (hollow circles)

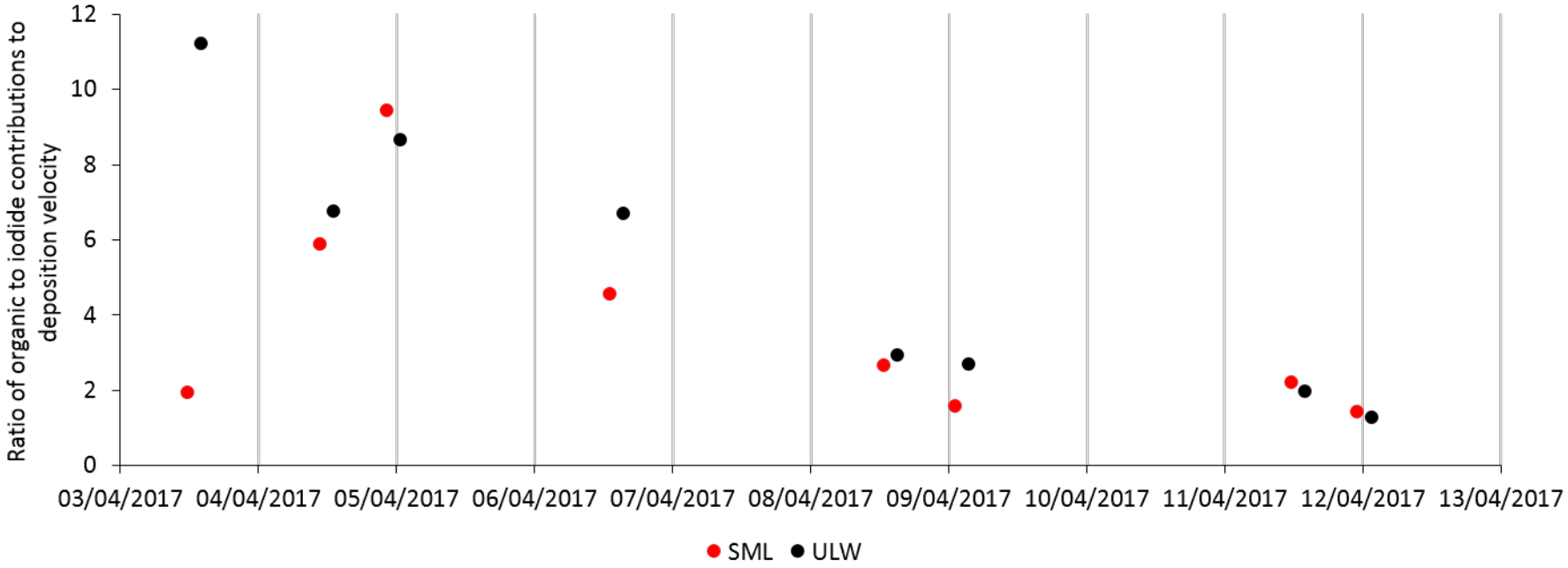

Figure 4.25: Ratio of estimated surface only deposition velocities for the reaction of ozone with organics to the reaction of ozone with iodide for the SML and ULW samples collected on the MILAN campaign at 50 ppb ozone exposure

It can be seen from figure 4.25 that the relative contribution of the reaction of ozone with unsaturated organic material for these samples is much higher than previously predicted [15, 21, 81, 106] shown by the ratios of organic to iodide surface only deposition velocity contributions being greater than one. The overall trends in figures 4.24 and 4.25 are very similar to those in figure 4.16 as the concentration of iodide was relatively stable during this period while the measured ozone deposition was much more varied. It can therefore be said that for the samples collected in the MILAN campaign, the unsaturated organic fraction is controlling the reactive ozone loss.

A similar trend can be observed for the samples collected off Bridlington in figures 4.26 and 4.27, though to a lesser degree. In all cases here the ratio of the organic to iodide surface only deposition velocities are greater than one indicating that the organic fraction is contributing more to the ozone loss for these coastal samples.

4.10 Relationships between ozone deposition and other measurements made during MILAN

The deposition of ozone due to the reactions with components other than iodide, which are assumed to be unsaturated organic molecules, were compared to the other metrics recorded during the MILAN campaign (table 4.5). Values for the gradient, m, intercept, c and R^2 of the lines of best fit for each correlation plot between estimated surface only deposition velocity and each other MILAN metric are shown in tables 4.6 and 4.7 for SML and ULW samples, respectively.

It can be seen from tables 4.6 and 4.7 that the largest R^2 values are from the correlation plots for unfiltered SML surfactant concentration, SML and ULW $PO_4{}^{3-}$ concentration and SML and ULW POC concentration. As previously mentioned, all samples were filtered prior to ozone deposition experiments so it

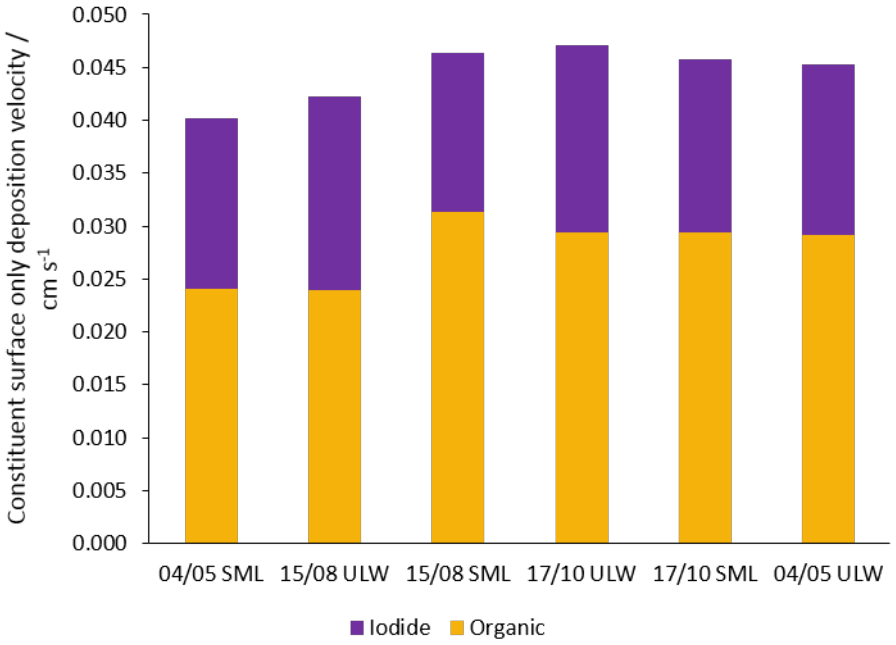

Figure 4.26: Estimated organic and iodide surface only deposition velocities at 50 ppb ozone exposure due to the reaction of ozone with unsaturated organics for the SML and ULW samples collected off Bridlington

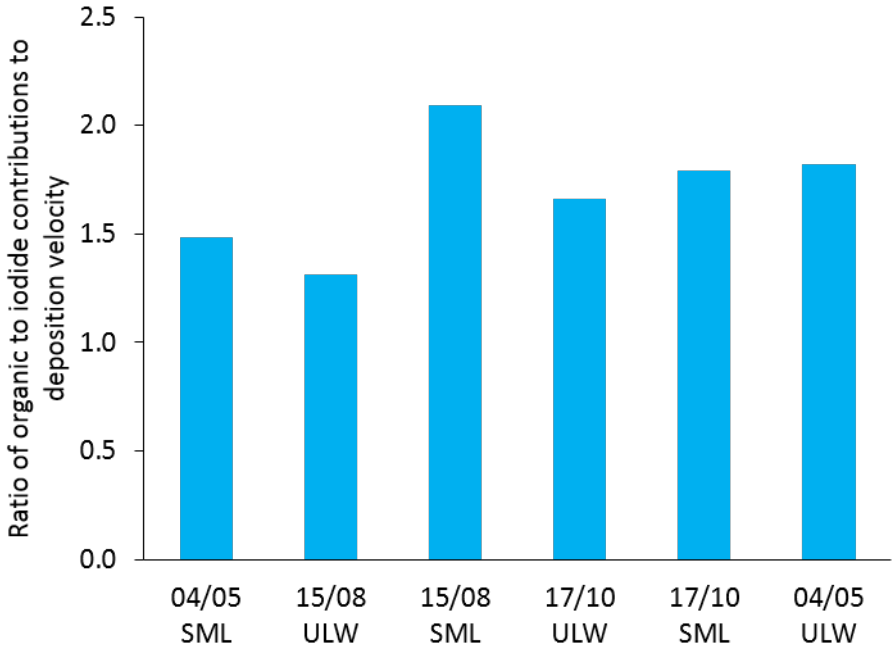

Figure 4.27: Ratio of estimated surface only deposition velocities for the reaction of ozone with unsaturated organics to the reaction of ozone with iodide for the SML and ULW samples collected off Bridlington at 50 ppb ozone exposure

Table 4.5: Metrics measured during the MILAN campaign. Measurements made *in situ* were made aboard the sampling catamaran or with a conductivity, temperature and depth rosette (CTD) and were thus not specific to SML or ULW samples

Metric	Details
Surface Tension	/ mN m^{-1}
pH	Measured *in situ*
Conductance	Measured *in situ* / μS cm^{-1}
Water temp	Measured *in situ* / ^{o}C
Average wind speed	Measured *in situ* / m s^{-1}
Max wind speed	Measured *in situ* / m s^{-1}
Air temperature	Measured *in situ* / ^{o}C
Solar radiation	Measured *in situ* / W m^{-2}
UV index	Measured *in situ*
CDOM	Absorbance at 355 nm / Au
Nitrate and nitrite	/ μg L^{-1}
silicate	/ μmol L^{-1}
PO_4^{3-}	/ μg L^{-1}
Unfiltered surfactant	SAS eq T-X-100 / mg L^{-1}
Filtered surfactant	SAS eq T-X-100 / mg L^{-1}
DOC	/ mg L^{-1}
POC	/ mg L^{-1}
FDOM	Humification index
Lipids	Total dissolved lipids / μg L^{-1}

Table 4.6: Values for the gradients, intercepts and R^2 for the correlation plots of non-iodide surface only deposition velocity and other metrics for SML samples collected during MILAN

Metric	m	c	R^2
Surface Tension	1.2129	75.021	0.3794
pH	0.2740	7.9313	0.3659
Conductance	15612	32117	0.2708
Water temp	-6.7781	10.625	0.2773
Average wind speed	11.534	4.3972	0.0175
Max wind speed	11.151	5.5086	0.0127
Air temperature	-1.5940	9.6076	0.0261
Solar radiation	908.56	65.183	0.0707
UV index	5.6064	0.3757	0.0745
CDOM	-0.3309	2.6676	0.1719
Nitrate and nitrite	-1676.3	1994.0	0.4978
silicate	-1308.9	753.03	0.2025
PO_4^{3-}	-278.61	122.23	0.8347
Unfiltered surfactant	-0.1913	0.2176	0.9553
Filtered surfactant	-0.2407	0.2257	0.6140
DOC	-1.1835	2.9087	0.2054
POC	5.3315	0.3341	0.7216
FDOM	-25.267	10.506	0.4555
Lipids	64.638	58.057	0.0922

Table 4.7: Values for the gradients, intercepts and R^2 for the correlation plots of non-iodide surface only deposition velocity and other metrics for ULW samples collected during MILAN

Metric	m	c	R^2
Surface Tension	-0.6982	75.193	0.2473
pH	-0.1235	7.9674	0.1030
Conductance	7057.0	32624	0.0767
Water temp	5.1653	9.4981	0.2231
Average wind speed	10.273	4.1279	0.0146
Max wind speed	14.994	4.5648	0.0242
Air temperature	-1.3046	9.5857	0.0110
Solar radiation	1968.9	-43.842	0.2096
UV index	12.530	-0.3348	0.2351
CDOM	0.1603	2.6117	0.1006
Nitrate and nitrite	-866.10	1960.2	0.0678
silicate	-540.82	652.99	0.0718
PO_4^{3-}	-337.66	124.41	0.5195
Unfiltered surfactant	0.0624	0.1821	0.0221
Filtered surfactant	0.1146	0.1776	0.0656
DOC	1.7374	2.7099	0.0754
POC	4.2089	0.05557	0.6509
FDOM	-51.546	14.115	0.9317
Lipids	20.979	67.326	0.0071

is an unexpected result that the highest correlation would be observed between an unfiltered measurement of SML surfactant concentration, particularly as the trendline for the correlation of the filtered surfactant samples is significantly lower. No such relationship was observed for the ULW samples, which is not because the concentration of surfactants were significantly different between these samples (average unfiltered surfactant concentration = 0.199 ± 0.01 mg L^{-1} and 0.190 ± 0.03 mg L^{-1} for all SML and ULW samples respectively).

The relatively strong positive correlation between ozone deposition and the concentration of particulate organics was unexpected for a similar reason; most of this material would have been filtered out of the sample prior to ozonolysis. It is possible that the POC fraction of these samples contains more reactive material towards ozone and that not all of this material is being filtered out. It was noted during MILAN that the surface waters were very turbid and as such more particulate matter may have been pulled through the filter by the vacuum pump.

The effect of phosphate ions on the aqueous phase chemistry of ozone has been reported by Morozov and Ershov [96]. Here it was found that phosphate was able to accept hydroxyl radicals that would otherwise catalytically react in the decomposition of dissolved ozone in pure water, reducing the rate of ozone loss. It is not known the extent to which phosphate interacts with other reactive processes that destroy aqueous ozone in seawater, but it was observed in this work that increasing phosphate concentrations reduced the non-iodide deposition velocity of ozone with an R^2 value of 0.8347 in the SML and 0.5195 in the ULW.

No correlation was observed with surface tension, chromophoric dissolved organic matter (CDOM), dissolved organic carbon (DOC) or lipid concentration, which suggest that either these metrics are measuring changes in ozone-inert substances such as saturated organic compounds or that the relationships between the compounds that control ozone deposition and these metrics are not simple or linear.

4.11 Conclusions

Sea surface microlayer samples were collected during the MILAN campaign in May 2017 by the rotating disk method and off Bridlington in May, August and October 2018 by Garrett Screen. The reactivity of these samples to ozone was measured and compared to that of corresponding samples of underlying, bulk water. Due to limitations in sample transport and storage, only one replicate was carried out of the ozone deposition profiles for the samples collected during MILAN. More material was collected and stored from the Bridlington sampling expeditions enabling more repeats of ozone deposition experiments. There was reasonably good reproducability of the method across three repeats of the Bridlington samples with the exception of one repeat that did not show any change in ozone deposition velocity with changing ozone exposure (figure 4.6).

Ozone deposition profiles for all SML and ULW samples indicated that the dominant mechanism for reactive ozone loss was the Langmuir - Hinshelwood surface reaction mechanism, as is typical of organic surfaces, though some samples did exhibit much flatter profiles suggesting that the contribution of bulk phase chemistry was also significant, particularly in the latter half of the MILAN campaign.

The relative reactivity of SML samples compared to the underlying water was not consistent during the MILAN campaign, though the underlying water was in most cases at least as reactive to ozone than the SML. This was attributed to the highly turbid water of the Jade Bay, where these samples were collected, containing higher than normal concentrations of organic material.

The relative contributions to reactive ozone loss onto SML and ULW samples by the reactions of ozone with dissolved iodide and unsaturated organics were estimated and compared. The largest contribution for all samples was found to be from the assumed reaction with organics which contributed between 1.3 and 2.1 times as much as iodide for the Bridlington samples and between 1.3 and 11.2 times as much as iodide for the MILAN samples. This is more than previously estimated in the literature, where the contri-

butions of iodide and organics have been said to be, at most, approximately equal [15, 21, 81, 106]. A potential reason for this difference with the previous literature estimates is that none of these examples used real surface seawater, in all cases the experiments were purely lab based using synthetic seawaters with assumed natural level concentrations of reactants. Additionally, these studies used various organic material such as riverine DOM, chlorophyll and nonanoic acid to mimic the organic material found in the surface ocean which may show very different reactivities to the real thing.

The correlations between the estimated organic deposition velocity and other physical and chemical metrics measured during the MILAN campaign have been measured. Overall, low R^2 values for correlation plots indicate that the relationships between deposition velocity and these other metrics are neither simple nor linear, which is not surprising as many separate factors will influence the reactivity of the ocean surface towards ozone. To gain a better understanding of the influences of these various metrics, much more regular measurements of each must be made and then the relative contributions might be compared. In reality this would not be possible as the MILAN campaign was attended by scientists from across the world with very varied expertise and so conducting all of those analyses regularly would be very challenging.

Chapter 5

Conclusions and discussions on further studies

5.1 Conclusions

5.1.1 Summary

This thesis has investigated the dry deposition of ozone at the ocean surface through the parallel reactive pathways that are the reaction of gas phase ozone and dissolved iodide and the reaction of gas phase ozone with surface organic matter.

In chapter 2, the second order heterogeneous rate of reaction between ozone and iodide was measured at 298 K using custom built apparatus under multiple sets of experimental conditions, equalling the total number of measurements reported at this temperature in the literature.

In chapter 3, the deposition of ozone onto synthetic seawater samples was measured and the relative reactivities of multiple unsaturated organic compounds and dissolved iodide compared experimentally.

In chapter 4, the dry deposition of ozone onto samples of real seawater, both surface and subsurface, was measured. Using the results from chapter 2 and directly measured iodide concentrations, the resistances to ozone deposition due to the reaction with iodide for each real seawater sample were estimated and compared to the measured deposition to estimate the difference between them.

5.1.2 Design and optimisation of a flow reactor for kinetic studies

A flow reactor was designed to measure the second order heterogeneous rate of reaction between gas phase ozone and dissolved iodide. As this reaction occurs on a faster timescale than could be measured by the detection method (due to large instrument response times and dead volumes in the setup), the reactor was designed to simulate different ozone exposure times to the reactive

surface with a movable injector line. Exposure time was dependant on the diameter of the tube, position of the inlet line within the tube and the flow conditions of gases into the reactor.

The flow conditions were optimised to minimise the contribution of gas phase diffusion (aerodynamic resistance) to the total measured resistance. A total of 15 flow conditions were tested with different combinations of ozone flow rate, carrier gas flow rate and inlet line shape; a reduction in aerodynamic resistance of ≈41% was achieved from the initial value (initial $R_a = 4.09$ cm^{-1} s, lowest $R_a = 2.41$ cm^{-1} s).

A second series of optimisation experiments were carried out under three sets of flow conditions (ozone flow + carrier flow = 2000 sccm) to directly measure the diffusion profile around the inlet in the reactor. The criteria for successful conditions were firstly, a steady mixing ratio of ozone between the end of the inlet and the reactor outlet and secondly, a steady mixing ratio reading of zero behind the end of the inlet line.

It was found that the conditions with the highest proportion of carrier flow (O_3:Carrier = 1:4) did not give a stable reading between the inlet and outlet as there was too much carrier flow pushing the ozone through the tube without fully mixing and therefore not satisfying criterion one. The opposite flow conditions (O_3:Carrier = 4:1) gave the largest observed signal behind the inlet line indicating that the carrier flow was not sufficient to mix with the ozone from the end of the inlet line and push the flows through the reactor and therefore not satisfying criterion two. Equal ratio flows (O_3:Carrier = 1:1) gave results in the 'Goldilocks zone' with a small amount of retro-diffusion, well mixed gases after the inlet and also a low aerodynamic resistance. The effect of changing the ozone mixing ratio over the range of $56 - 258$ ppb was found to have no effect on the degree of retro-diffusion observed.

5.1.3 Direct measurement of the second order rate constant between ozone and iodide

Three sets of flow conditions were used to measure the second order rate constant for ozone and iodide at 293 K. Values for $k_{O_3+I^-}$ showed a high error and variability, with a factor of 2.4 separating the highest and lowest measured values(1.79 ± 0.32 and 4.31 ± 0.39 × 10^9 M^{-1} s^{-1}). While the spread was high, it was not more so than had previously been reported in the literature at similar temperatures by Magi *et al.* (2.40 ± 1.30 × 10^9 M^{-1} s^{-1}) [79], Shaw and Carpenter [120] (1.40 ± 0.20 × 10^9 M^{-1} s^{-1}) and Rouvière *et al.* (1.0 ± 0.3 × 10^9 M^{-1} s^{-1}) [111].

5.1.4 Measurement of ozone dry deposition onto unsaturated organic molecules

A flask reactor was used to measure the ozone deposition onto synthetic seawater solutions containing one of four fatty acid molecules, nonanoic, oleic, linoleic and linolenic acids. Apparent Langmuir-Hinshelwood (LH) behaviour was observed for all four acids, including nonanoic acid which was hypothesised to be unreactive to ozone, though this could have been an artefact of the method. It was found that increasing the number of double bonds within the fatty acid molecule leads to a higher level of ozone deposition which agreed with previous measurements of the same fatty acids by Thornberry *et al.* [131].

A theoretical fit was calculated for the uptake of ozone by oleic acid with changing ozone exposure based on the kinetics of the LH surface reaction. The fit gave a low R^2 (0.795) suggesting that the deposition may not be fully described by LH kinetics. The gradient of the fitted curve was found to be shallower than that of the reported data indicating a potential bias toward overestimation of ozone deposition at low ozone exposure ($O_3 < 20$ ppb) which could be due to a similar error as observed for nonanoic acid.

5.1.5 Measurement of ozone dry deposition onto North Sea samples of sea surface microlayer and underlying water

SML and ULW samples were collected from the North Sea during the MILAN campaign of 2017 in Wilhelmshaven, Germany and on three more occasions near Bridlington, England in 2018. Ozone deposition experiments were carried out in the same way as for the synthetic seawater described previously. All ozone deposition profiles suggested that the dominant mechanism of ozone loss was the LH surface reaction as would be expected of the reaction between ozone and organic molecules.

The deposition of ozone onto ULW samples was found to be at least as high as that of the SML samples suggesting that the coastal water sampled in each case had similar reactive species throughout the top meter of the water column. A negative correlation was observed between phosphate concentration and ozone deposition, which may indicate that phosphate inhibits ozone loss in the surface ocean as has been previously observed for ozone loss in pure water [96]. Ozone deposition also showed correlations with the surfactant concentrations of unfiltered SML and concentrations of particulate organic material. This was unexpected as both classes of material would be removed from the samples during filtering, which occurred for all MILAN samples prior to exposure to ozone. None of the measured metrics could be used to parameterise ozone deposition alone, though a more complex relationship that could not be observed here may exist between multiple metrics.

5.1.6 Comparison of the relative contributions of DOM and iodide to reactive ozone loss at the ocean surface

The reactivities of iodide and organic matter were compared for synthetic seawater samples and for real SML and ULW. Ozone deposition was measured

onto a synthetic seawater solution containing both iodide and oleic acid and compared to the depositions onto the individual components. It was shown that the deposition onto the solution of both oleic acid and iodide was larger than either individual deposition though less than the direct sum of the two. As the deposition due to iodide occurs via a bulk mechanism that is independent of ozone exposure and the deposition due to oleic acid occurs via the ozone dependant LH surface mechanism the contribution of either constituent to the total deposition will be dependant on ozone exposure. At atmospherically relevant ozone mixing ratios, the deposition due to oleic acid is much greater than that of iodide, for example at 27 ppb ozone the ozone uptake coefficients onto oleic acid, iodide and the combination were 1.02, 0.41 and 1.22×10^{-4}, respectively.

Iodide concentrations were measured for all SML and ULW samples and ozone deposition velocities estimated using the rates of reaction calcuated in chapter 2. For the MILAN samples, the deposition due to iodide accounted for between 8% and 43% of the total measured deposition at 50 ppb ozone reflecting the differences in total deposition as iodide concentrations remained fairly constant. For the Bridlington samples, the deposition due to iodide had a greater and more constant contribution, accounting for between 32% and 43% of total measured deposition. These values suggest that deposition is often dominated by processes other than the reaction with iodide. As the LH surface mechanism is evident from the ozone dependence of deposition velocity, surface chemistry is likely a candidate for the missing source of deposition.

Most estimates of the relative contributions of I^- and DOM to marine ozone deposition in the literature have suggested that the effects of DOM is at most equal in magnitude to that of I^-; the results obtained here indicate that the contribution of DOM could be far greater than previously reported [81, 116].

5.2 Discussion of further studies

In all of the literature, the only study to investigate the effect of temperature on the second order rate constant for ozone and iodide was conducted in 1997 by Magi *et al.* [79]. Other values reported at individual temperatures (such as those reported by Liu *et al.* [77] and Hu *et al.* [52]) do not appear to follow the same trend as observed in that work. The values reported here show agreement with the values reported by Magi *et al.* at 293 K, and so there is the opportunity to conduct a similar temperature dependant study using the flow reactor developed in this work to further verify Magi *et al.*'s results.

The flow reactor was found to be unsuitable for the measurement of ozone deposition onto organic films as the surface was too long and narrow for the fatty acids to spread evenly upon them. This may be alleviated using a flow reactor design with a wider or shorter tube so that the surface area of the reactive sample would be more square. In order to gain useful information about the change in ozone deposition with changing exposure time, any new reactor must be carefully designed so that multiple positions may be monitored over the surface, each giving significantly different ozone readings (i.e. such that ΔO_3 between two positions is greater than the noise of the ozone instrument).

Further comparisons could be made for the reaction between ozone and marine DOM with the literature by expanding the range of organic molecules tested to include some of those reported in previous works (such as chlorophyll [21, 106]). In addition, several studies have reported on the significant influence of photochemistry in marine ozone dry deposition [20, 106]. By conducting similar experiments to those presented in this work in dark and light environments, an extra layer of depth could be added to the understanding of ozone dry deposition.

Measurements of ozone deposition onto real seawater samples are scarce in the literature, and as such the measurements here make a significant contribution to the total pool of measurements in this field. To improve upon the work presented here, more repeats of ozone deposition onto more samples

should be made whilst endeavouring to measure as many additional metrics as is feasible. It may then be possible to parameterise ozone deposition in terms of more readily available measurements of marine properties such as latitude, water temperature, salinity, etc. This could then be employed in atmospheric models to better capture the complex and diverse range of values reported for marine ozone deposition.

5.3 Final Thoughts

For those hoping to effectively model atmospheric ozone, an understanding of the reactive dry deposition pathways at the ocean surface is key. The uncertainties in these processes are large, and can only be reduced by additional measurements on both real seawater and simplified laboratory systems.

When considering the reactive pathways for ozone dry deposition in the marine environment, the organic fraction of the SML cannot be ignored. For future work, particular effort should be made to measure both the organic and inorganic composition of this layer. Only by comparing reactive ozone loss to such chemical compositions can a parameter based relationship be incorporated into atmospheric models.

List of Abbreviations

γ_{eff}	Uptake coefficient
BrFa	Branched fatty acid
CDOM	Coloured dissolved organic matter
CTD	Conductivity, temperature and depth rosette
DMS	Dimethyl sulfide
DOC	Dissolved organic carbon
DOM	Dissolved organic matter
ER	Eley - Rideal
FA	Fatty acid
FDOM	Fluorescent dissolved organic matter
I^-	Iodide
IR	Infrared
LH	Langmuir - Hinshelwood
MILAN	Microlayer at night
MUFA	Monounsaturated fatty acid
O_3	Ozone
OOTF	Organised organic thin film
PO_4^{3-}	Phosphate
POC	Particulate organic matter
POM	Particulate organic carbon
PUFA	Polyunsaturated fatty acid
R_a	Aerodynamic resistance
R_s	Surface resistance
RTD	Retro-diffusive distance

S^3	Sea surface scanner
SAFA	Saturated fatty acid
SML	Sea surface microlayer
STE	Stratosphere-troposphere exchange
ULW	Underlying water
UV	Ultra-violet
v_d	Deposition velocity

Bibliography

[1] *Estimation Programs Interface Suite™ for Microsoft Windows*. United States Environmental Protection Agency, Washington, DC, USA, 2019.

[2] Aldaz, L. Flux Measurements of Atmospheric Ozone over Land and Water. *Journal of Geophysical Research 74*, 28 (1969), 6943–6946.

[3] Aller, J. Y., Radway, J. A. C., Kilthau, W. P., Bothe, D. W., Wilson, T. W., Vaillancourt, R. D., Quinn, P. K., Coffman, D. J., Murray, B. J., and Knopf, D. A. Size-resolved characterization of the polysaccharidic and proteinaceous components of sea spray aerosol. *Atmospheric Environment 154* (2017), 331–347.

[4] Aminot, Y., Belles, A., Alary, C., and Readman, J. W. Near-surface distribution of pollutants in coastal waters as assessed by novel polyethylene passive samplers. *Marine Pollution Bulletin 119*, 1 (2017), 92–101.

[5] Bariteau, L., Helmig, D., Fairall, C. W., Hare, J. E., Hueber, J., and Lang, E. K. Determination of oceanic ozone deposition by ship-borne eddy covariance flux measurements. *Atmospheric Measurement Techniques 3*, 2 (2010), 441–455.

[6] Beltran, F. J. *Ozone Reaction Kinetics for Water and Wastewater Systems*, 1st ed. CRC Press, Boca Raton, FL, USA, 2003.

[7] Bińk, A. K. Ozone Solubility in Liquids. *Ozone: Science & Engineering 28*, 2 (2006), 67–75.

[8] Bosac, C., Black, V. J., Roberts, J. A., and Black, C. R. Impact of ozone on seed yield and quality and seedling vigour in oilseed rape (Brassica napus L.). *Journal of Plant Physiology 153*, 1-2 (1998), 127–134.

[9] Calace, N., Catrambone, T., Petronio, B. M., and Pietroletti, M. Fulvic acid in microlayer waters of the Gerlache Inlet Sea (Antarctica): Their distribution in dissolved and particulate phases. *Water Research 41*, 1 (2007), 152–158.

[10] Carlson, D. J. A field evaluation of plate and screen microlayer sampling techniques. *Marine Chemistry 11*, 3 (1982), 189–208.

[11] Carlson, D. J., Cantey, J. L., and Cullen, J. J. Description of and results from a new surface microlayer sampling device. *Deep Sea Research Part A. Oceanographic Research Papers 35*, 7 (7 1988), 1205–1213.

[12] Carpenter, L. J., MacDonald, S. M., Shaw, M. D., Kumar, R., Saunders, R. W., Parthipan, R., Wilson, J., and Plane, J. M. Atmospheric iodine levels influenced by sea surface emissions of inorganic iodine. *Nature Geoscience 6*, 2 (2013), 108–111.

[13] Carpenter, L. J., and Nightingale, P. D. Chemistry and Release of Gases from the Surface Ocean. *Chemical Reviews 115*, 10 (5 2015), 4015–4034.

[14] Chance, R., Baker, A. R., Carpenter, L. J., and Jickells, T. D. The distribution of iodide at the sea surface. *Environmental Science: Processes & Impacts 16*, 8 (2014), 1841–1859.

[15] Chang, W., Heikes, B. G., and Lee, M. Ozone deposition to the sea surface: Chemical enhancement and wind speed dependence. *Atmospheric Environment 38*, 7 (2004), 1053–1059.

[16] Chapman, P., and Liss, P. S. The sea surface microlayer: measurements of dissolved iodine species and nutrients in coastal waters. *Limnology and Oceanography 26*, 2 (1981), 387–390.

[17] Chiu, R., Tinel, L., Gonzalez, L., Ciuraru, R., Bernard, F., George, C., and Volkamer, R. UV Photochemistry of Carboxylic Acids at the Air-Sea Boundary: A Relevant Source of Glyoxal and other OVOC in the Marine Atmosphere. *Geophysical Research Letters* (2016), 1079–1087.

[18] Christiansen, B. O. Radiative forcing and climate sensitivity: The ozone experience. *Quarterly Journal of the Royal Meteorological Society 125*, April 1998 (1999), 3011–3035.

[19] Cincinelli, A., Stortini, A. M., Pergini, M., Checchini, L., and Lepri, L. Organic pollutants in sea-surface mycrolayer and aerosol in the coastal environment of Leghorn - Tyrrhenian Sea. *Marine Chemistry 76*, 1-2 (2001), 77–98.

[20] Ciuraru, R., Fine, L., van Pinxteren, M., D'Anna, B., Herrmann, H., and George, C. Photosensitized production of functionalized and unsaturated organic compounds at the air-sea interface. *Scientific Reports 5*, August (2015), 12741.

[21] Clifford, D., Donaldson, D. J., Brigante, M., D'Anna, B., and George, C. Reactive uptake of ozone by chlorophyll at aqueous surfaces. *Environmental Science and Technology 42*, 4 (2008), 1138–1143.

[22] Criegee, R. Mechanism of Ozonolysis. *Angewandte Chemie International Edition in English 14*, 11 (1975), 745–752.

[23] Cunliffe, M., and Wurl, O. *Guide to best practices to study the ocean's surfaces*. Marine Biological Association of the United Kingdom for SCOR, Plymouth, UK, 2014.

[24] de Gouw, J. A., and Lovejoy, E. R. Reactive uptake of ozone by liquid organic compounds. *Geophysical Research Letters 25*, 6 (1998), 931–934.

[25] Emberson, L. D., Pleijel, H., Ainsworth, E. A., van den Berg, M., Ren, W., Osborne, S., Mills, G., Pandey, D., Dentener, F., Büker, P., Ewert, F., Koeble, R., and Van Dingenen, R. Ozone effects on crops and consideration in crop models. *European Journal of Agronomy 100*, May (2018), 19–34.

[26] Falkowska, L. Sea surface microlayer: A field evaluation of teflon plate, glass plate and screen sampling techniques. Part 1. Thickness of microlayer samples and relation to wind speed. *Oceanologia 41*, 2 (1999), 211–221.

[27] Fouke, J. M., Delemos, R. A., and McFadden, E. R. Airway response to ultra short-term exposure to ozone. *The American Review of Respiratory Disease 137*, 2 (1988), 326–330.

[28] Fowler, D., Pilegaard, K., Sutton, M. A., Ambus, P., Raivonen, M., Duyzer, J., Simpson, D., Fagerli, H., Fuzzi, S., Schjoerring, J. K., Granier, C., Neftel, A., Isaksen, I. S., Laj, P., Maione, M., Monks, P. S., Burkhardt, J., Daemmgen, U., Neirynck, J., Personne, E., Wichink-Kruit, R., Butterbach-Bahl, K., Flechard, C., Tuovinen, J. P., Coyle, M., Gerosa, G., Loubet, B., Altimir, N., Gruenhage, L., Ammann, C., Cieslik, S., Paoletti, E., Mikkelsen, T. N., Ro-Poulsen, H., Cellier, P., Cape, J. N., Horváth, L., Loreto, F., Niinemets, , Palmer, P. I., Rinne, J., Misztal, P., Nemitz, E., Nilsson, D., Pryor, S., Gallagher, M. W., Vesala, T., Skiba, U., Brüggemann, N., Zechmeister-Boltenstern, S., Williams, J., O'Dowd, C., Facchini, M. C., de Leeuw, G., Flossman, A., Chaumerliac, N., and Erisman, J. W. Atmospheric composition change: Ecosystems-Atmosphere interactions. *Atmospheric Environment 43*, 33 (2009), 5193–5267.

[29] Fowler, S. W. Critical review of selected heavy metal and chlorinated hydrocarbon concentrations in the marine environment. *Marine Environmental Research 29*, 1 (1990), 1–64.

[30] Galbally, I. E., and Roy, C. R. Destruction of ozone at the earth's surface. *Quarterly Journal of the Royal Meteorological Society 106*, 449 (1980), 599–620.

[31] Gallagher, M. W., Beswick, K. M., and Coe, H. Ozone deposition to coastal waters. *Quarterly Journal of the Royal Meteorological Society 127*, October 1999 (2001), 539–558.

[32] Ganguly, N. D. Stratosphere-troposphere exchange of ozone at Indain Antarctic station, Maitri. *Current Science 99*, 8 (2010), 1074–1079.

[33] Ganzeveld, L., Helmig, D., Fairall, C. W., Hare, J., and Pozzer, A. Atmosphere-ocean ozone exchange: A global modeling study of biogeochemical, atmospheric, and waterside turbulence dependencies. *Global Biogeochemical Cycles 23*, 4 (2009), 1–16.

[34] García-Flor, N., Guitart, C., Bodineau, L., Dachs, J., Bayona, J. M., and Albaigés, J. Comparison of sampling devices for the determination of polychlorinated biphenyls in the sea surface microlayer. *Marine Environmental Research 59*, 3 (2005), 255–275.

[35] Garland, J. A., Elzerman, A. W., and Penkett, S. A. The Mechanism for Dry Deposition of Ozone to Seawater Surfaces. *Journal of Geophysical Research 85* (1980), 7488–7492.

[36] Garland, J. A., and Penkett, S. A. Absorption of peroxy acetyl nitrate and ozone by natural surfaces. *Atmospheric Environment 10*, 12 (1976), 1127–1131.

[37] Garrett, W. D. Collection of Slick-Forming Materials from the Sea Surface. *Limnology and Oceanography 10*, 4 (1965), 602–605.

[38] Gašparović, B., Kozarac, Z., Saliot, A., Ćosović, B., and Möbius, D. Physicochemical Characterization of Natural and ex-Situ

Reconstructed Sea-Surface Microlayers. *Journal of Colloid and Interface Science 208* (1998), 191–202.

[39] Gašparović, B., Plavšić, M., Ćosović, B., and Saliot, A. Organic matter characterization in the sea surface microlayers in the subarctic Norwegian fjords region. *Marine Chemistry 105*, 1-2 (2007), 1–14.

[40] Gong, S. L., Walmsley, J. L., Barrie, L. A., and Hopper, J. F. Mechanisms for Surface Ozone Depletion and Recovery During Polar Sunrise. *Atmospheric Environment 31*, 7 (1997), 969–981.

[41] González-Labrada, E., Schmidt, R., and DeWolf, C. E. Kinetic analysis of the ozone processing of an unsaturated organic monolayer as a model of an aerosol surface. *Physical Chemistry Chemical Physics 9*, 43 (2007), 5814–5821.

[42] Griffith, D. R., McNichol, A. P., Xu, L., McLaughlin, F. A., MacDonald, R. W., Brown, K. A., and Eglinton, T. I. Carbon dynamics in the western Arctic Ocean: Insights from full-depth carbon isotope profiles of DIC, DOC, and POC. *Biogeosciences 9*, 3 (2012), 1217–1224.

[43] Hansell, D. A., and Carlson, C. A., Eds. *Biogeochemistry of Marine Dissolved Organic Matter*. Academic Press, London, 2002.

[44] Hardacre, C., Wild, O., and Emberson, L. An evaluation of ozone dry deposition in global scale chemistry climate models. *Atmospheric Chemistry and Physics 15*, 11 (2015), 6419–6436.

[45] Hardy, J. T., Coley, J. A., Antrim, L. D., and Kiesser, S. L. A Hydrophobic Large-Volume Sampler for Collecting Aquatic Surface Microlayers: Characterization and comparison with the Glass Plate Method. *Canadian Journal of Fisheries and Aquatic Sciences 45*, 5 (5 1988), 822–826.

[46] Harvey, G. W. Microlayer Collection From the Sea Surface: A New Method and Initial Results. *Limnology and Oceanography 11*, 4 (1966), 608–613.

[47] Harvey, G. W., and Burzell, L. A. Simple microlayer method for small samples. *LIMNOLOGY AND OCEANOGRAPHY 17*, 1 (1972), 156–157.

[48] Hearn, J. D., Lovett, A. J., and Smith, G. D. Ozonolysis of oleic acid particles: Evidence for a surface reaction and secondary reactions involving Criegee intermediates. *Physical Chemistry Chemical Physics 7*, 3 (2005), 501–511.

[49] Hearn, J. D., and Smith, G. D. Kinetics and product studies for ozonolysis reactions of organic particles using aerosol CIMS. *Journal of Physical Chemistry A 108*, 45 (2004), 10019–10029.

[50] Helmig, D., Boylan, P., Johnson, B., Oltmans, S., Fairall, C., Staebler, R., Weinheimer, A., Orlando, J., Knapp, D. J., Montzka, D. D., Flocke, F., Frieó, U., Sihler, H., and Shepson, P. B. Ozone dynamics and snow-atmosphere exchanges during ozone depletion events at Barrow, Alaska. *Journal of Geophysical Research Atmospheres 117*, 20 (2012), 1–15.

[51] Hou, X., Aldahan, A., Nielsen, S. P., Possnert, G., Nies, H., and Hedfors, J. Speciation of 129I and 127I in seawater and implications for sources and transport pathways in the North Sea. *Environmental Science and Technology 41*, 17 (2007), 5993–5999.

[52] Hu, J. H., Shi, Q., Davidovits, P., Worsnop, D. R., Zahniser, M. S., and Kolb, C. E. Reactive uptake of Cl2(g) and Br2(g) by aqueous surfaces as a function of Br-and I-ion concentration. The effect of chemical reaction at the interface. *Journal of Physical Chemistry 99*, 21 (1995), 8768–8776.

[53] Hu, L., Jacob, D. J., Liu, X., Zhang, Y., Zhang, L., Kim, P. S., Sulprizio, M. P., and Yantosca, R. M. Global budget of tropo-

spheric ozone: Evaluating recent model advances with satellite (OMI), aircraft (IAGOS), and ozonesonde observations. *Atmospheric Environment 167* (2017), 323–334.

[54] Hung, H.-m., and Tang, C.-w. Effects of Temperature and Physical State on Heterogeneous Oxidation of Oleic Acid. *Journal of Physical Chemistry A 114*, 022 (2010), 13104–13112.

[55] Jaafar, S. A., Latif, M. T., Chian, C. W., Han, W. S., Wahid, N. B. A., Razak, I. S., Khan, M. F., and Tahir, N. M. Surfactants in the sea-surface microlayer and atmospheric aerosol around the southern region of Peninsular Malaysia. *Marine Pollution Bulletin 84*, 1-2 (2014), 35–43.

[56] Johnson, P. N., and Davis, R. A. Diffusivity of Ozone in Water. *Journal of Chemical Engineering Data 41*, 6 (1996), 1485–1487.

[57] Kahan, T. F., Kwamena, N. O. A., and Donaldson, D. J. Heterogeneous ozonation kinetics of polycyclic aromatic hydrocarbons on organic films. *Atmospheric Environment 40*, 19 (2006), 3448–3459.

[58] Katrib, Y., Biskos, G., Buseck, P. R., Davidovits, P., Jayne, J. T., Mochida, M., Wise, M. E., Worsnop, D. R., and Martin, S. T. Ozonolysis of mixed oleic-acid/stearic-acid particles: Reaction kinetics and chemical morphology. *Journal of Physical Chemistry A 109*, 48 (2005), 10910–10919.

[59] Katrib, Y., Martin, S. T., Hung, H.-m., Rudich, Y., Zhang, H., Slowik, J. G., Davidovits, P., Jayne, J. T., and Worsnop, D. R. Products and Mechanisms of Ozone Reactions with Oleic Acid for Aerosol Particles Having Core Shell Morphologies. *Journal of Physical Chemistry A 108*, 32 (2004), 6686–6695.

[60] Kawa, S. R., and Pearson Jr., R. Ozone Budget From the Dynamics and Chemistry of Marine Stratocumulus Experiment. *Journal of Geophysical Research 94*, D7 (1989), 9809–9817.

[61] Kieber, D. J., and Mopper, K. Photochemical formation of glyoxylic and pyruvic acids in seawater. *Marine Chemistry 21*, 2 (7 1987), 135–149.

[62] Kieber, R. J., Zhou, X., and Mopper, K. Formation of carbonyl compounds from UV-induced photodegradation of humic compounds in the sea. *Limnology and Oceanography 35*, 7 (1990), 1503–1515.

[63] Kleber, J., and Friedrichs, G. Quantitative Time-Resolved Vibrational Sum Frequency Generation Spectroscopy as a Tool for Thin Film Kinetic Studies: New Insights into Oleic Acid Monolayer Oxidation. *The Journal of Physical Chemistry A 117* (2013), 7863–7875.

[64] Kosak-Channing, L. F., and Helz, G. R. Solubility of Ozone in Aqueous Solutions of 0-0.6 M Ionic Strength. *Environmental Science & Technology 17*, 3 (1983), 145–149.

[65] Kozarac, Z., Risović, D., Frka, S., and Möbius, D. Reflection of light from the air/water interface covered with sea-surface microlayers. *Marine Chemistry 96*, 1-2 (2005), 99–113.

[66] Krueger, A. J., and Minzner, R. A. Mid-Latitude Ozone Model for the 1976 U. S. Standard Atmosphere. *Journal of Geophysical Research 81*, 24 (1976), 4477–4481.

[67] Kwamena, N. O. A., Earp, M. E., Young, C. J., and Abbatt, J. P. D. Kinetic and product yield study of the heterogeneous gas-surface reaction of anthracene and ozone. *Journal of Physical Chemistry A 110*, 10 (2006), 3638–3646.

[68] Lacis, A. A., Wuebbles, D. J., and Logan, J. A. Radiative forcing of climate by changes in the vertical distribution of ozone. *Journal of Geophysical Research 95*, D7 (1990), 9971–9981.

[69] Leisner, C. P., and Ainsworth, E. A. Quantifying the effects of ozone on plant reproductive growth and development. *Global Change Biology 18*, 2 (2012), 606–616.

[70] Lenschow, D. H., Pearson Jr, R., and Stankov, B. B. Measurements of Ozone Vertical Flux to Ocean and Forest. *Journal of Geophysical Research 87*, 2 (1982), 8833–8837.

[71] Levanov, A. V., Antipenko, E. E., and Lunin, V. V. Primary Stage of the Reaction between Ozone and Chloride Ions in Aqueous Solution : Oxidation of Chloride Ions with Ozone through the Mechanism of Oxygen Atom Transfer. *Russian Journal of Physical Chemistry A 86*, 3 (2012), 519–522.

[72] Levich, V. G. *Physicochemical hydrodynamics.*, 2nd ed. Prentice-Hall, Englewood Cliffs N.J., 1962.

[73] Li, Q., Gabay, M., Rubin, Y., Raveh-Rubin, S., Rohatyn, S., Tatarinov, F., Rotenberg, E., Ramati, E., Dicken, U., Preisler, Y., Fredj, E., Yakir, D., and Tas, E. Investigation of ozone deposition to vegetation under warm and dry conditions near the Eastern Mediterranean coast. *Science of the Total Environment 658* (2019), 1316–1333.

[74] Lippmann, M. Health Effects Of Ozone A Critical Review. *Journal of the Air Pollution Control Association 39*, 5 (1989), 672–695.

[75] Lippmann, M. Health Effects of Tropospheric Ozone. *Environmental Science and Technology 25*, 12 (1991), 1954–1962.

[76] Liss, P. S., and Slater, P. G. Flux of Gases across the Air-Sea Interface. *Nature 247* (1974), 181–184.

[77] Liu, Q., Schurter, L. M., Muller, C. E., Aloisio, S., Francisco, J. S., and Margerum, D. W. Kinetics and mechanisms of aqueous ozone reactions with bromide, sulfite, hydrogen sulfite, iodide, and nitrite ions. *Inorganic Chemistry 40*, 17 (2001), 4436–4442.

[78] Macdonald, S. M., Gómez Martín, J. C., Chance, R., Warriner, S., Saiz-Lopez, A., Carpenter, L. J., and Plane, J. M. A laboratory characterisation of inorganic iodine emissions from the sea

surface: Dependence on oceanic variables and parameterisation for global modelling. *Atmospheric Chemistry and Physics 14*, 11 (2014), 5841–5852.

[79] Magi, L., Schweitzer, F., Pallares, C., Cherif, S., Mirabel, P., and George, C. Investigation of the Uptake Rate of Ozone and Methyl Hydroperoxide by Water Surfaces. *The Journal of Physical Chemistry A 101*, 27 (1997), 4943–4949.

[80] Martino, M., Lézé, B., Baker, A. R., and Liss, P. S. Chemical controls on ozone deposition to water. *Geophysical Research Letters 39*, 5 (2012), 39–43.

[81] Martino, M., Mills, G. P., Woeltjen, J., and Liss, P. S. A new source of volatile organoiodine compounds in surface seawater. *Geophysical Research Letters 36*, 1 (2009), 2–6.

[82] Marty, J. C., Saliot, A., Buat-Ménard, P., Chesselet, R., and Hunter, K. A. Relationship between the lipid compositions of marine aerosols, the sea surface microlayer, and subsurface water. *Journal of Geophysical Research 84*, C9 (1979), 5707.

[83] Matyssek, R., and Sandermann, H. Impact of Ozone on Trees: an Ecophysiological Perspective. In *Progress in Botany*, K. Esser, U. Luttge, W. Beyschlag, and F. Hellwig, Eds., 64 ed. Springer Berlin Heidelberg, 2003.

[84] McFadzen, I. R., and Cleary, J. J. Toxicity and chemistry of the sea-surface microlayer in the North Sea using a cryopreserved larval bioassay. *Marine Ecology Progress Series 103*, 1-2 (1994), 103–110.

[85] McKay, W. A., Stephens, B. A., and Dollard, G. J. Laboratory Measurements of Ozone Deposition To Sea-Water and Other Saline Solutions. *Atmospheric Environment Part a-General Topics 26*, 17 (1992), 3105–3110.

[86] McNeill, V. F., Wolfe, G. M., and Thornton, J. A. The oxidation of oleate in submicron aqueous salt aerosols: Evidence of a surface process. *Journal of Physical Chemistry A 111*, 6 (2007), 1073–1083.

[87] McVeigh, P., O'Dowd, C., and Berresheim, H. Eddy Correlation Measurements of Ozone Fluxes over Coastal Waters West of Ireland. *Advances in Meteorology 2010* (2010), 1–7.

[88] Mendez, M., Visez, N., Gosselin, S., Crenn, V., Riffault, V., and Petitprez, D. Reactive and Nonreactive Ozone Uptake during Aging of Oleic Acid Particles. *The Journal of Physical Chemistry A 118* (2014), 9471–9481.

[89] Miller, J. E., Booker, F. L., Pursley, W. A., and Heagle, A. S. Ozone Stress, Carbon Dioxide Enrichment, and Nitrogen Fertility Interactions in Cotton. *Crop Science 39*, 3 (1999), 731–741.

[90] Mmereki, B. T., and Donaldson, D. J. Direct Observation of the Kinetics of an Atmospherically Important Reaction at the Air-Aqueous Interface. *Journal of Physical Chemistry A 107*, 50 (2003), 11038–11042.

[91] Moise, T., and Rudich, Y. Reactive uptake of ozone by proxies for organic aerosols: Surface versus bulk processes. *Journal of Geophysical Research Atmospheres 105*, D11 (2000), 14667–14676.

[92] Moise, T., and Rudich, Y. Reactive uptake of ozone by aerosol-associated unsaturated fatty acids: Kinetics, mechanism, and products. *Journal of Physical Chemistry A 106*, 27 (2002), 6469–6476.

[93] Momzikoff, A., Brinis, A., Dallot, S., Gondry, G., Saliot, A., Lebaron, P., and others. Field study of the chemical characterization of the upper ocean surface using various samplers. *Limnology and Oceanography: Methods 2* (2004), 374–386.

[94] Mopper, K., Zhou, X., Kieber, R. J., Kieber, D. J., Sikorski, R. J., and Jones, R. D. Photochemical degradation of dissolved

organic carbon and its impact on the oceanic carbon cycle. *Nature 353*, 6339 (1991), 60–62.

[95] Moreno, C. G., Gálvez, O., López-Arza Moreno, V., Espildora-García, E. M., and Baeza-Romero, M. T. A revisit of the interaction of gaseous ozone with aqueous iodide. Estimating the contributions of the surface and bulk reactions. *Physical Chemistry Chemical Physics 20*, 43 (2018), 27571–27584.

[96] Morozov, P. A., and Ershov, B. G. The influence of phosphates on the decomposition of ozone in water: Chain process inhibition. *Russian Journal of Physical Chemistry A 84*, 7 (2010), 1136–1140.

[97] Muller, J. B., Dorsey, J. R., Flynn, M., Gallagher, M. W., Percival, C. J., Shallcross, D. E., Archibald, A., Roscoe, H. K., Obbard, R. W., Atkinson, H. M., Lee, J. D., Moller, S. J., and Carpenter, L. J. Energy and ozone fluxes over sea ice. *Atmospheric Environment 47* (2012), 218–225.

[98] Muñoz, F., Mvula, E., Braslavsky, S. E., and von Sonntag, C. Singlet dioxygen formation in ozone reactions in aqueous solution. *Journal of the Chemical Society, Perkin Transactions 2 266*, 7 (2001), 1109–1116.

[99] Myhre, G., Shindell, D., Bréon, F.-M., Collins, W. D., Fuglestvedt, J., Huang, J., Koch, D., Lamarque, J.-F., Lee, D., Mendoza, B., Nakajima, T., Robock, A., Stephens, G., Takemura, T., and Zhang, H. IPCC AR5 (2013) Chapter 8: Anthropogenic and Natural Radiative Forcing. In *Climate Change 2013: The Physical Science Basis. Contribution of Working Group I to the Fifth Assessment Report of the Intergovernmental Panel on Climate Change*, T. Stocker, D. Qin, G. K. Plattner, M. Tignor, S. K. Allen, J. Boschung, A. Nauels, Y. Xia, V. Bex, and P. M. Midgley, Eds. Cambridge University Press, Cambridge, United Kingdom and New York, NY, USA, 2013, pp. 659–740.

[100] Nash, D. G., Tolocka, P., and Baer, T. The uptake of O3 by myristic acid – oleic acid mixed particles : evidence for solid surface layers. *Physical Chemistry Chemical Phsysics 8* (2006), 4468–4475.

[101] Nebbioso, A., and Piccolo, A. Molecular characterization of dissolved organic matter (DOM): A critical review. *Analytical and Bioanalytical Chemistry 405*, 1 (2013), 109–124.

[102] Neil, M. J. *The Merck index : an encyclopedia of chemicals, drugs, and biologicals.* Merck, Whitehouse Station, N.J, 2006.

[103] Olkowska, E., Ruman, M., Kowalska, A., and Polkowska, Determination of Surfactants in Environmental Samples. Part II. Anionic Compounds. *Ecological Chemistry and Engineering S 20*, 2 (2013), 331–342.

[104] Pogorzelski, S. J., and Kogut, A. D. Structural and thermodynamic signatures of marine microlayer surfactant films. *Journal of Sea Research 49*, 4 (2003), 347–356.

[105] Rahlff, J., Stolle, C., Giebel, H. A., Brinkhoff, T., Ribas-Ribas, M., Hodapp, D., and Wurl, O. High wind speeds prevent formation of a distinct bacterioneuston community in the sea-surface microlayer. *FEMS Microbiology Ecology 93*, 5 (2017), 1–14.

[106] Reeser, D. I., Jammoul, A., Clifford, D., Brigante, M., D'Anna, B., George, C., and Donaldson, D. J. Photoenhanced reaction of ozone with chlorophyll at the seawater surface. *Journal of Physical Chemistry C 113*, 6 (2009), 2071–2077.

[107] Rennie, A. R., Pfrang, C., Fisher, F. N., Dong, C. C., Thomas, R. K., King, M. D., Hughes, A. V., and Thompson, K. C. Oxidation of oleic acid at the air–water interface and its potential effects on cloud critical supersaturations. *Physical Chemistry Chemical Physics 11*, 35 (2009), 7699.

[108] Reynolds, G., Corless, C., Graham, N., Perry, R., Gibson, T. M., and Haley, J. Aqueous Ozonation of Fatty Acids. *Ozone: Science & Engineering 11*, 2 (1989), 143–154.

[109] Ribas-Ribas, M., Hamizah Mustaffa, N. I., Rahlff, J., Stolle, C., and Wurl, O. Sea Surface Scanner (S3): A Catamaran for High-Resolution Measurements of Biogeochemical Properties of the Sea Surface Microlayer. *Journal of Atmospheric and Oceanic Technology 34*, 7 (2017), 1433–1448.

[110] Rodrigues, A., Brito, A., Janknecht, P., Proença, M. F., and Nogueira, R. Quantification of humic acids in surface water: effects of divalent cations, pH, and filtration. *Journal of Environmental Monitoring 11*, 2 (2009), 377–382.

[111] Rouviere, A., and Ammann, M. The effect of fatty acid surfactants on the uptake of ozone to aqueous halogenide particles. *Atmospheric Chemistry and Physics 10*, 23 (2010), 11489–11500.

[112] Rouviere, A., Sosedova, Y., and Ammann, M. Uptake of Ozone to Deliquesced KI and Mixed KI / NaCl Aerosol Particles. *Journal of Physical Chemistry A 114* (2010), 7085–7093.

[113] Sakamoto, Y., Yabushita, A., Kawasaki, M., and Enami, S. Direct emission of I2 molecule and IO radical from the heterogeneous reactions of gaseous ozone with aqueous potassium iodide solution. *Journal of Physical Chemistry A 113*, 27 (2009), 7707–7713.

[114] Saliot, A., Marty, J. C., Scribe, P., Sicre, M. A., Viets, T. C., de Leeuw, J. W., Schenck, P. A., and Boon, J. J. Characterization of particulate organic matter in Mediterranean sea-surface films and underlying water by flash pyrolysis and gas chromatographic analyses. *Organic Geochemistry 17*, 3 (1991), 329–340.

[115] Sandström, T., Blomberg, A., Helleday, R., and Rudell, B. Allergy and automobile pollution: experiments in animals. *Revue Française d'Allergologie et d'Immunologie Clinique 40*, 1 (2000), 47–51.

[116] Sarwar, G., Kang, D., Foley, K., Schwede, D., and Gantt, B. Technical note : Examining ozone deposition over seawater. *Atmospheric Environment 141* (2016), 255–262.

[117] Sauer Jr., T. C., Durell, G. S., Brown, J. S., Redford, D., and Boehm, P. D. Concentrations of chlorinated pesticides and PCBs in microlayer and seawater samples collected in open-ocean waters off the U.S. East Coast and in the Gulf of Mexico. *Marine Chemistry 27*, 3-4 (1989), 235–257.

[118] Sauret, C., Tedetti, M., Guigue, C., Dumas, C., Lami, R., Pujo-Pay, M., Conan, P., Goutx, M., and Ghiglione, J. F. Influence of PAHs among other coastal environmental variables on total and PAH-degrading bacterial communities. *Environmental Science and Pollution Research 23*, 5 (2016), 4242–4256.

[119] Schlichting, H., and Gersten, K. *Boundary-Layer Theory*. Springer Berlin Heidelberg, Berlin, Heidelberg, 2017.

[120] Shaw, M. D., and Carpenter, L. J. Modification of ozone deposition and I2 emissions at the air-aqueous interface by dissolved organic carbon of marine origin. *Environmental Science and Technology 47*, 19 (2013), 10947–10954.

[121] Shinki, M., Wendeberg, M., Vagle, S., Cullen, J. T., and Hore, D. K. Characterization of adsorbed microlayer thickness on an oceanic glass plate sampler. *Limnology and Oceanography: Methods 10*, 10 (2012), 728–735.

[122] Sieburth, J. M. Bacterial Substrates and Productivity in Marine Ecosystems. *Annual Review of Ecology and Systematics 7* (1976), 259–285.

[123] Smith, G. D., Woods III, E., Hauser, C., Miller, R. E., and Baer, T. Reactive uptake of ozone by oleic acid aerosol particles: Application of single particle mass spectrometry to the measurement of

heterogeneous reaction kinetics. *Journal of Physical Chemistry A 106* (2002), 8085–8095.

[124] Song, Y. K., Hong, S. H., Jang, M., Kang, J. H., Kwon, O. Y., Han, G. M., and Shim, W. J. Large accumulation of micro-sized synthetic polymer particles in the sea surface microlayer. *Environmental Science and Technology 48*, 16 (2014), 9014–9021.

[125] Stella, P., Loubet, B., de Berranger, C., Charrier, X., Ceschia, E., Gerosa, G., Finco, A., Lamaud, E., Serça, D., George, C., and Ciuraru, R. Soil ozone deposition: Dependence of soil resistance to soil texture. *Atmospheric Environment 199* (2019), 202–209.

[126] Stevenson, D. S., Dentener, F. J., Schultz, M. G., Ellingsen, K., van Noije, T. P., Wild, O., Zeng, G., Amann, M., Atherton, C. S., Bell, N., Bergmann, D. J., Bey, I., Butler, T., Cofala, J., Collins, W. J., Derwent, R. G., Doherty, R. M., Drevet, J., Eskes, H. J., Fiore, A. M., Gauss, M., Hauglustaine, D. A., Horowitz, L. W., Isaksen, I. S., Krol, M. C., Lamarque, J. F., Lawrence, M. G., Montanaro, V., Müller, J. F., Pitari, G., Prather, M. J., Pyle, J. A., Rast, S., Rodriquez, J. M., Sanderson, M. G., Savage, N. H., Shindell, D. T., Strahan, S. E., Sudo, K., and Szopa, S. Multimodel ensemble simulations of present-day and near-future tropospheric ozone. *Journal of Geophysical Research Atmospheres 111*, 8 (2006).

[127] Stevenson, D. S., Young, P. J., Naik, V., Lamarque, J. F., Shindell, D. T., Voulgarakis, A., Skeie, R. B., Dalsoren, S. B., Myhre, G., Berntsen, T. K., Folberth, G. A., Rumbold, S. T., Collins, W. J., MacKenzie, I. A., Doherty, R. M., Zeng, G., Van Noije, T. P., Strunk, A., Bergmann, D., Cameron-Smith, P., Plummer, D. A., Strode, S. A., Horowitz, L., Lee, Y. H., Szopa, S., Sudo, K., Nagashima, T., Josse, B., Cionni, I., Righi, M., Eyring, V., Conley, A., Bowman, K. W., Wild,

O., and Archibald, A. Tropospheric ozone changes, radiative forcing and attribution to emissions in the Atmospheric Chemistry and Climate Model Intercomparison Project (ACCMIP). *Atmospheric Chemistry and Physics 13*, 6 (2013), 3063–3085.

[128] Strunin, M. A., Postnov, A. A., and Mezrin, M. Y. Meteorological potential for contamination of arctic troposphere: Boundary layer structure and turbulent diffusion characteristics. *Atmospheric Research 44*, 1-2 (1997), 37–51.

[129] Tager, I. B. Introduction To Working Group on Tropospheric Ozone, Health-Effects Institute Environmental Epidemiology Planning Project. *Environmental Health Perspectives 101*, 4 (1993), 205–207.

[130] Takahashi, K., Hayashi, S., Matsumi, Y., Taniguchi, N., and Hayashida, S. Quantum yields of O(1D) formation in the photolysis of ozone between 230 and 308 nm. *Journal of Geophysical Research D: Atmospheres 107*, 20 (2002).

[131] Thornberry, T., and Abbatt, J. P. D. Heterogeneous reaction of ozone with liquid unsaturated fatty acids: Detailed kinetics and gas-phase product studies. *Physical Chemistry Chemical Physics 6*, 1 (2004), 84–93.

[132] Thurman, E. M. *Organic geochemistry of natural waters.* Springer Netherlands, 1985.

[133] Tiefenau, H. K. The specific ozone destruction rate of the ocean surface and its dependence on horizontal wind velocity. *Pure and Applied Geophysics 106-108*, 1 (1973), 1116–1123.

[134] Truesdale, V. W. Iodine in inshore and off-shore marine waters. *Marine Chemistry 6*, 1 (1978), 1–13.

[135] Truesdale, V. W., Žic, V., Garnier, C., and Cukrov, N. Circumstantial evidence in support of org-I as a component of the marine

aerosol arising from a study of marine foams. *Estuarine, Coastal and Shelf Science 115* (2012), 388–398.

[136] Van Dam, B., Helmig, D., Doskey, P. V., and Oltmans, S. J. Summertime surface O3 behavior and deposition to tundra in the Alaskan Arctic. *Journal of Geophysical Research 121*, 13 (2016), 8055–8066.

[137] van Pinxteren, M., Müller, C., Iinuma, Y., Stolle, C., and Herrmann, H. Chemical characterization of dissolved organic compounds from coastal sea surface microlayers (Baltic Sea, Germany). *Environmental Science & Technology 46*, 19 (2012), 10455–10462.

[138] von Sonntag, C., and von Gunten, U. *Chemistry of Ozone in Water and Wastewater Treatment*, 1st ed. IWA Publishing, London, 2012.

[139] Voss, L. F., Bazerbashi, M. F., Beekman, C. P., Hadad, C. M., and Allen, H. C. Oxidation of oleic acid at air/liquid interfaces. *Journal of Geophysical Research Atmospheres 112*, 6 (2007), 1–9.

[140] Wang, P., Baines, A., Lavine, M., and Smith, G. Modelling ozone injury to U.S. forests. *Environmental and Ecological Statistics 19*, 4 (2012), 461–472.

[141] Watson, A. J., Bock, E. J., Jähne, B., Asher, W. E., Frew, N. M., Hasse, L., Korenowski, G. M., Merlivat, L., Phillips, L. F., Schluessel, P., Woolf, D. K., and Liss, P. S. Report Group 1 – Physical processes in the microlayer and the air–sea exchange of trace gases. In *The Sea Surface and Global Change*, P. S. Liss and R. A. Duce, Eds. Cambridge University Press, Cambridge, 1997, pp. 1–34.

[142] Wesely, M. L. Parameterization of surface resistances to gaseous dry deposition in regional-scale numerical models. *Atmospheric Environment 23*, 6 (1989), 1293–1304.

[143] Wesely, M. L., Cook, D. R., and Williams, R. M. Field measurement of small ozone fluxes to snow, wet bare soil, and lake water. *Boundary-Layer Meteorology 20*, 4 (1981), 459–471.

[144] Wesely, M. L., and Hicks, B. B. A review of the current status of knowledge on dry deposition. *Atmospheric Environment 34*, 12-14 (2000), 2261–2282.

[145] Whitehead, J. D., Mcfiggans, G., Gallagher, M. W., and Flynn, M. J. Simultaneous coastal measurements of ozone deposition fluxes and iodine-mediated particle emission fluxes with subsequent CCN formation. *Atmospheric Chemistry and Physics 10* (2010), 255–266.

[146] Wong, G. T. F. The Marine Geochemistry of Iodine. *Reviews in Aquatic Sciences 4*, 1 (1991), 45–73.

[147] Wurl, O., and Holmes, M. The gelatinous nature of the sea-surface microlayer. *Marine Chemistry 110*, 1-2 (2008), 89–97.

[148] Wurl, O., Miller, L., Röttgers, R., and Vagle, S. The distribution and fate of surface-active substances in the sea-surface microlayer and water column. *Marine Chemistry 115*, 1-2 (2009), 1–9.

[149] Wurl, O., and Obbard, J. P. A review of pollutants in the sea-surface microlayer (SML): A unique habitat for marine organisms. *Marine Pollution Bulletin 48*, 11-12 (2004), 1016–1030.

[150] Young, P. J., Naik, V., Fiore, A. M., Gaudel, A., Guo, J., Lin, M. Y., Neu, J. L., Parrish, D. D., Rieder, H. E., Schnell, J. L., Tilmes, S., Wild, O., Zhang, L., Ziemke, J., Brandt, J., Delcloo, A., Doherty, R. M., Geels, C., Hegglin, M. I., Hu, L., Im, U., Kumar, R., Luhar, A., Murray, L., Plummer, D., Rodriguez, J., Saiz-Lopez, A., Schultz, M. G., Woodhouse, M. T., and Zeng, G. Tropospheric ozone assessment report: Assessment of global-scale model performance for global and regional ozone distributions, variability, and trends. *Elementa - Science of the Anthropocene 6: 10* (2018).

[151] Zahardis, J., and Petrucci, G. A. The oleic acid-ozone heterogeneous reaction system: products, kinetics, secondary chemistry, and atmospheric implications of a model system – a review. *Atmospheric Chemistry and Physics Discussions 7* (2007), 1237–1274.

[152] Zeng, G., Holladay, S., Langlois, D., Zhang, Y., and Liu, Y. Kinetics of heterogeneous reaction of ozone with linoleic acid and its dependence on temperature, physical state, RH, and ozone concentration. *Journal of Physical Chemistry A 117*, 9 (2013), 1963–1974.

[153] Zhengbin, Z., Liansheng, L., Zhijian, W., Jun, L., and Haibing, D. Physicochemical Studies of the Sea Surface Microlayer. *Journal of Colloid and Interface Science 204* (1998), 294–299.

[154] Zhou, S., Forbes, M. W., and Abbatt, J. P. D. Application of direct analysis in real time-mass spectrometry (DART-MS) to the study of gas-surface heterogeneous reactions: Focus on ozone and PAHs. *Analytical Chemistry 87*, 9 (2015), 4733–4740.

[155] Zhou, S., Gonzalez, L., Leithead, A., Finewax, Z., Thalman, R., Vlasenko, A., Vagle, S., Miller, L. A., Li, S. M., Bureekul, S., Furutani, H., Uematsu, M., Volkamer, R., and Abbatt, J. Formation of gas-phase carbonyls from heterogeneous oxidation of polyunsaturated fatty acids at the air-water interface and of the sea surface microlayer. *Atmospheric Chemistry and Physics 14*, 3 (2014), 1371–1384.